

Abstract of thesis entitled

“Large-area Nanostructures Manipulation: Pattern Generation, Size Modulation and Pattern Transfer”

Submitted by

GAN Zhuofei (甘斫非)

for the Degree of Doctor of Philosophy

at the University of Hong Kong

in August 2022

Recently, nanostructures have become vitally crucial in a wide variety of emerging applications. The high-throughput structure generation, precise feature size control, and high-fidelity pattern transfer remain challenging because of various process limitations. Based on interference lithography, several strategies are theoretically and experimentally studied in this dissertation to achieve large-area, high-performance, and versatile nanopatterning.

To achieve the nanopatterning of high-aspect-ratio structures, the interference pattern contrast is numerically and experimentally investigated on a home-built phase-locked interference lithography system. Enlarging the exposure latitude for the linewidth control, the sufficient interference pattern contrast is very crucial to achieving the desired feature sizes in the photoresist. Using high-contrast interference fringes for exposure, sub-50-nm, high-aspect-ratio, and wafer-scale nanopatterning can be fabricated in photoresist

and the high-aspect-ratio attribute makes the resist pattern well suited for pattern transfer techniques used in nanoimprint mold fabrication.

To achieve high-quality IL nanopatterning on diverse substrates, a process optimization strategy is devised to reduce the standing wave based on numerical modeling. Since the multi-layer substrates usually introduce the optical mismatch in the photoresist resulting in the standing wave phenomenon, which significantly affects the nanopattern quality. Using the tri-layer resist process for high-fidelity pattern transfer as an example, the condition of standing wave generation can be quantitatively characterized by calculating the interface reflectance and the electric field distribution of the photoresist. The standing wave reduction can be achieved by well-designing the multi-layer thicknesses before exposure. This systematic numerical analysis can also be extended in complex multi-layer substrates for the perfect nanopatterning using IL.

To achieve the nanopatterning on unconventional substrates, a high-fidelity and clean nanotransfer lithography strategy is proposed. The water-soluble material is used as the transfer carrier to fully embed pre-fabricated nanostructures to well maintain the order and triboelectric charges on the carrier surface work as adhesive media to ensure high transfer yield. Based on this, we demonstrate the transfer of nanostructures of high resolution, high aspect ratio, three-dimensional profiles, and various materials. The pattern transfer can be also demonstrated on diverse receivers that can be rigid, soft, planar, or curved, even including a 125- μm -diameter single-mode optical fiber.

To achieve the nanopatterning with spatially varying dimensions, a lithographic portfolio that enables precise local dimension tunability is invented. The modulation resolution can be down to the sub-wavelength scale and the modulation area can be up to the wafer scale. Using this novel, high-throughput nanopatterning strategy, 4-inch wafer-

scale nanogratings with highly uniform linewidths and 3-inch wafer-scale high-resolution structural color painting are demonstrated.

The methods studied in this dissertation can be combined with each other and compatible with most mature nanofabrication techniques, indicating applications in nanoscience and nanotechnology fields such as nanophotonics, meta-optics, biosciences, etc.

(440 words)

Large-area Nanostructures Manipulation: Pattern Generation, Size Modulation and Pattern Transfer

by

GAN Zhuofei (甘斫非)

B.E. Huazhong University of Science and Technology

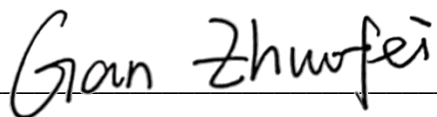
M.Sc. University of Hong Kong

A thesis submitted in partial fulfillment of the requirements for
the Degree of Doctor of Philosophy
at the University of Hong Kong
in August 2022

Declaration

I declare that this thesis represents my own work, except where the due acknowledgment is made, and that it has not been previously included in a thesis, dissertation or report submitted to this University or to any other institution for a degree, diploma or other qualifications.

Signed: _____

A handwritten signature in black ink, appearing to read "Gan Zhuofei".

GAN Zhuofei

Acknowledgements

As a student of the Joint Education Programme for PhD offered by the University of Hong Kong (HKU) and Southern University of Science and Technology (SUSTech), I would like to express my heartfelt gratitude to my supervisors, Prof. Wen-Di Li in HKU and Prof. Dehu Cui in SUSTech, for their supervision as well as to HKU and SUSTech for their support for my research studies in HKU and SUSTech. First, I would like to express my sincere gratitude to Prof. Li, for his kind support and patient guidance throughout my postgraduate career. Beginning with the dissertation project in MSc period, Prof. Li has guided me to the field of nanoscience and carefully support my project. He was always willing to share his insightful thoughts of modern nanotechnology techniques which opened my mind and benefit me for a life-long journey. I also sincerely appreciate my co-supervisor, Prof. Cui in SUSTech, for his technical and financial support for my research.

I also would like to thank all members in the Nanofabrication and Nanodevice Lab. Dr. Liyang Chen introduced me the major equipment and operation trainings that laid the foundation for all my research work. Hongtao Feng collaborated with me on most nanofabrication work and I always enjoy the talk with him. Dr. Siyi Min and Chuwei Liang taught me about operations of lithographic process and shared their rich experimental experiences that helped me a lot. Menghong Xu assisted me for building, maintaining, and troubleshooting with the interference lithography setup. I also learned a lot from Zhao Sun and Chuying Sun, for their professional knowledge in perovskite and 2D materials. Zijie Jiang, Jianwen Zhong and Rulong Ma greatly assisted me by sharing their professional numerical simulation.

My sincere thanks also go to my best friends in HKU, Dr. Wei Li, Dr. Mojun Chen, Cong Chen, Sixi Cao, etc., for companying and enriching my life in Hong Kong. I also

couldn't forget the encouragements from my far-away friends, Kun Jia, Hua He, Xingyu Cheng, etc., which makes me consistently study for PhD.

Last but not the least, I would like to express my deepest gratitude to my parents and wife for their unconditional support.

Table of Contents

Declaration	i
Acknowledgements.....	ii
Table of Contents.....	iv
List of Figures	ix
List of Tables	xxiv
List of Abbreviations	xxv
Chapter 1 Introduction.....	1
1.1 Nanolithography	1
1.2 Interference lithography	3
1.3 Pattern transfer techniques	6
1.4 Opportunities of interference lithography in emerging metasurface.....	7
Chapter 2 Patterning of High-aspect-ratio Nanogratings Using Phase-locked Two-beam Fiber-optic Interference Lithography.....	10
2.1 Introduction	10
2.2 High interference pattern contrast	12
2.2.1 Setup of the phase-locked two-beam fiber-optic interference lithography ..	12
2.2.2 Static interference pattern contrast.....	15
2.2.3 Dynamic interference pattern contrast	17
2.3 Numerical exposure model.....	19

2.4	Experimental demonstrations using high-contrast interference lithography	22
2.4.1	Linewidth control by exposure doses	22
2.4.2	High-aspect-ratio nanostructures	24
2.4.3	Wafer-scale nanopatterning	26
2.4.4	Pattern transfer results.....	28
2.5	Summary	30
Chapter 3 A Numerical Model for Optimizing Interference Lithography on Multi-layer Substrates		32
3.1	Introduction	33
3.1.1	Standing wave phenomenon and anti-reflective coating	33
3.1.2	High-fidelity tri-layer resist process	35
3.2	Numerical modeling of interference lithography on multi-layer substrates.....	37
3.2.1	Reflection above the photoresist interface	37
3.2.2	Contrast of electric field distribution in photoresist	40
3.3	Experimental results	43
3.4	High-fidelity pattern transfer and scalability demonstration.....	45
3.4.1	High-fidelity pattern transfer using tri-layer resist process	45
3.4.2	Scalability of interference lithography on complex substrates	47
3.5	Summary	49

Chapter 4	High-fidelity and Clean Nanotransfer Lithography Using Structure-embedded and Electrostatic-adhesive Carrier.....	50
4.1	Introduction	50
4.2	Fabrication procedure and mechanisms	52
4.2.1	Fabrication process of the structure-embedded and electrostatic-adhesive nanotransfer lithography	52
4.2.2	High-fidelity order-maintaining by polymeric embedding and high transfer yield owing to electrostatically enhanced adhesion.....	54
4.3	Experimental results	58
4.3.1	Structural and material versatility in SENTL process	58
4.3.2	Receiver substrate compatibility in SENTL process	61
4.4	Demonstrations of compact spectrometer with convex nanogratings and SERS analysis on graphene	63
4.5	Summary	65
Chapter 5	Spatial Modulation of Feature Size Using Interference Lithography and Grayscale-patterned Secondary Exposure	67
5.1	Introduction	67
5.2	The dimension modulation using secondary exposure.....	69
5.2.1	Mechanism of the dimension modulation using secondary exposure	69
5.2.2	Photoresist characteristics.....	70
5.2.3	Interference lithography exposure dose distribution.....	72

5.3	Experimental demonstration using secondary exposure	74
5.3.1	UV projection lithography	77
5.3.2	Direct laser writing	79
5.3.3	UV contact photolithography.....	81
5.4	Large-area uniform grating patterning	83
5.5	Summary	87
Chapter 6 High-Resolution and Large-area Grayscale and Structural Color Painting.....		89
6.1	Introduction	89
6.2	Grayscale paintings	90
6.2.1	High-resolution grayscale painting	92
6.2.2	Large-area grayscale painting	93
6.3	Structural color paintings	97
6.3.1	Structural color based on Fabry-Pérot cavity resonances	99
6.3.2	All-dielectric structural color paintings	101
6.4	Experimental details	103
6.5	Summary	104
Chapter 7 Conclusions and Outlooks		106
7.1	Concluding marks.....	106
7.2	Future directions.....	110
Appendix A		113

Appendix B	115
Appendix C	119
Appendix D	125
Appendix E	132
References.....	136
List of Publications	153
Journal publications	153
Conference paper	154

List of Figures

Figure 1-1 Schematic of two-beam interference lithography configuration.....	3
Figure 1-2 Schematics of typical IL configurations, (a) Lloyd's mirror type ²⁷ , (b) Two-beam IL in free space using beam splitter and mirrors ²⁸ . (c) Photograph of the home-built two-beam fiber-optic IL system ²⁹	5
Figure 1-3 Novel optical applications using functional nanostructures. (a) Metolenses at visible wavelengths using TiO ₂ nanorods ⁴⁵ . (b) High-resolution structural color painting using TiO ₂ nanorods ⁴⁸ . (c) Plasmonically active microscope slides using metallic nanoholes ³⁴ . (d) Surface-relief waveguide for AR display using slanting nanogratings ⁵²	9
Figure 2-1 Schematic of the two-beam fiber-optic interference lithography system.	13
Figure 2-2 Schematic of the interference angle change of spherical beams on large-area planar substrate. The interference angle varies away from the center, which acts to the grating period variation.....	14
Figure 2-3 Simulated interference period as a function of position on the 4-inch substrate for non-ideal conditions. Period variation in terms of (a) two-beam angle asymmetry and (b) different arm lengths.....	15
Figure 2-4 The static contrast analysis of two Gaussian beams on large-area substrates. (a) Schematic of Gaussian beam on large-area substrate. (b) Simulated static contrast as a function of position on the 4-inch substrate for different periods.....	17

Figure 2-5 The dynamic contrast enhanced by the phase-locking system. The varying phase differences for (a) the open-loop operation without the phase-locking and (b) the closed-loop operation with the phase-locking.19

Figure 2-6 Simulation on the effect of the exposure time on the latent image and the developed photoresist grating profile. (a) Simulated ideal and (b) real photoresist profiles of the latent image with different exposure time of 30 s, 60 s, 250 s, 1000 s, and 2000 s, respectively.21

Figure 2-7 Simulation on the effect of the interference pattern contrast on the latent image and the developed photoresist grating profile. Simulated photoresist latent images of different contrasts of (a) 0.95, (b) 0.9, and (c) 0.8 with five groups of exposure time of 30 s, 60 s, 250 s, 1000 s, and 2000 s, respectively.....22

Figure 2-8 Experimental results showing the exposure dose modulating the linewidth. (a) SEM images of 1000-nm-period gratings with different exposure doses of 28.5, 34.2, 37.6, 41.2, 47.0, 52.9, 58.8 mJ/cm², respectively. (b) A linear fitting curve of calculated $\cos(\pi d)$ from SEM images in (a) versus Dose⁻¹ recorded in experiments.24

Figure 2-9 Nanogratings with rectangular profiles fabricated by phase-locked 2-FOIL. SEM images of (a) 360-nm-period, (b) 700-nm-period, and (c) 1-μm-period gratings. Scale bars, (a) 200 nm, (b, c) 500 nm.25

Figure 2-10 Nanogratings with high aspect ratio fabricated by phase-locked 2-FOIL. SEM images of (a) 240-nm-period, (b) 850-nm-period, and (c) 850-nm-period gratings. Scale bars, (a) 200 nm, (b, c) 500 nm.25

Figure 2-11 Intensity distribution of Gaussian beams when exposing 400-nm period nanogratings. (a) Plot of normalized calculated Gaussian beam intensity

distribution on 4-inch wafer. (b) Plot of measured intensity distribution on 4-inch wafer using interpolation fitting.....26

Figure 2-12 Large-area nanopatterning using high-contrast 2-FOIL on 3-inch wafer. (a) Photograph of 3-inch wafer carrying 400-nm-period gratings. (b) The period distribution showing 0.3% variation. (c) The linewidth distribution showing 15% uniformity along 80% of the diameter on 3-inch wafer.....28

Figure 2-13 SEM images of diverse pattern transfer results. Etched results using photoresist as mask with different recipes, (a) 360-nm-period rectangular gratings. (b) 850-nm-period high-aspect-ratio gratings. Etched results using a pattern-reversed Cr mask, including (c) Sub-30-nm grooves, (d) 400-nm-period slanted gratings, (e) 700-nm-period nanogratings. (f) Nanomesh structures fabricated by the silicon mold in (e) with multiple NIL processes. Scale bars, 100 nm (a, c, d), and 500 nm (b, e, f).....30

Figure 3-1 The standing wave phenomenon reduced by ARC. (a) SEM images of 400-nm-period gratings without ARC showing distorted lines and rough sidewalls. (b) SEM images of 400-nm-period gratings with ARC showing smooth lines and straight sidewalls. Scale bars, 500 nm.34

Figure 3-2 The lateral linewidth loss induced by ARC open process. (a) Schematic of lateral linewidth loss of resist structures after ARC open process using RIE. SEM images of nanogratings (b) before and (c) after ARC open process, showing a 50-nm linewidth loss. Scale bars, 200 nm.....35

Figure 3-3 Schematic of high-fidelity tri-layer resist process for the fabrication of nanoimprint mold and functional nanodevice. Before spin-coating the photoresist, ARC and interlayer (SiO_2) layers are coated on the substrate. The substrate is

patterned using IL followed by etching of SiO₂ and ARC to form undercut profiles.
For the nanoimprint mold fabrication, the substrates could be performed by the Cr evaporation, lift-off, and etching processes. For the nanodevice fabrication, functional material could be evaporated followed by lift-off36

Figure 3-4 Results of measured refractive indices n and extinction coefficients k versus wavelength for ARC (AZ BarLi II 200) and photoresist (AZ MiR 701) via spectroscopic ellipsometry measurements.....37

Figure 3-5 Numerical modeling results for the reflectivity at the boundary between the photoresist and underlying interlayer. Simulated reflectivity vs ARC thickness with (a) different interlayer materials, (b) different SiO₂ thicknesses, and (c) different periods.....39

Figure 3-6 Contrast distributions versus thicknesses of SiO₂ and ARC for exposing nanostructures of different periods, (a) 400 nm and (b) 240 nm.41

Figure 3-7 FDTD simulation of the electric field distribution in the ARC/SiO₂/photoresist stack. The best result is in the 210-nm ARC group, followed by the 80-nm ARC group, while 80-nm ARC group is the worst. The interference period and photoresist thickness are fixed at 400 nm and 300 nm, while SiO₂ and ARC thicknesses are assigned as 15/25/35/45 nm and 80/140/210 nm, respectively.42

Figure 3-8 SEM images of IL-exposed 400-nm-period gratings using different ARC and SiO₂ thicknesses. Gratings with 80 and 210 nm ARC have vertical and smooth profiles due to the high contrast, while gratings with 140 nm ARC are strongly affected by the standing wave, showing rough profiles.....44

Figure 3-9 SEM images recorded for each step in TLR process. (a) High-quality photoresist nanopillar pattern exposed by IL. (b) SiO₂ interlayer etched using photoresist as the etching mask. (c) ARC layer etched using the SiO₂ as the etching mask, which forms an undercut structure. (d) Cr deposited by e-beam evaporation. (e) Cr pattern left after the lift-off process. (f) High-quality Si nanohole pattern etched using Cr as the etching mask. Scale bars, 200 nm.....46

Figure 3-10 The fidelity characterization by SEM measurements. SEM images of (a) photoresist nanopillars and (b) Si nanoholes before and after TLR pattern transfer, respectively. (c) The statistical plot with the circle diameter characterization of nanopatterns in photoresist and Si, showing the size reduction of less than 4%. Scale bars, 200 nm.....47

Figure 3-11 Simulated and experimental results of TMM and FDTD analysis applied on complex multi-layer substrates. (a) Simulated and (b) SEM results of IL-exposed nanogratings on 240-nm-thick ARC, which has a high contrast and undesired profiles. (c) Simulated and (d) SEM results of IL-exposed nanogratings on 175-nm-thick ARC, which has a low contrast and high-quality profiles. Scale bars, 200 nm.....48

Figure 4-1 Process flow of SENTL applied on electroplated metallic nanostructures...53

Figure 4-2 SEM images recorded for key steps in SENTL process. (a) Imprinted nanoholes in resist on ITO. (b) Electrodeposited Cu nanodisks on ITO. (c) Cu nanodisks-embedded PVA film. (d) Transferred Cu nanodisks on a glass substrate. Scale bars, 300 nm (a-d), 1 cm (insets in c, d).....54

Figure 4-3 Schematic illustration of the high-fidelity lateral dimension maintaining and high transfer yield due to triboelectric electrostatic adhesion.55

Figure 4-4 High fidelity characterization of SENTL. (a) and (b), SEM images of Cu nanogratings before and after SENTL transfer, respectively. (c) The statistical box plot with the mean, maximum, minimum, and 25-75% range of the distribution of the line spacing and line edge roughness of Cu nanogratings before and after transfer. Scale bars, 300 nm.....56

Figure 4-5 Triboelectric charges characterization in SENTL. (a) and (b), the KPFM surface topography and surface potential mapping of the PVA carrier film with embedded Au nanogratings immediately after separation and after charge releasing, respectively. (c) The KPFM surface potential difference variation before and after charge releasing. Scale bars, 300 nm.....57

Figure 4-6 High transfer yield of SENTL. (a) Photograph of the 1-cm²-area transferred nanodisk pattern. (b-f) SEM images obtained from five different points on the transferred pattern. Scale bars, 2 μm in (b-f) and 1 cm in (a).....58

Figure 4-7 SEM images of various 1D/2D nanostructures transferred by SENTL. (a) High-resolution Au nanogratings with 40-nm spacing. (b) 700-nm-period Cu nanodisks of uniform diameters with a standard deviation of 2.8 nm. (c) 550-nm-period Au nanohole array. Scale bars, 300 nm (a, inset in c), 500 nm (b), and 1000 nm (c).....59

Figure 4-8 SEM images of high-aspect-ratio and 3D nanostructures transferred by SENTL. (a) High-aspect-ratio Cu nanogratings with 300-nm width and 600-nm height. (b) Quasi-3D Z-shaped Ni nanostructures. (c) Stacked-mesh nanostructure fabricated by double SENTL transfer. Scale bars, 300 nm (inset in c), 500 nm (a, b), and 1000 nm (c, inset in a).60

Figure 4-9 SEM images of various nanostructures transferred by SENTL. (a, b) 700-nm-period Pd and Co nanodisks. (c) 700-nm-period Au nanodisks and (d) corresponding EDX spectrum indicating a residue-free transfer. Scale bars, 500 nm.61

Figure 4-10 Experimental results of SENTL-transferred nanostructures on flexible and patterned substrates. Including (a) PDMS pad, (b) PI film, (c) PTFE film, (d) 10- μm diameter and 2- μm height Si micropost array. Scale bars, 500 nm (a-c), 10 μm (d), and 1 cm (insets in a-c).62

Figure 4-11 SEM images and photographs of SENTL-transferred nanostructures on curved substrates. Including (a) glass ball, (b) plastic optical fiber, (c) inner and outer wall of a glass vial, and (d) 125- μm diameter single-mode optical fiber. Scale bars, 1 cm.63

Figure 4-12 Compact spectrometer enabled by SENTL. (a) Photograph of rainbow-like stripe image formed by dispersing and focusing the light from a white LED using the transferred nanogratings on a convex lens. (b) Greyscale image of the stripe captured by a monochromatic CMOS detector. (c) Plot that maps the pixel position to the calibrated wavelength. (d) Reconstructed spectrum obtained from the greyscale image. (e) Reference spectrum measured by a commercial spectrometer. Scale bar, 1 cm.64

Figure 4-13 SERS analysis on graphene enabled by SENTL. (a) Schematic diagram and (b) SEM image of transferred Au nanodisks on monolayer graphene. (c) Raman spectra showing an enhancement of Raman signatures of Au-covered graphene over that measured from bare graphene under 785-nm excitation. Scale bar, 300 nm.65

Figure 5-1 The schematic diagram of the IL-GPSE process. Step 1, a two-beam IL is performed on the photoresist to form periodic latent exposed regions with sinusoidal dose profile. Step 2, a secondary exposure follows the IL exposure and increases the effective dose applied on the photoresist which increases the portion of photoresist that receives above-threshold dose, and then leaves less photoresist after development.....70

Figure 5-2 The influence of photoresist contrast on IL-GPSE process. (a) Normalized measured photoresist remaining thickness as a function of exposure dose (blue squares) and the corresponding best fitting curve (red line). (b-d) Simulated photoresist profiles using IL-GPSE model by assigning different photoresist (PR) contrasts.72

Figure 5-3 The influence of IL dose distribution on IL-GPSE process. Simulated photoresist profiles using IL-GPSE model by assigning different contrasts of the interference exposure dose distribution: (a) 0.95, (b) 0.8, (c) 0.7 and (d) 0.6.74

Figure 5-4 Experimental results of IL-GPSE with different combinations of IL and secondary exposure doses. (a) SEM image matrix of 1000-nm-period gratings with various linewidths fabricated by different IL and secondary exposure doses. (b) The FWHM linewidths measured in (a), showing the linewidth is negatively correlated to both IL and secondary exposure doses.76

Figure 5-5 The simulated duty cycle variation as a function of the secondary exposure dose using various initial IL exposure doses.77

Figure 5-6 Experimental results of IL-GPSE using UV projection lithography. (a) A 3-inch wafer carrying the HKU logo consisting of 600-nm-period photoresist gratings with the linewidths in different regions modulated by projected grayscale

pattern. (b) SEM images taken on background, “H”, “K”, and “U” letters on the wafer, showing corresponding linewidths of 250, 190, 140, and 110 nm. Scale bars, 500 nm.....78

Figure 5-7 Experimental results of IL-GPSE using direct laser writing. (a) SEM images of the spatial resolution test for secondary exposure using direct laser writing with different critical dimensions of (i) 4.2, (ii) 2.6, (iii) 1.7 and (iv) 1.4 μm . (b) Plot of the filling ratio of nanostructures in the green box in (iii) versus the horizontal position, showing a resolution of 1.7 μm . Scale bars, 2 μm80

Figure 5-8 Single-pixel modulation using IL-GPSE. (a) SEM image of a 600-nm-period hole array modulated by single-pixel secondary exposure. (b) Plot of the filling ratio of nanostructures in the red box in (a) versus the horizontal position, showing a resolution of 1 μm81

Figure 5-9 Experimental results of IL-GPSE using UV contact Photolithography. (a) The OM image of a 12-point-star pattern, consisting of 600-nm-period gratings with linewidths modulated by contact photolithography using a photomask. SEM images taken inside and outside the secondary exposure pattern, showing the 245-nm and 170-nm linewidths, respectively. (b) Green-box and (c) yellow-box regions in (a), characterized by (i) SEM images and (ii) linewidth distributions. (d) The linewidth variation measured every 200 nm along a grating line (white), showing the grating linewidth gradient of 35 nm/ μm . Scale bars, 500 nm (a), 1 μm (b, c).82

Figure 5-10 Schematic of uniform nanopatterning using secondary exposure to compensate the linewidth variation due to the non-uniform Gaussian beam for IL.84

Figure 5-11 4-inch wafer-scale uniform nanogratings fabricated by IL-GPSE. (a) Photograph of IL-exposed 400-nm-period gratings over a 4-inch wafer with the diffracted blue light intensity gradually decreasing from the center to the edge. (b) SEM images taken in the labelled positions in (a), showing a poor control of linewidth and roughness. (c) Photograph of 400-nm-period gratings over a 4-inch wafer using secondary exposure with a designed projected grayscale pattern after IL exposure, diffracting uniform blue light. (d) SEM images recorded in the labelled positions in (c), showing the uniform linewidth and linewidth roughness. (e) The 4-inch (i) intensity distribution for linewidth tailoring and (ii) devised grayscale image transformed by the characterized relation between the digital grayscale value and projected light intensity via the UV projector. Scale bars, 500 nm.....85

Figure 5-12 Morphological comparison of 4-inch nanogratings fabricated by IL and IL-GPSE. The comparison of (a) linewidth and (b) linewidth roughness distributions over the radius of 4-inch wafers with and without the secondary exposure.....87

Figure 6-1 (a) Schematic of spatial modulation of filling ratio for 2D nanostructures using IL-GPSE. (b) SEM image matrix of 400-nm-period 2D pattern with various filling ratios fabricated by different IL and secondary exposure doses.....91

Figure 6-2 Ultrahigh-resolution grayscale paintings constructed of nanostructures patterned by IL-GPSE. SEM images show the paintings of (a) *Girl with a Pearl Earring*, (b) *The Starry Night*, and (c) a cute American shorthair cat. (d) The original grayscale images for secondary exposures, where the grayscale implies doses. Scale bars, 10 μ m.....93

Figure 6-3 The grayscale tuning on wafer scale. (a) The photograph of 25 squares of 700-nm-period 2D patterns on photoresist modulated by secondary exposure projection, showing a clear grayscale change from dark brown to light gold. (b) SEM images of the region labelled using white box in (a). (c) Fraction area of photoresist calculated from SEM images of Figure E-2, showing a negative correlation between the photoresist filling ratio and the secondary exposure dose. Scale bars, 2 μm (inset in b), 10 μm (b), and 1 cm (a)95

Figure 6-4 Large-area grayscale painting on 3-inch wafer. (a) A photograph of the 3-inch grayscale painting of *Along the River During the Qingming Festival* in photoresist patterned by IL-GPSE. (b) A dynamic structural color due to the residual diffraction at tilting angles. Grayscale paintings patterned by IL-GPSE are further (c) etched into 300-nm-thick SiO₂-coated Si wafer, and (d) deposited with 50-nm-thick Ag on glass. Scale bars, 1 cm (b-d).....96

Figure 6-5 Different colors produced by different nanostructures. (a) (i) OM, (ii) SEM and (iii) zoom-in SEM images showing a butterfly pattern composed of 1- μm -period nanostructures with orthogonal lattices. (b) (i) OM, (ii) SEM and (iii) zoom-in SEM images showing a butterfly pattern composed of 360-nm-period nanostructures with hexagonal lattices. Scale bars, 10 μm98

Figure 6-6 Structural color demonstration based on Fabry-Pérot cavity resonance. (a) Schematic of the Fabry-Pérot cavity structure using photoresist, etched ARC and Si substrate. (b) The fabricated centimeter-scale metasurface displaying various structural colors. (c) SEM images of different regions in (a), showing nanostructures with different feature sizes modulated by IL-GPSE.....100

Figure 6-7 All-dielectric structural color painting based on Mie resonances. (a) Schematic illustration of the metasurface unit cell composed of Si nanopillar on a fused silica substrate. The height of the pillars is 220 nm, the period is 400 nm, and the diameter is a varying parameter. (b) FDTD simulated reflective spectra of the Si metasurface with different diameters ranging between 80 nm (light green) and 180 nm (pink). The insets are the corresponding structural color. (c) Spatial distributions of the simulated electromagnetic field for Si nanopillars with diameters of (i) 100 nm and (ii) 160 nm. (d) The photograph of the all-dielectric Si metasurface, showing a map of China with the provinces distinguished by structural colors.....	102
Figure 7-1 Conclusions of this dissertation: The fabrication and applications of nanostructures through interference lithography and pattern transfer techniques.	109
Figure 7-2 (a) Initial prototype of home-built automated 2-FOIL system. (b) Fabricated nanopattern with different periods for the AR diffractive waveguide.....	110
Figure 7-3 (a) Schematic of re-usable template-based nanotransfer lithography. (b) SEM image of the transfer template using SiO ₂ nanostructures as masks. (c) SEM images of the transferred Cu nanopillars after (i) 1 st and (ii) 2 nd transfers.....	111
Figure A-1 The schematic illustration of different pattern transfer techniques.....	113
Figure A-2 SEM images recorded every 5 mm along the diameter of the 3-inch wafer patterned by 2-FOIL.	114
Figure B-1 The illustration of tri-layer structure for TMM analysis	115
Figure B-2 Collapse of the undercut structure when exposing sub-100-nm pattern using thick ARC. (a) schematic of the collapse happened when etching ARC to	

form the undercut structure. SEM images of final etched pattern (b) nanogratings and (c) nanopillars in Si when the collapse happened. Scale bars, 200 nm.....117

Figure B-3 Fabrication of high-aspect-ratio MIM nanostructures. (a) Schematic of the fabrication of Au-SiO₂-Au nanostructures using RIE and IBE subtractive manufacture. (b) The SEM image of high-aspect-ratio Au-SiO₂-Au nanogratings fabricated by IL, RIE and IBE.....118

Figure C-1 SEM image of the PVA film with nanostructures embedded. Scale bar, 10 μm.....119

Figure C-2 SEM images of the etched high-aspect-ratio Si nanostructures using transferred Cu pattern as the mask, (a) 800-nm-height nanogratings, (b) 1500-nm-height nanopillars. Scale bars, 500 nm.....120

Figure C-3 The schematic process flow of fabricating Z-shaped nanostructures. (a) Shadow evaporation on the resist grating. (b) Dissolving the resist. (c) Spin-casting PVA solution to fill the space among nanostructures.....121

Figure C-4 SEM images of the etched Si square nanohole array using transferred stack-mesh as the mask. Scale bars, 5 μm and 500 nm (inset).122

Figure C-5 SEM images and corresponding EDX spectra and mapping of the transferred (a, b) Cu and (c, d) Pd nanodisks on Si. Scale bars, 500 nm.....123

Figure C-6 Spectra for wavelength calibration of (a) 470 nm, (b) 532 nm and (c) 650 nm.124

Figure D-1 Negative-tone photoresist test using IL-GPSE. (a) SEM images of 1000-nm-period gratings in negative-tone photoresist patterned by IL-GPSE process. (b)

The measured linewidths showing a positive correlation to secondary exposure dose.....	125
--	-----

Figure D-2 IL-GPSE method using UV projection lithography. (a) Setup of the UV projection for secondary exposure with a digital grayscale image. (b) Digital grayscale image for the UV projection to generate a patterned UV intensity distribution. (c) The intensity distribution converted from (b) for secondary exposure.....126

Figure D-3 SEM images recorded every 2.5 mm along the radius of the 4-inch wafer patterned only by interference lithography.....127

Figure D-4 SEM image matrix of 400-nm-period gratings exposed by different combinations of interference lithography and secondary exposure doses.....128

Figure D-5 The linewidths measured in the SEM images of Figure D-4.129

Figure D-6 The relationship between digital grayscale value and normalized projected light intensity using the UV projector.....130

Figure D-7 SEM images recorded every 2.5 mm along the radius of the 4-inch wafer patterned by IL and grayscale-patterned secondary exposure.131

Figure E-1 (a) The photograph of 25 squares of 700-nm-period 2D patterns on photoresist modulated by secondary exposure projection, showing a clear grayscale change from dark brown to light gold. (b-f) Measured reflection spectra on each square.....132

Figure E-2 SEM images of all 25 areas in Figure 6-3a patterned by different secondary exposure doses.133

Figure E-3 Pixel-by-pixel mapping of an image into grayscale and intensity channels.134

Figure E-4 Results of measured refractive index n and extinction coefficient k versus wavelength for polysilicon deposited by LPCVD. 135

List of Tables

Table 3-a Refractive indices for Interlayer material	38
---	----

List of Abbreviations

2D	Two-Dimensional
2-FOIL	Two-beam Fiber-optic Interference Lithography
3D	Three-Dimensional
AFM	Atomic Force Microscopy
AR	Augmented Reality
ARC	Anti-reflective Coating
CMOS	Complementary Metal-oxide-semiconductor
DLW	Direct Laser Writing
DMD	Digital Micromirror Device
DUV	Deep Ultra-violet
EBE	Electron Beam Evaporation
EBL	Electron Beam Lithography
EDX	Energy-dispersive X-ray
EUV	Extreme Ultra-violet
FDTD	Finite-difference Time-domain
FIB	Focused Ion Beam
FWHM	Full Width at Half-maximum
IBE	Ion Beam Etching
IC	Integrated Circuits
ICP	Inductively Coupled Plasma
IL	Interference Lithography
IL-GPSE	Interference Lithography and Grayscale-patterned Secondary Exposure

ITO	Indium-Tin Oxide
KPFM	Kelvin Probe Force Microscopy
MIM	Metal-Insulator-Metal
NIL	Nanoimprint Lithography
NTL	Nanotransfer Lithography
OM	Optical Microscopy
PAC	Photoacid Compound
PDMS	Polydimethylsiloxane
PGMEA	Propylene Glycol Methyl Ether Acetate
PI	Polyimide
PTFE	Polytetrafluoroethylene
PVA	Polyvinyl Acetate
RIE	Reactive Ion Etching
SE	Secondary Exposure
SEM	Scanning Electron Microscopy
SENTL	Structure-embedded and Electrostatic-adhesive Nanotransfer Lithography
SERS	Surface-enhanced Raman Spectroscopy
SM	Single Mode
TLR	Tri-layer Resist
TMM	Transfer Matrix Method
UV	Ultra-violet

Chapter 1 Introduction

“There’s plenty of room at the bottom.”

- Richard Feynman

As Richard Feynman predicted at an American Physical Society meeting in 1959¹, nanotechnology has been widely investigated and achieved enormous breakthroughs in the past decades. Generally, nanotechnologies are defined as the design, production and application of structures, devices, and systems by manipulating the shape and size at nanometer scale. Due to the novel physical, chemical, mechanical, and other characteristics exhibited in nanoscale, artificial nanostructures have attracted great interests in a variety of emerging applications such as integrated circuits (IC), meta-optics, biosciences etc. The progress of nanotechnology in fundamental scientific research and industrial production points towards developing advanced nanofabrication techniques, which transforms the theoretical design into actual physical structures of specific functional material.

1.1 Nanolithography

Used for directly regulating the geometries and dimensions of the pattern, lithography is of central importance in fabricating modern nanodevices because the functionality closely associates with the nanostructure dimensions. For example, the state-of-art IC chip performance has significantly benefited from the development of the advanced extreme ultra-violet (EUV) photolithography technologies for achieving the 5-nm process to integrating more transistors within smaller areas. Generally, the workhorses of modern nanolithographic techniques are electron beam lithography (EBL)²⁻⁴, focused ion beam (FIB)⁵⁻⁷, and direct laser writing (DLW)^{8,9}, which use electron, ion, and photon beams, respectively, to scan and write the patterns. Both EBL and FIB can write sub-10 nm

nanostructures, however, the serial pixel-by-pixel writing mode is extremely low-throughput and needs a long turnaround time for one iteration. Although DLW writes relatively faster and enables three-dimensional (3D) structures, its minimum feature size is around 0.5 μm due to the diffraction limit.

In comparison, parallel nanopatterning techniques such as photolithography and nanoimprint lithography (NIL) enable the fabrication of large-scale nanostructures in high throughput. Using light to transfer the geometric pattern from the photomask to photoresist on substrates, photolithography has become the most adopted strategy for IC and MEMS fabrication due to the consistent and high-throughput capabilities. However, most nanoscience research usually cannot afford nanoscale optical lithographic approaches that use deep ultra-violet (DUV)¹⁰⁻¹² or EUV¹³⁻¹⁵ sources, since the short-wavelength lasers and dense-nanopattern photomask are extremely expensive. Thus, most optical lithography for scientific research can only fabricate patterns of micrometer scale. The other famous parallel nanolithography NIL¹⁶⁻¹⁸, enabling high-resolution (sub-10 nm), wafer-scale patterning, low-cost process, and the versatilities of roll-to-roll^{19,20} and step-and-repeat^{21,22} modes, has been rapidly employed in both scientific research and industrial mass production. However, NIL is a replication process that highly relies on the master mold, which is still challenging because mold fabrication still refers to the above-mentioned scanning beam lithographic techniques. Besides, both the advanced optical lithography and NIL require superior equipment, professional operation, and high-level clean room, etc. Other parallel nanopatterning techniques like self-assembly lithography^{23,24}, nanosphere lithography^{25,26} etc., can only fabricate periodic nanostructures with specific orders, which has a poor pattern flexibility. Among all the nanopatterning techniques of nanoscience and nanotechnologies, interference lithography attracts great interest and holds a great deal of

promises with the simple optical configuration, quick nanopattern generation, and high process compatibility.

1.2 Interference lithography

Interference lithography (IL), also known as interferometric lithography or holographic lithography, is a maskless nanolithography technique that uses the interference pattern formed by two or more coherent laser beams to fabricate periodic nanostructures. In the basic two-beam IL configuration, a coherent laser beam is split into two sub-beams and the sub-beams overlap on the photoresist-coated substrate with an angle (Figure 1-1). The interference intensity of sinusoidal profiles can be recorded in photoresist and finally developed into physical periodic structures. The periodicity (P) of the interference pattern can be determined by

$$P = \frac{\lambda}{2n \sin \theta} \quad (1.1)$$

where λ is the laser wavelength, θ is half of the angle between the two sub-beams, and n is the environmental refractive index.

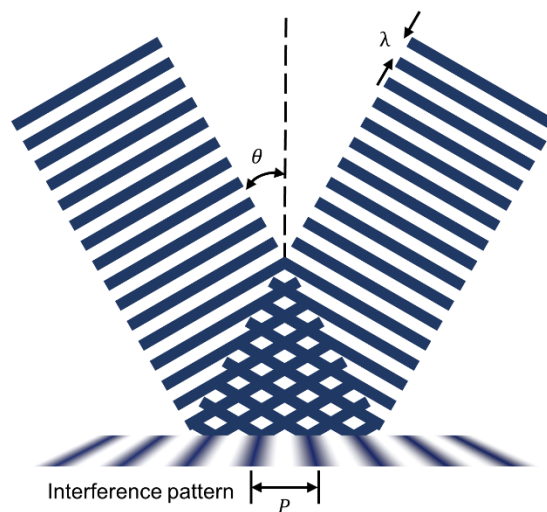


Figure 1-1 Schematic of two-beam interference lithography configuration.

IL systems has been developed in diverse configurations, such as the wavefront-divided Lloyd's mirror type and amplitude-divided multi-beam type. The former, reflecting half of the beam wavefront by a mirror to overlap with the other half to generate interference patterns, has simple optical configurations that benefits flexible periodicity adjustment (Figure 1-2a)²⁷. But the patterning area in this configuration is typically limited to centimeter scale due to the mirror size and the beam intensity profile. The latter is suitable for wafer-scale patterning because the split coherent sub-beams can completely overlap to generate large-area interference fringes (Figure 1-2b). However, the split beams have different optical paths that cause the fluctuating phase difference, in which a phase-locking system is typically needed and makes this configuration complex²⁸. The whole setup usually needs to be re-built and re-aligned when adjusting the period. This dissertation is mainly based on a novel two-beam amplitude-divided IL setup that uses fiber-optics to replace the conventional optical lens, pinholes, and mirrors²⁹ (Figure 1-2c), which enjoys merits of fast period re-configuration, high-quality and wafer-scale nanopatterning (**Chapter 2**).

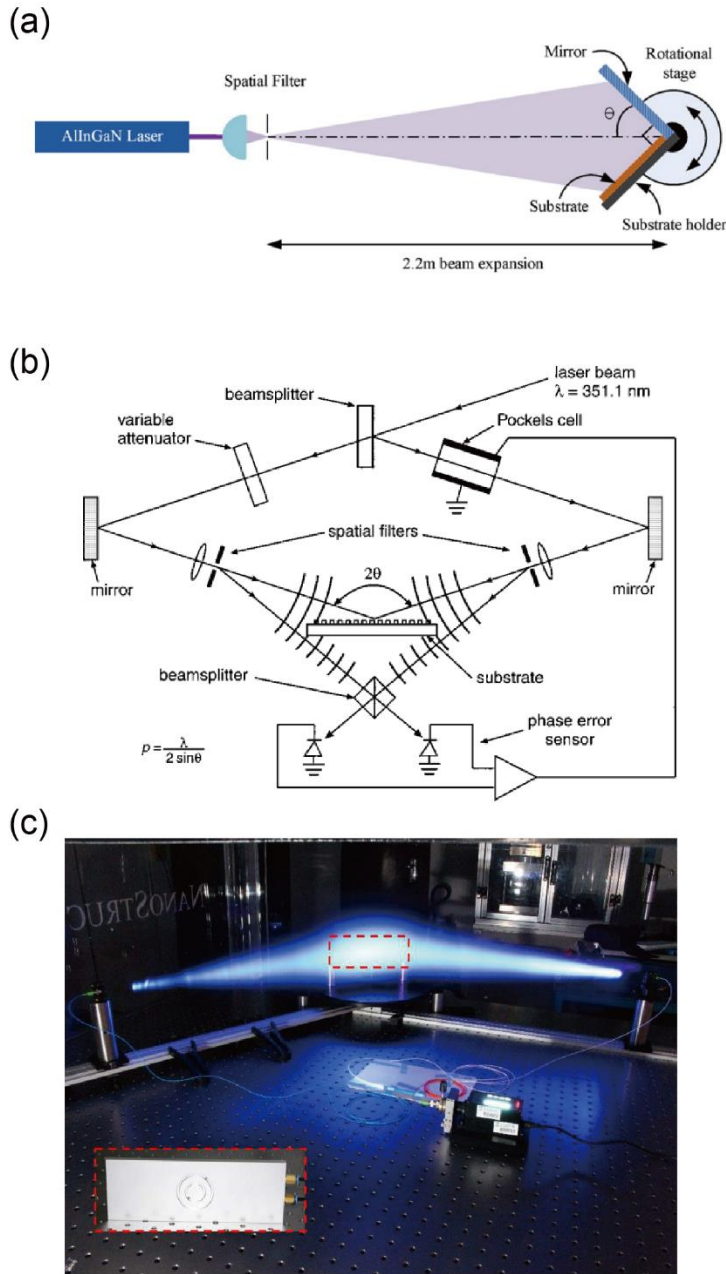


Figure 1-2 Schematics of typical IL configurations, (a) Lloyd's mirror type²⁷, (b) Two-beam IL in free space using beam splitter and mirrors²⁸. (c) Photograph of the home-built two-beam fiber-optic IL system²⁹.

IL is very advantageous for fabricating periodic nanostructures, which has been widely used in various fields such as photonic crystals, diffractive waveguides, and material and crystal growth that require nanotextured surfaces with specific lattices³⁰, etc. In addition to periodic parallel lines, IL also enables the fabrication of various two-

dimensional (2D) nanopatterns by double exposure with an angle. The 2D nanostructures include pillars, checkerboards, holes, rods, etc., which are the potential building blocks for nanophotonic, plasmonic, and meta-optic research and applications. Without scanning or stitching nanopatterns of small areas, IL possess the fast fabrication of large-area dense periodic nanostructures, which is very beneficial for the low-cost fabrication of diverse nanotextured substrates in both scientific research and industrial prototyping.

Although IL can only fabricate periodic nanostructures, its ability to create the perfect sinusoidal exposure field can be viewed as an asset instead of a limitation if viewed from a different perspective. Without any photomasks or templates, the exposed feature size can be easily modulated by increasing or decreasing the amplitude of the sinusoidal exposure field distribution, indicating that the minimum feature size is no longer primarily constrained by the laser source wavelength. In this dissertation, we demonstrate sub-50 nm lines fabricated by a 405 nm laser (**Chapter 2**). Despite only a few nanodevices that can be directly fabricated by IL, the ability of nanoscale patterning is valuable for characterizing the other processes such as etching or deposition that are associated with lithography. Compatible with the mainstream photolithographic process, IL can be easily combined with other nanofabrication techniques to transfer the resist pattern into functional materials for broader areas (**Chapter 3**).

1.3 Pattern transfer techniques

Defining the nanoscale shapes and sizes in photoresists using the nanolithography approaches, a subsequent pattern transfer technique should be necessarily employed to transfer the geometries into functional materials for different nanoscale devices or systems. For example, metallic nanostructures exhibit extraordinary optical responses for color filtering^{31,32} and plasmonic sensing^{33,34}. Dielectric nanostructures are promising in meta-

optics for less optical loss and high refractive indices^{35,36}, featuring a more powerful ability of light manipulation. In pattern transfer processes, pattern fidelity is of great importance because the feature sizes directly affect the device performance. For example, the linewidth variation introduced by undesirable etching recipes when fabricating nanogratings would deteriorate the diffraction efficiency. For meta-optics, the geometric variation in building blocks closely relates to the phase change and intensity that affect the device performance³⁷. In this dissertation, a nanofabrication process portfolio is introduced for high-quality pattern generation and high-fidelity pattern transfer on complex substrates of metallic and dielectric materials (**Chapter 3**).

Besides, a variety of emerging applications requires nanopatterning on unconventional substrates such as flexible materials for electronic skins^{38,39} or curved surfaces like the lens^{40,41} and fiber optics^{42,43}. A novel nanotransfer lithography is also proposed in **Chapter 4** that can achieve clean and high-fidelity transfer of pre-fabricated nanostructures onto diverse substrates, which facilitates the exploration of new nanopatterning applications.

1.4 Opportunities of interference lithography in emerging metasurface

In addition to state-of-art IC technology, another emerging application that has benefitted from advanced nanofabrication techniques is the metasurfaces. Due to the extraordinary manipulation on electromagnetic waves, the metasurfaces constructed of subwavelength-scale artificial structures make it possible to achieve flat, ultrathin optical devices. Providing new degrees of freedom to control the amplitude, phase, and polarization with subwavelength resolution, novel optical applications has been widely investigated including metalenses^{44,45}, meta-holograms^{46,47}, structural colors^{48,49}, AR

displays^{50,51} shown in Figure 1-3. All of these applications require the advanced, precise, and controllable fabrication of nanostructures.

Many practical nanotechnology applications such as metalenses, structural color paintings, and AR waveguides, usually require a large pattern area to obtain better performance. For example, large-area metalenses offer opportunities to replace traditional, bulky optical components used in applications such as high-level microscopy, imaging, and AR display. A large-area light out-coupling gratings in the AR diffraction waveguide has a large eyebox for a better user-friendly experience. However, the current mainstream EBL strategy is quite low-throughput and costs a lot when fabricating the pattern of centimeter scale or wafer scale for prototyping and iterations. While current high-throughput approaches of photolithography and NIL highly rely on expensive equipment and consumables such as photomasks and templates. In this dissertation, a versatile IL strategy enabling the feature size modulation is introduced in **Chapter 5**, which exhibits enormous advantages in fabricating large-area metasurfaces. Using the structural color as the example, large-area and high-resolution metasurface paintings are demonstrated in **Chapter 6**, indicating the ability of fabricating novel optics.

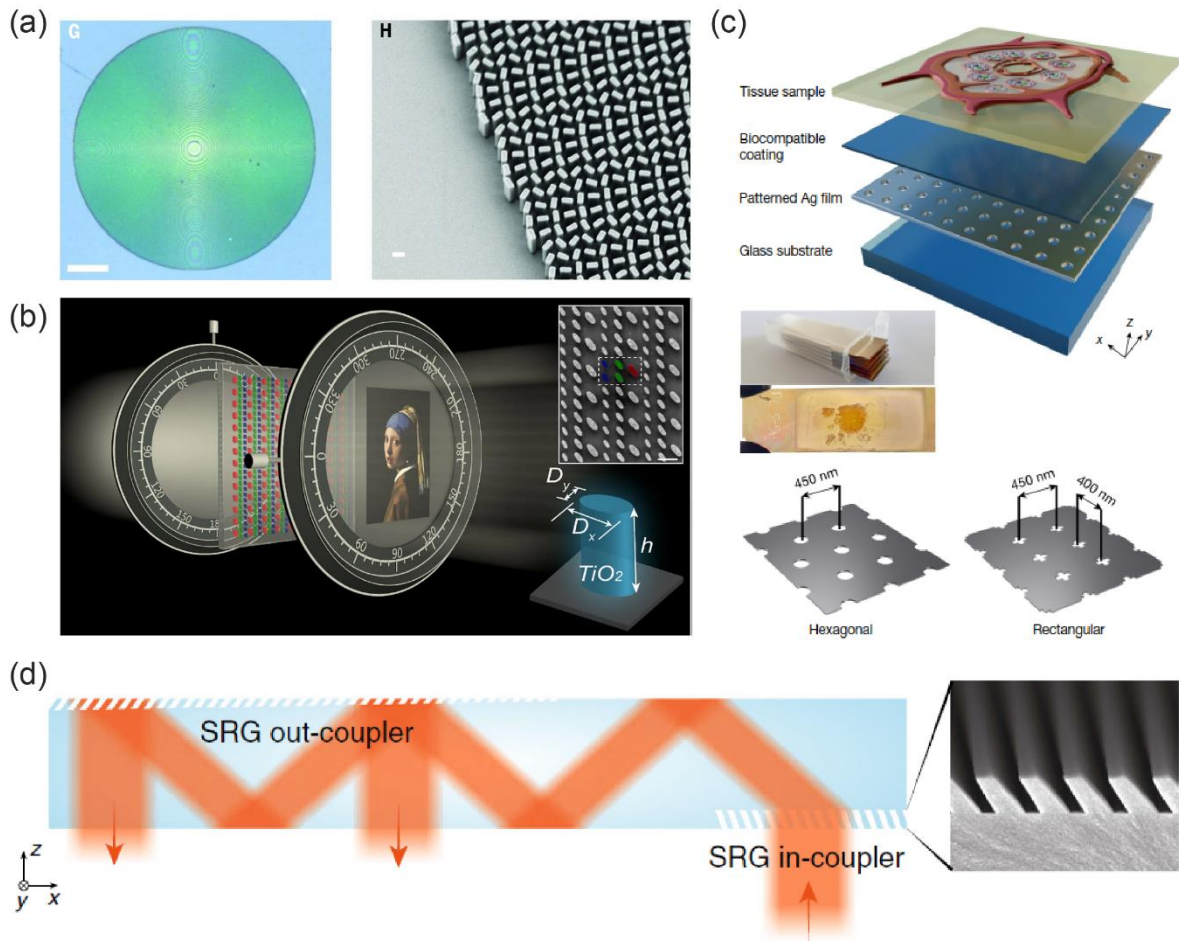


Figure 1-3 Novel optical applications using functional nanostructures. (a) Metalenses at visible wavelengths using TiO_2 nanorods⁴⁵. (b) High-resolution structural color painting using TiO_2 nanorods⁴⁸. (c) Plasmonically active microscope slides using metallic nanoholes³⁴. (d) Surface-relief waveguide for AR display using slanting nanogratings⁵².

Chapter 2 Patterning of High-aspect-ratio Nanogratings Using Phase-locked Two-beam Fiber-optic Interference Lithography

In this chapter, we demonstrate the fabrication of high-aspect-ratio nanostructures using the phase-locked two-beam fiber-optic interference lithography (2-FOIL) system. The key factors that affect the nanopatterning morphologies are numerically and experimentally investigated. The Dill model is applied in the numerical simulation to understand the effects of exposure dose and pattern contrast on the exposed photoresist grating profiles. Exposure experiments on our home-built 2-FOIL setup are conducted to demonstrate the suitability for manipulating the linewidth of photoresist gratings by tuning the exposure dose to achieve high aspect ratios over 6 at high pattern contrast thanks to the phase-locking mechanism. The high-aspect-ratio photoresist gratings serve as an excellent etching mask for subsequent pattern transfer into underlying silicon substrates for high-aspect-ratio silicon gratings. Using these high-aspect-ratio silicon gratings as the nanoimprint mold, a square nano-mesh is demonstrated by means of multiple-step nanoimprint lithography. The proposed phase-locked 2-FOIL system enables high pattern contrast under long exposure duration, making it a suitable tool for fabricating high-aspect-ratio grating structures.

2.1 Introduction

Periodic nanostructures such as gratings and pillars have been increasingly used in many emerging applications of plasmonics⁵³, metasurfaces⁵⁴, and optoelectronics⁵⁵. The performance of such components is critically dependent on not only their planar shape but also the vertical profile. Gratings with heights larger than linewidths, which means high

aspect ratio, are essential in many optical devices to achieve designed performance such as diffraction efficiency. In most nanofabrication processes, nanostructures in the photoresist with vertical sidewall and high aspect ratio are often necessary for reliable pattern transfer into underlying hard substrates through dry etching processes or pattern reverse with other functional materials by deposition and lift-off strategies. Therefore, to precisely control the nanopattern profiles becomes indispensable and a perfect lithography pattern becomes particularly predominant^{56,57}.

Interference lithography (IL) is one of the most adopted methods to fabricate large-area periodic structures such as gratings and pillar arrays. IL has been demonstrated with light sources of various wavelengths ranging from EUV^{58,59} to blue bands. In the past decades, IL has been achieved in various configurations such as wavefront-divided Lloyd's mirror type⁶⁰ and amplitude-divided multi-beam type^{28,61,62}, while the latter typically is preferred for large-area and high-quality patterning applications. Recently, we have developed an improved two-beam interference lithography configuration using fiber-optic components, named two-beam fiber-optic interference lithography (2-FOIL)²⁹, to realize unprecedented reconfigurability and automation that are needed for commercialized interference lithography patterning tools. With the actively-stabilized phase-locking mechanism, the 2-FOIL system can maintain the stability of the interference pattern during long exposure duration⁶³, which is essential to expose high-aspect-ratio gratings with narrow linewidth.

2.2 High interference pattern contrast

2.2.1 Setup of the phase-locked two-beam fiber-optic interference lithography

The schematic of our home-built 2-FOIL system is illustrated in Figure 2-1. The Gaussian beam from a longitudinal-mode single-frequency 405-nm diode laser is split into two coherent beams and coupled into two single-mode polarization-maintaining optical fiber cables through fiber couplers. The two sub-beams go through the flexible optical fiber cables and emit out from the fiber connectors. Due to the flexibility of the optical fiber cables, the angle between the two fiber ports can be adjusted arbitrarily, therefore creating interference patterns of widely tuneable periodicities. However, the employment of fiber-optic components also introduces new challenges. Particularly, thermal fluctuations around the two fiber cables will cause random variation in the phase difference between the two sub-beams. Therefore, an active stabilization mechanism containing a PID controller, an interferometry phase detector, and a piezoelectric actuator is implemented to compensate the fringe drifts and pattern quality. The active-stabilized phase-locking module enables our 2-FOIL system to achieve excellent pattern contrast with long exposure duration, therefore creating high-aspect-ratio photoresist gratings with narrow linewidth.

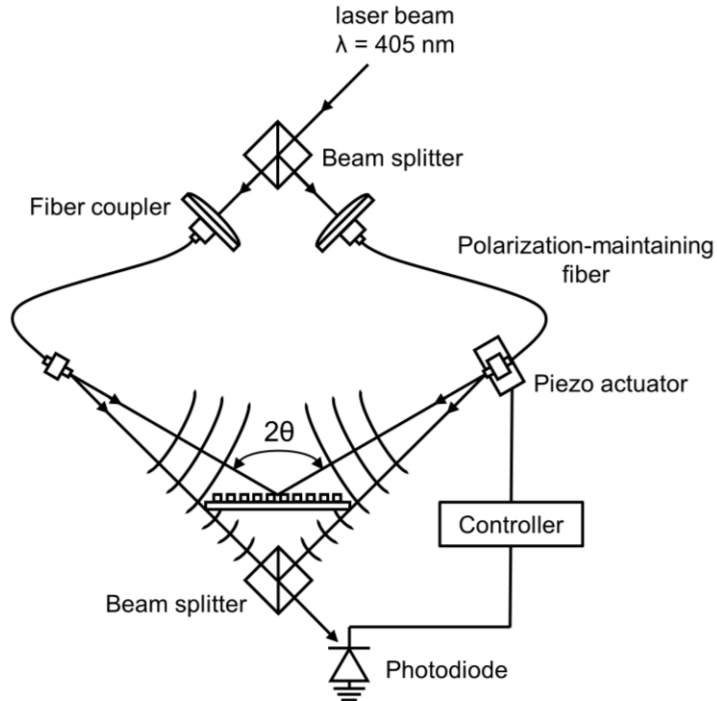


Figure 2-1 Schematic of the two-beam fiber-optic interference lithography system.

One critical parameter to estimate IL system performance is the interference pattern uniformity, which mainly serves as two aspects, the period and linewidth. The period is primarily determined by the mechanical and optical configurations such as the symmetry of the two beams, the difference of two-beam paths, and the tilting angle of the substrate, etc. The linewidth uniformity is conventionally affected by the exposure dosages and the interference pattern contrast, which will be discussed in the following. In our 2-FOIL system, single-mode optical fiber outputs an ideal circular Gaussian intensity profile, which has a non-uniform exposure intensity distribution over large-area substrate. Since the interference pattern is generated from two spherical waves, the exposed gratings are hyperbolic profiles instead of perfectly parallel lines. The schematic of the beam path is illustrated in Figure 2-2, where the practical interference period on the substrate can be expressed as⁶⁴

$$P(x) = \frac{\lambda}{\frac{L_1 \sin \theta_1 - x}{\sqrt{(L_1 \sin \theta_1 - x)^2 + (L_1 \cos \theta_2)^2}} + \frac{L_2 \sin \theta_2 + x}{\sqrt{(L_2 \sin \theta_2 + x)^2 + (L_2 \cos \theta_2)^2}}} \quad (2.1)$$

where λ is the laser wavelength, L_1 and L_2 are the distances from the fiber facet to the substrate (arm lengths) of the two beams, and θ_1 and θ_2 are the two-beam incident angles.

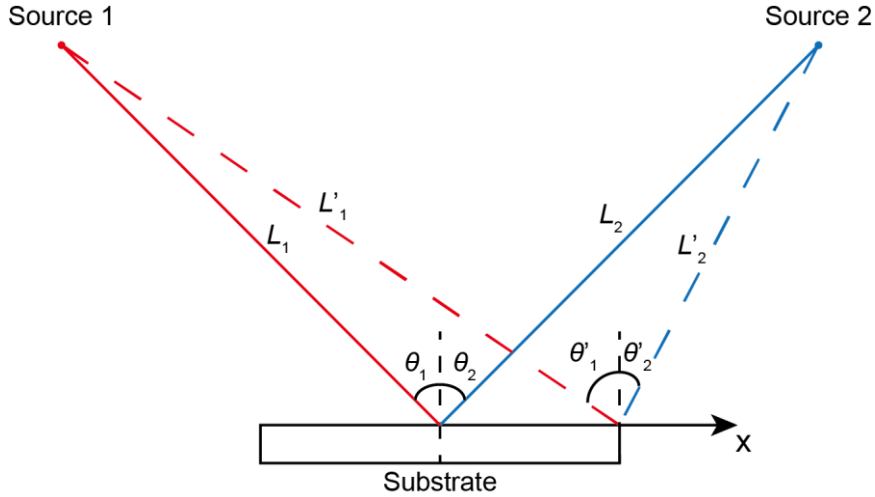


Figure 2-2 Schematic of the interference angle change of spherical beams on large-area planar substrate. The interference angle varies away from the center, which acts to the grating period variation.

To explore the most important factor that affects the period uniformity, the beam angles and arm lengths are investigated through numerical simulation where the reference angle is set as 30.4° and the reference length is fixed at 90 cm (Figure 2-3). When one of the interference beams is tilted 1° from the symmetry position, a nearly 8-nm shift would generate for exposing 400-nm-period nanogratings on 4-inch wafer. Similarly, a 10-cm asymmetry in the arm lengths would produce over 4-nm period variation over the 4-inch wafer. Therefore, both the angle and arm length accuracies highly relate to period uniformity in the IL exposure. Notably, our 2-FOIL system adopting flexible fiber-optics

has the great merit in easily adjusting and configuring the beam angles and arm distances, resulting in the homogeneous period uniformity.

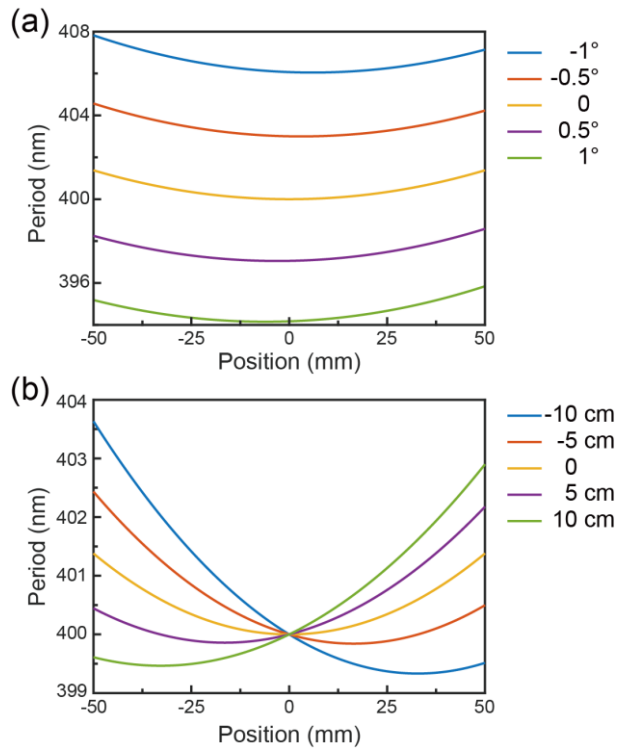


Figure 2-3 Simulated interference period as a function of position on the 4-inch substrate for non-ideal conditions. Period variation in terms of (a) two-beam angle asymmetry and (b) different arm lengths.

Besides, the linewidth uniformity is determined by several factors including the inequality of two beam intensities, non-uniform intensity distribution of Gaussian beam. These factors closely contribute to the interference pattern contrast, which is discussed in the following part.

2.2.2 Static interference pattern contrast

The contrast of the two-beam interference pattern on the photoresist significantly affects the exposed photoresist grating profiles including morphologies and linewidths.

There are mainly two types of factors, static and dynamic, that can affect the contrast. In our 2-FOIL system, static factors include the inequality of the two sub-beams, the diffused reflection in the surroundings, non-ideal polarization alignment, and the diffraction of the latent image, etc. Since our system enables easy tuning of intensity and polarization through the beam splitter and fiber coupler, the static interference pattern contrast can be simply determined by as the intensity distribution due to the Gaussian beams,

$$\gamma = \frac{I_{max} - I_{min}}{I_{max} + I_{min}} \quad (2.2)$$

The Gaussian beam intensity distribution can be calculated through,

$$I(z, r) = \frac{I_0}{1 + \left(\frac{\lambda z}{\pi \omega_0^2}\right)^2} \exp\left(-\frac{2r^2}{\omega_0^2 \left(1 + \left(\frac{\lambda z}{\pi \omega_0^2}\right)^2\right)}\right) \quad (2.3)$$

where λ is the laser wavelength, I_0 is the laser intensity at the center of the fiber facet, ω_0 is half of the fiber mode field diameter, r is the radial distance from the beam delivery axis, and z is the beam propagation distance. Assuming the two beams start with equal intensities at the fiber facets, the contrast of two Gaussian beams on the 4-inch wafer can be simulated in Figure 2-4. The results show the non-uniformity induced by two Gaussian beams can be negligible.

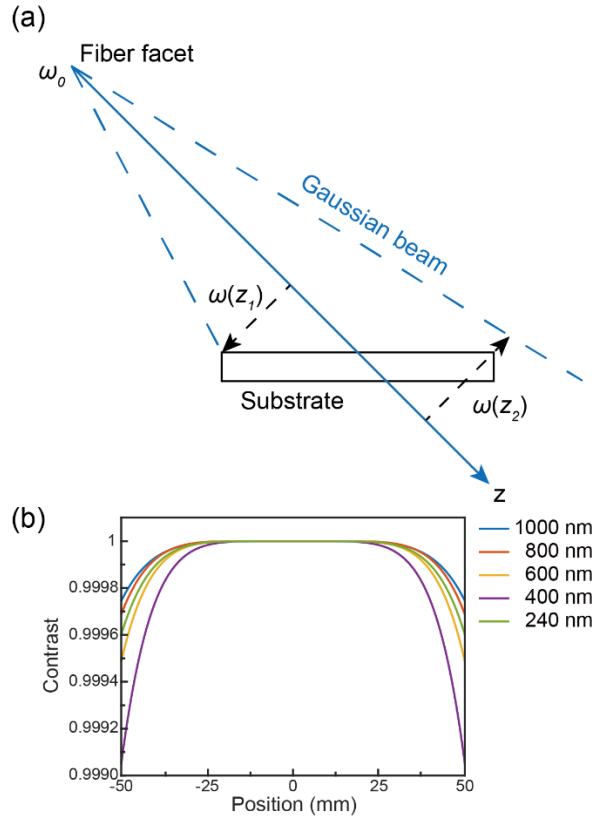


Figure 2-4 The static contrast analysis of two Gaussian beams on large-area substrates. (a) Schematic of Gaussian beam on large-area substrate. (b) Simulated static contrast as a function of position on the 4-inch substrate for different periods.

2.2.3 Dynamic interference pattern contrast

The interference contrast induced by the dynamic factors plays a crucial role in IL exposure dose that modulates the linewidth. Typical dynamic factors are mainly about thermal fluctuations and mechanical vibrations, which change with time. And the phase-locking system is mainly used to minimize the influence caused by dynamic factors, particularly, the thermal fluctuations. In our 2-FOIL system, the intensity profile of the interference pattern can be calculated as below,

$$I(x, t) = 2I_0 \left\{ 1 + \cos \left[\frac{4\pi}{\lambda} \sin \theta \cdot x + \Delta\varphi(t) \right] \right\} \quad (2.4)$$

where λ is the laser wavelength, θ is the half-angle between the two beams, I_0 is the intensity of the beam's incident on the photoresist (assuming the two beams are of equal intensities), x is the horizontal distance from the exposed center, and $\Delta\varphi(t)$ is the relative phase difference between the two beams caused by the thermal fluctuation. To address this, we have implemented the phase-locking system to minimize the impact brought by the random changes in the phase difference between the two beams due to thermal fluctuation and other environmental factors.

When the interference pattern randomly drifts due to the random change in the phase difference between the two beams, the actual dose profile on the photoresist can be obtained from:

$$D(x) = \int_0^T I(x, t) dt = 2D_0 \left[1 + \Gamma \cos \left(\frac{4\pi}{\lambda} \sin \theta \cdot x \right) \right] \quad (2.5)$$

where T is the total exposure time, $D_0=I_0 \cdot T$, and Γ is the dynamic pattern contrast, which can be estimated by:

$$\Gamma = \frac{\text{MAX}[D(x)] - \text{MIN}[D(x)]}{\text{MAX}[D(x)] + \text{MIN}[D(x)]} \quad (2.6)$$

where the maximum and minimum value are obtained within one period of the interference fringe. The contrast is a key factor used to estimate the stability of the laser interference pattern.

In our 2-FOIL system, typical variations of the phase difference between the two beams can also be acquired using the phase-locking interferometry setup and plotted as shown in Figure 2-6, when the phase-locking system is off and on, respectively. The corresponding contrasts can be calculated to be 0.3397 and 0.9993, respectively, which

shows the superior contrast-enhancing performance of the phase-locking mechanism in our 2-FOIL system.

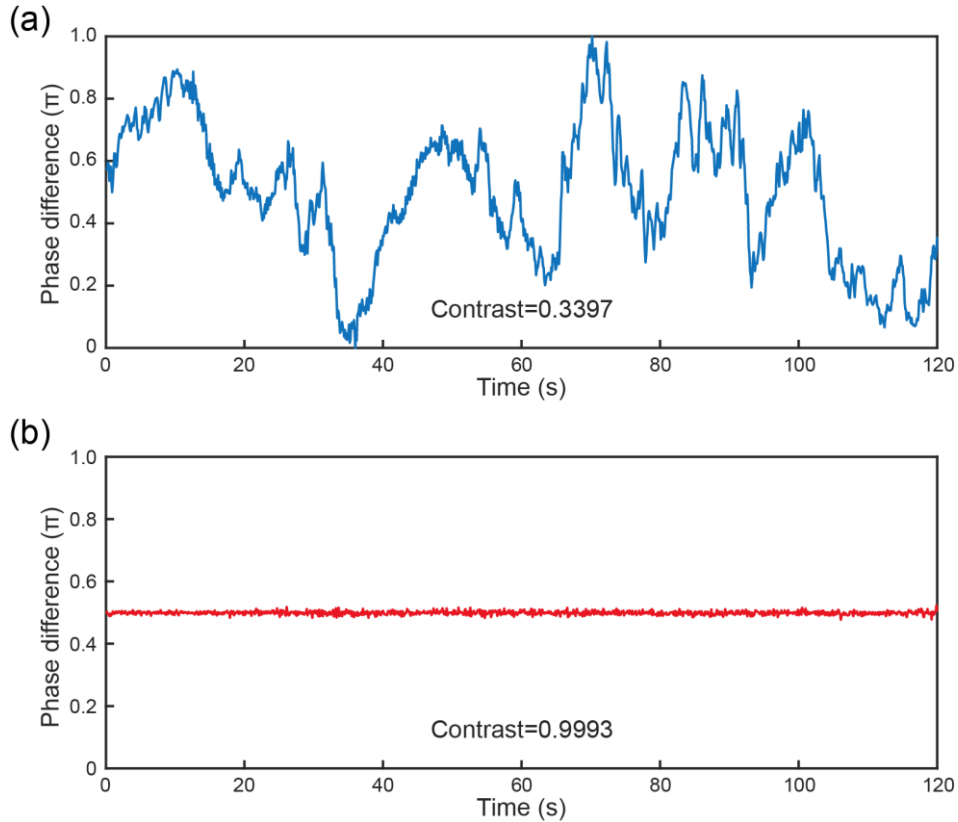


Figure 2-5 The dynamic contrast enhanced by the phase-locking system. The varying phase differences for (a) the open-loop operation without the phase-locking and (b) the closed-loop operation with the phase-locking.

2.3 Numerical exposure model

The property of the photoresist used in the exposure is important to the final profile of the exposed grating structures. In this part, we use positive-tone photoresist, which will be dissolved in the subsequent development process if exposed with sufficient dose. The positive photoresist is generally composed of a photoacid compound (PAC), a base resin and a solvent, of which PAC is the photoactive ingredient. According to the Dill model^{65,66},

$$M = e^{-CIt} \quad (2.7)$$

where M is the normalized concentration of unbleached PAC remaining in the resist, C is the measurable constant of the photoresist in the Dill model, I is the light intensity, and t is the exposure time. This relation indicates the propagation and evolution of PAC during the exposure so that we can simulate the photoresist latent image with the known intensity distribution of the interference pattern.

In this model, we assume no reflection occurs at the bottom of the photoresist because we use an anti-reflective coating (ARC) layer to eliminate the reflection. Parameters of the development process, such as the developer concentration and development time, will also affect the photoresist profiles. However, in this study, we will not investigate these factors but just keep the same development condition every time⁶⁷. To simplify the numerical simulation, in this research, we utilize the exposed latent image in the photoresist to simulate the profile of gratings patterned by the phase-locked 2-FOIL system.

For the ideal photoresist, the latent image under different exposure time can be shown in Figure 2-7a represented by the local dose absorbed by the photoresist under certain exposure conditions. During the development, the photoresist will be dissolved when the specific position absorbs dose. But for the real condition in the photoresist, the thickness of photoresist cannot be reduced after development until the exposure dose reaches the threshold, which is the maximum dose to keep the photoresist undeveloped. By assigning a certain threshold dose to the exposed photoresist, we can get the simulated latent image profiles in Figure 2-7b. In this simulation, the top of the photoresist is flat, and the linewidth of the latent grating is relatively wider than the ideal profile.

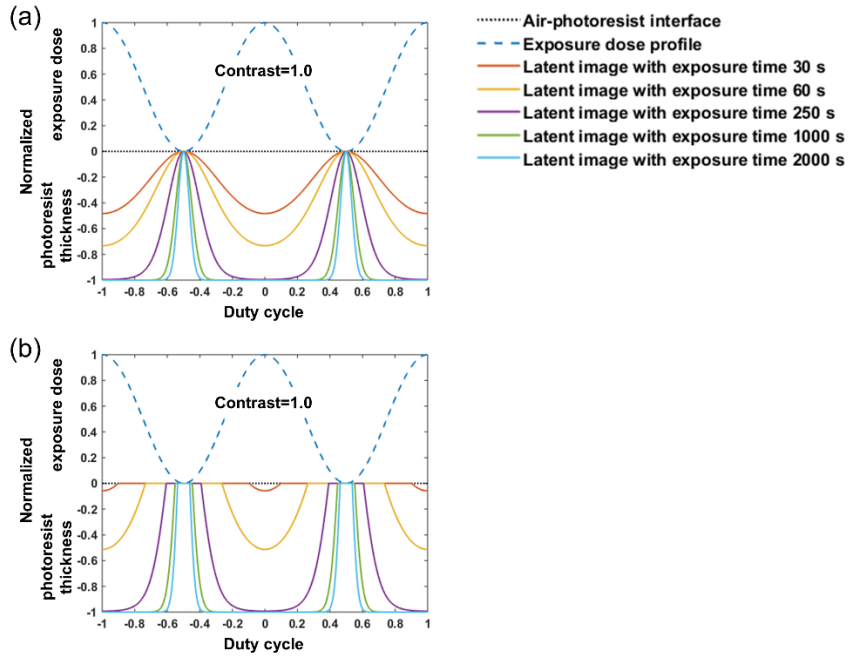


Figure 2-6 Simulation on the effect of the exposure time on the latent image and the developed photoresist grating profile. (a) Simulated ideal and (b) real photoresist profiles of the latent image with different exposure time of 30 s, 60 s, 250 s, 1000 s, and 2000 s, respectively.

The contrast is of great importance which affects the photoresist pattern most. Figure 2-8 shows the latent images at the same exposure time but with different contrasts (0.95, 0.9, 0.8). The aspect ratio of the photoresist latent image decreases when the contrast decreases, which is more obvious for long exposure time. Therefore, fulfilling the requirement for higher-aspect-ratio structure in the photoresist needs higher interference pattern contrast. Meanwhile, the linewidth of a grating for a given periodicity can be manipulated simply by changing the exposure dose on the condition of high pattern contrast.

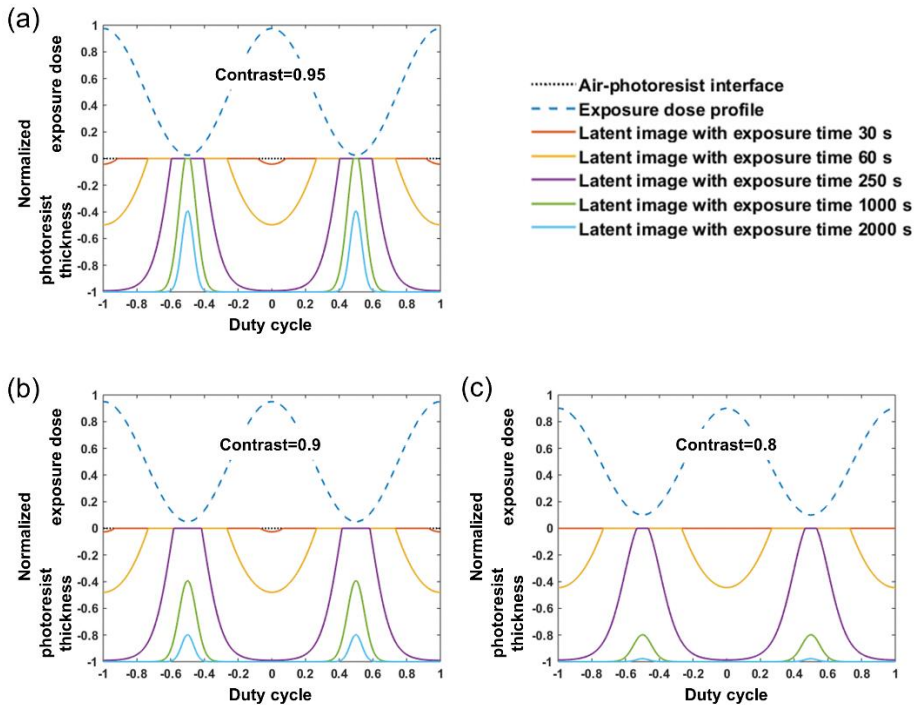


Figure 2-7 Simulation on the effect of the interference pattern contrast on the latent image and the developed photoresist grating profile. Simulated photoresist latent images of different contrasts of (a) 0.95, (b) 0.9, and (c) 0.8 with five groups of exposure time of 30 s, 60 s, 250 s, 1000 s, and 2000 s, respectively.

2.4 Experimental demonstrations using high-contrast interference lithography

2.4.1 Linewidth control by exposure doses

We experimentally explore the capability of patterning high-aspect-ratio and narrow-linewidth photoresist gratings using the phase-locked 2-FOIL setup, as well as relationship between exposure dose and linewidth. Silicon wafers coated with a 200-nm-thick layer of ARC (AZ BARLi II 200) and a layer of positive photoresist (AZ MiR 701, diluted in 1.5: 1 with PGMEA) of 330 nm are used as the substrates. The samples are exposed to 1- μm -period grating patterns at different exposure doses. After developing under the same

condition using AZ 726 MIF developer, photoresist gratings of different linewidths are obtained. From the SEM images in Figure 2-9a, the linewidth significantly decreases when the exposure dose increases.

For an exposed duty cycle d , according to Eq. (2.5), we can obtain $D_c = 2D_0[1 - \Gamma \cos(\pi d)]$, where D_c is the critical dose for clearing the exposed photoresist and D_0 corresponds to the actual exposure dose. Therefore, different exposure doses will lead to different duty cycles for a fixed critical dose D_c . Through the measurement of the exposed duty cycles under different exposure doses D_0 , we can get the linear model of $D_0^{-1} \sim \cos(\pi d)$ relation,

$$\cos(\pi d) = \frac{1}{\Gamma} - \frac{D_c}{2\Gamma} D_0^{-1} \quad (2.8)$$

By fitting the linear model, the contrast Γ can be determined as the reciprocal of the intercept of the linear fitting curve. Our experimental data is plotted in Figure 2-9b and the contrast Γ is determined to be 0.8583 based on this fitting. The difference between the contrast obtained from the fitting of the exposed linewidth and exposure doses, which is calculated to be 0.8583, and that obtained from the phase-locking interferometry data, which is determined to be 0.9993, is mainly because the phase-locking interferometry data does not consider static factors affecting the contrast, as mentioned in the last section. Besides, the power stability of the laser in a long working duration also contributes to the non-ideal exposure patterns and therefore a lower contrast.

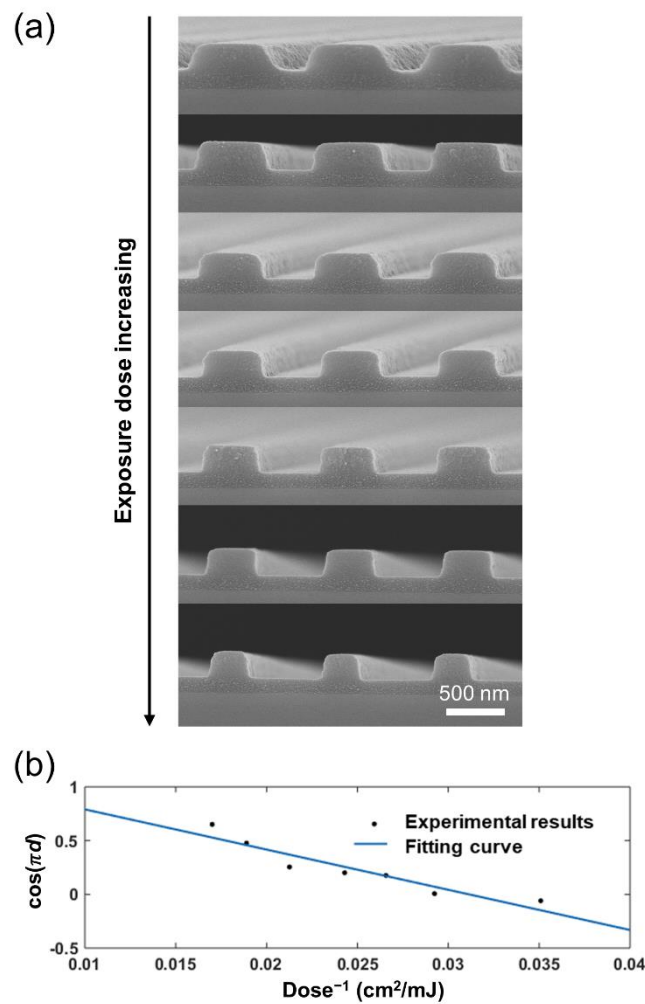


Figure 2-8 Experimental results showing the exposure dose modulating the linewidth. (a) SEM images of 1000-nm-period gratings with different exposure doses of 28.5, 34.2, 37.6, 41.2, 47.0, 52.9, 58.8 mJ/cm^2 , respectively. (b) A linear fitting curve of calculated $\cos(\pi d)$ from SEM images in (a) versus $Dose^{-1}$ recorded in experiments.

2.4.2 High-aspect-ratio nanostructures

The good linewidth controllability of our phase-locked 2-FOIL system can be demonstrated by patterning high aspect-ratio photoresist gratings with periodicity ranging from 240 nm to 1.0 μm . For different periodicities, the corresponding thickness of photoresist should be adjusted according to the dilution ratio of the photoresist and

parameters of the spin coating. Under the appropriate exposure dose and development duration, Figure 2-10 shows the SEM images of the high-aspect-ratio photoresist gratings of rectangular profile and vertical sidewall patterned by the phase-locked 2-FOIL system.

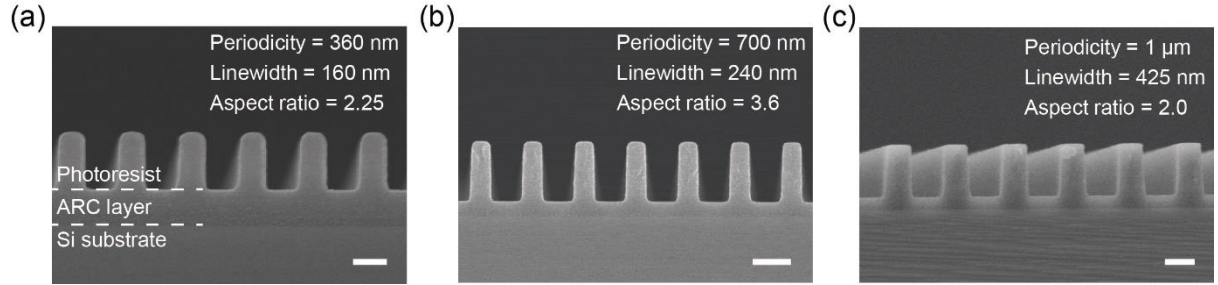


Figure 2-9 Nanogratings with rectangular profiles fabricated by phase-locked 2-FOIL. SEM images of (a) 360-nm-period, (b) 700-nm-period, and (c) 1- μ m-period gratings. Scale bars, (a) 200 nm, (b, c) 500 nm.

The linewidth can be further shrunk by continuously increasing the exposure dose. As examples, Figure 2-11a-b exhibit the SEM images of 240-nm-period gratings with a 50-nm linewidth and 850-nm period gratings with a 135-nm linewidth, and corresponded aspect ratios are 3.0 and 6.25. Using thicker photoresist, we successfully fabricated 850-nm period gratings with a 335-nm linewidth and a 1.95- μ m height, corresponding to an aspect ratio of 5.8, as shown in Figure 2-11c.

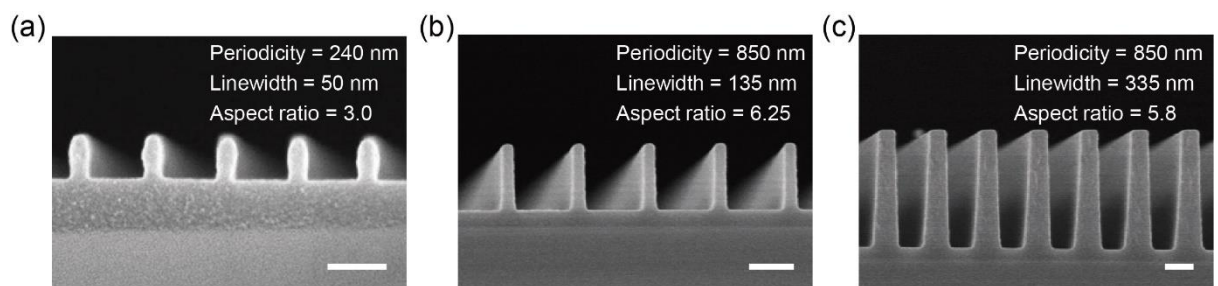


Figure 2-10 Nanogratings with high aspect ratio fabricated by phase-locked 2-FOIL. SEM images of (a) 240-nm-period, (b) 850-nm-period, and (c) 850-nm-period gratings. Scale bars, (a) 200 nm, (b, c) 500 nm.

2.4.3 Wafer-scale nanopatterning

In the last section, we mentioned that the high-contrast interference pattern, enabling a wide exposure latitude, benefits the wafer-scale nanopatterning with relatively uniform linewidth even under the non-uniform Gaussian beams. Figure 2-10 shows the simulated and measured intensity distribution when exposing 400-nm-period nanogratings on a 4-inch wafer, of which the intensity reduces over 50% from center to the edge.

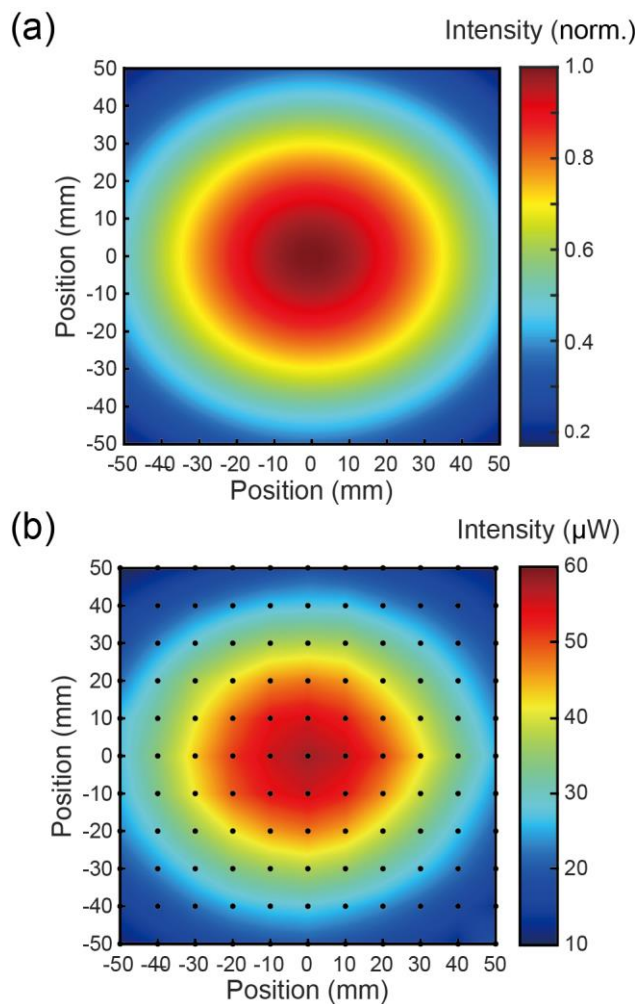


Figure 2-11 Intensity distribution of Gaussian beams when exposing 400-nm period nanogratings. (a) Plot of normalized calculated Gaussian beam intensity distribution on 4-inch wafer. (b) Plot of measured intensity distribution on 4-inch wafer using interpolation fitting.

Exposed by the non-uniform Gaussian beams, the dynamic interference pattern contrast becomes quite important because it can enlarge the IL exposure latitude for further maintaining the pattern completeness during long exposure duration. Figure 2-12 demonstrates a 3-inch wafer carrying of 400-nm-period nanogratings, showing the uniform diffraction. By recording SEM images along the wafer diameter (Figure A-2) and characterizing the dimensions, the period has less than 0.03% variation (404 ± 1 nm) over the diameter and the linewidth varies 15% (131 ± 20 nm) along 80% of wafer diameter.

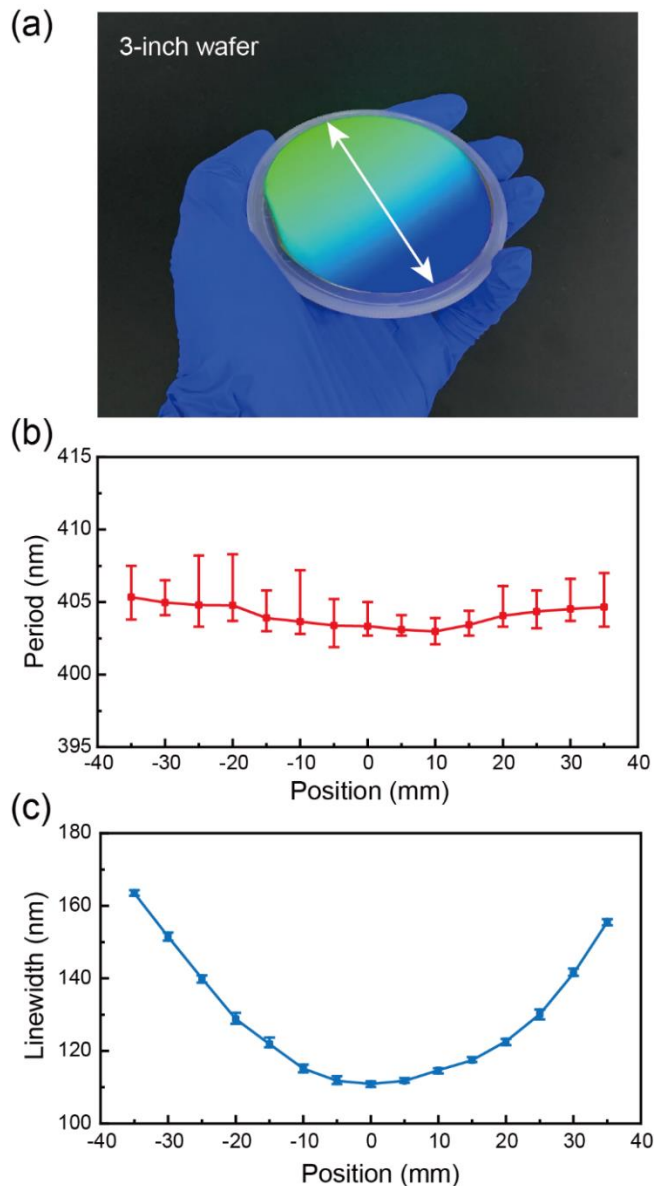


Figure 2-12 Large-area nanopatterning using high-contrast 2-FOIL on 3-inch wafer. (a) Photograph of 3-inch wafer carrying 400-nm-period gratings. (b) The period distribution showing 0.3% variation. (c) The linewidth distribution showing 15% uniformity along 80% of the diameter on 3-inch wafer.

2.4.4 Pattern transfer results

Pattern transfer into hard substrates such as silicon, fused silica and sapphire is commonly necessary in various applications. And high-quality NIL usually also needs

nanostructures on hard substrates as the nanoimprint mold^{68,69}. Transferring the photoresist grating patterns into the underlying hard substrates typically involves reactive ion etching, where the height and vertical profile of the photoresist patterns are essential to achieve an ideal transferred pattern. Using the high-aspect-ratio and narrow-linewidth photoresist nanogratings achieved using our phase-locked 2-FOIL setup, we also demonstrate the transferred nanogratings in the hard substrates as shown in Figure 2-13.

With the vertical sidewall and high aspect ratio of the photoresist gratings, we can directly etch the underlying substrates without using additional nanofabrication processes such as angle deposition. Oxygen reactive ion etching (RIE) is first used to remove the ARC layer below the photoresist gratings. After O₂ RIE, we use the stack of the photoresist and the ARC as the mask to directly etch the underlying silicon substrate in inductively coupled plasma (ICP) mode using SF₆/CHF₃ or SF₆/O₂ recipe. The SEM images in Figure 2-13a and 2-13b show two typical directly etched silicon gratings. We can also convert the photoresist pattern into a Cr mask using e-beam evaporation of Cr and the lift-off process, as shown in Figure A-1. In this process, the high-aspect-ratio and vertical grating profile in the photoresist patterns also help to achieve a good quality in the lift-off process. After the subsequent ICP etching with the Cr mask, nanograting patterns with a reversed profile can be transferred into the silicon substrates with sub-30 nm grooves, slanted profiles, or wide-linewidth gratings (Figure 2-13c-e). Using silicon mold in Figure 2-13e, we further fabricate large-area square nano-mesh patterns through multiple-step NIL, as shown in Figure 2-13f.

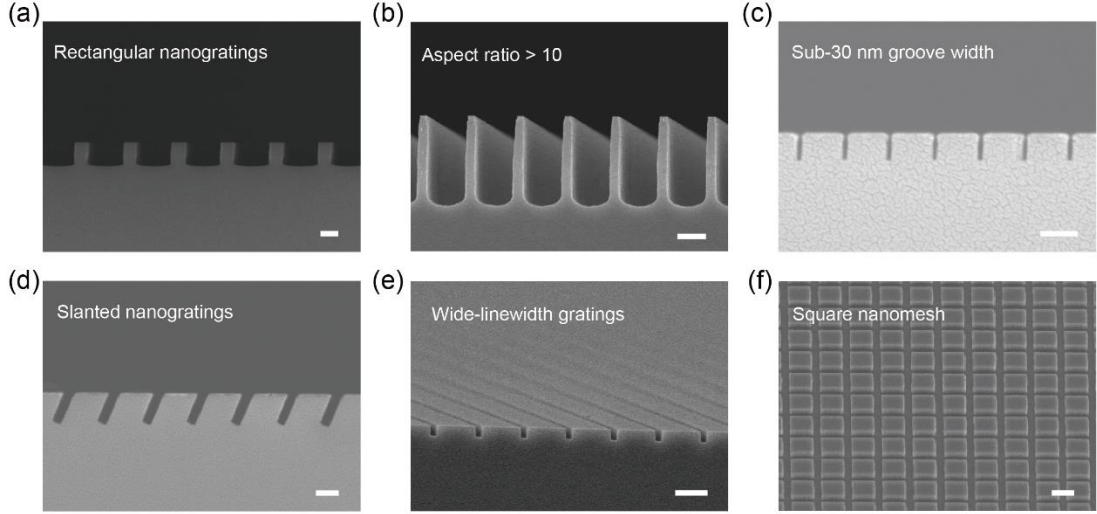


Figure 2-13 SEM images of diverse pattern transfer results. Etched results using photoresist as mask with different recipes, (a) 360-nm-period rectangular gratings. (b) 850-nm-period high-aspect-ratio gratings. Etched results using a pattern-reversed Cr mask, including (c) Sub-30-nm grooves, (d) 400-nm-period slanted gratings, (e) 700-nm-period nanogratings. (f) Nanomesh structures fabricated by the silicon mold in (e) with multiple NIL processes. Scale bars, 100 nm (a, c, d), and 500 nm (b, e, f).

2.5 Summary

In this chapter, we have demonstrated patterning high aspect-ratio photoresist gratings using our home-built phase-locked 2-FOIL system. Numerical simulation based on the Dill model and experimental characterization are used to investigate the effects of the contrast of the interference patterns and the exposure dose on the grating profiles including the aspect ratio and the linewidth. High-aspect-ratio photoresist gratings of different periodicities are demonstrated using our 2-FOIL system in long exposure duration, which proves the pattern stability thanks to the active phase-locking mechanism. Using the high-aspect-ratio patterns as the etching mask, we successfully transferred the pattern into the silicon substrate to fabricate silicon molds of high-aspect-ratio gratings. Through the

multiple-step nanoimprint lithography using the fabricated high-aspect-ratio grating mold, a square nanomesh can be fabricated.

Chapter 3 A Numerical Model for Optimizing Interference Lithography on Multi-layer Substrates

Compared with other lithographic techniques, IL is superior in fabricating nanoscale periodic structures on large areas. In **Chapter 2** we introduced a numerical model to simulate the photoresist evolution using the IL dose distribution and the Dill model. However, the real IL process contains more complex conditions^{70,71} such as the multi-layer substrate composed of transparent and metallic materials that may result in serious standing waves, which seriously affects the morphology of exposed patterns. Involving optical theories and material properties, the standing wave phenomenon cannot be ignored in both numerical calculation and practical exposure. Using the classic tri-layer resist process as an example, the mechanism of the light interaction in the photoresist is first studied by applying the transfer matrix method (TMM) and finite-difference time-domain (FDTD) analysis. The contrast of electric field distribution in the photoresist is proposed to quantitatively characterize the condition of standing wave generation and can be used for optimizing the tri-layer resist combination to improve the exposed pattern quality. Based on this process optimization strategy, the tri-layer resist process is demonstrated with high pattern transfer fidelity. The optimization strategy can be further applied to other complex substrates for exposing high-quality nanostructures, which benefits the nanofabrication processes for diverse functional materials.

3.1 Introduction

3.1.1 Standing wave phenomenon and anti-reflective coating

In optical lithography processes, the exposure beam irradiates through the photoresist on the substrate, where the light usually reflects at the photoresist/substrate interface. The reflected beam interferes with the incident beam, resulting in the non-uniform exposure intensity distribution along the photoresist depth, which is called the standing wave phenomenon^{72,73}. Particularly in IL process, the standing wave significantly deteriorates the nanopattern because the IL-exposed structures have similar dimensions to the standing wave. Figure 3-1a shows the typical IL-exposed photoresist nanogratings affected by the standing wave, showing a poor sidewall morphology and linewidth uniformity.

To address this, employing an anti-reflective coating (ARC) between the photoresist and substrate is the most adopted approach to reduce the standing wave. The thickness and optical properties (refractive index and extinction coefficient) of ARC determine the anti-reflective performance. In contrast, Figure 3-1b shows the exposed photoresist gratings with ARC, showing improved morphologies of straight sidewalls and smooth lines. Separating the resist from the substrate, the ARC layer also enhances the adhesion between the two layers, as well as avoids the potential defects of footing or scumming.

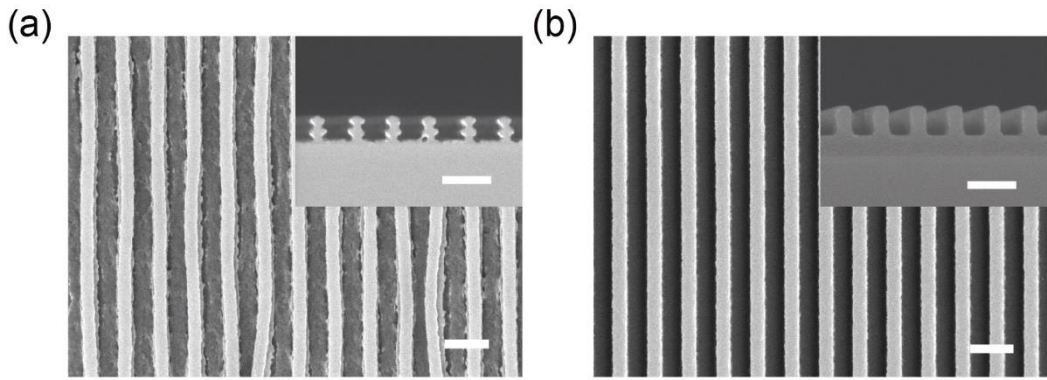


Figure 3-1 The standing wave phenomenon reduced by ARC. (a) SEM images of 400-nm-period gratings without ARC showing distorted lines and rough sidewalls. (b) SEM images of 400-nm-period gratings with ARC showing smooth lines and straight sidewalls. Scale bars, 500 nm.

However, since most ARC materials are non-photosensitive, an ARC open process should be proceeded to expose the underlying substrate before the subsequent etching or deposition. Thus, the isotropic etching should be considered in the ARC open process because it directly affects the desirable feature sizes. Since the photoresist and ARC have similar chemical compositions, these two layers feature the same etching rate in ARC open process. Meanwhile, the resist pattern also suffers lateral linewidth loss caused by the isotropic etching, which especially cannot be ignored when the feature sizes are down to sub-200 nm (Figure 3-3). Therefore, it is necessary to develop a process strategy that simultaneously satisfies anti-reflection performance and high-fidelity pattern transfer.

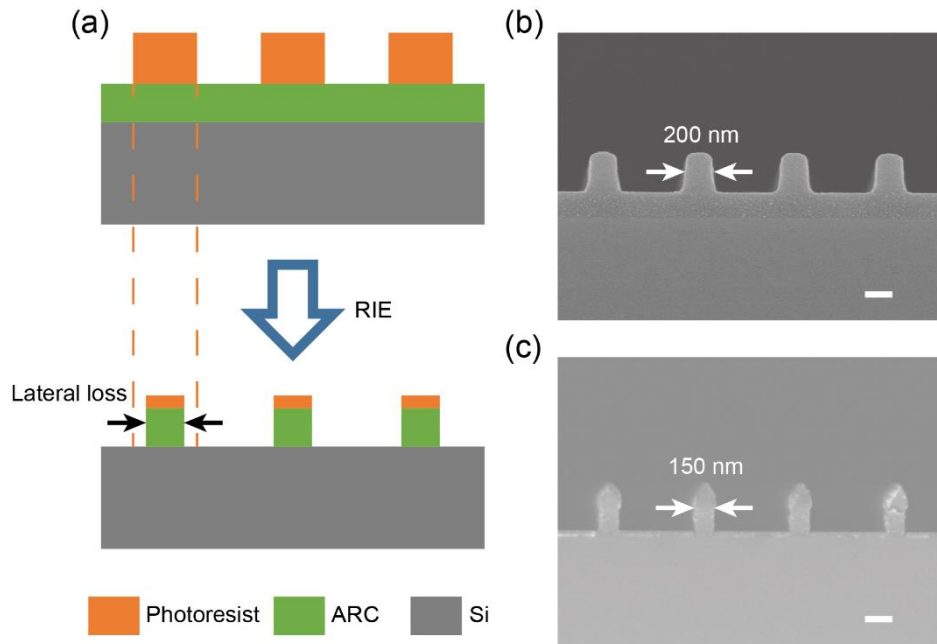


Figure 3-2 The lateral linewidth loss induced by ARC open process. (a) Schematic of lateral linewidth loss of resist structures after ARC open process using RIE. SEM images of nanogratings (b) before and (c) after ARC open process, showing a 50-nm linewidth loss. Scale bars, 200 nm.

3.1.2 High-fidelity tri-layer resist process

Regarding the above issues, a tri-layer resist (TLR) process has been proposed for high-fidelity pattern transfer by implementing a hard interlayer between the photoresist and ARC to enhance the etch selectivity^{74,75}, which is shown in Figure 3-3. In the sandwich structures of photoresist/interlayer/ARC, the standing wave mitigation can be sufficiently retained by the ARC layer and the etch selectivity can be greatly enhanced by alternately using polymeric and hard interlayer etching masks. First the interlayer is etched by the IL-exposed resist nanopattern, and then the polymeric ARC layer can be etched deeply using the hard interlayer, forming undercut profiles. The undercut enables easy deposition and lift-off processes so that the underlying substrates could be etched by Cr mask as

nanoimprint molds or evaporated with functional material as nanodevices. However, introducing the interlayer also brings the optical mismatch in optical lithographic processes, of which the unsuitable interlayer thickness or material may cause worse standing waves⁷⁴. Therefore, the material and thickness of TLR stack should be well-designed.

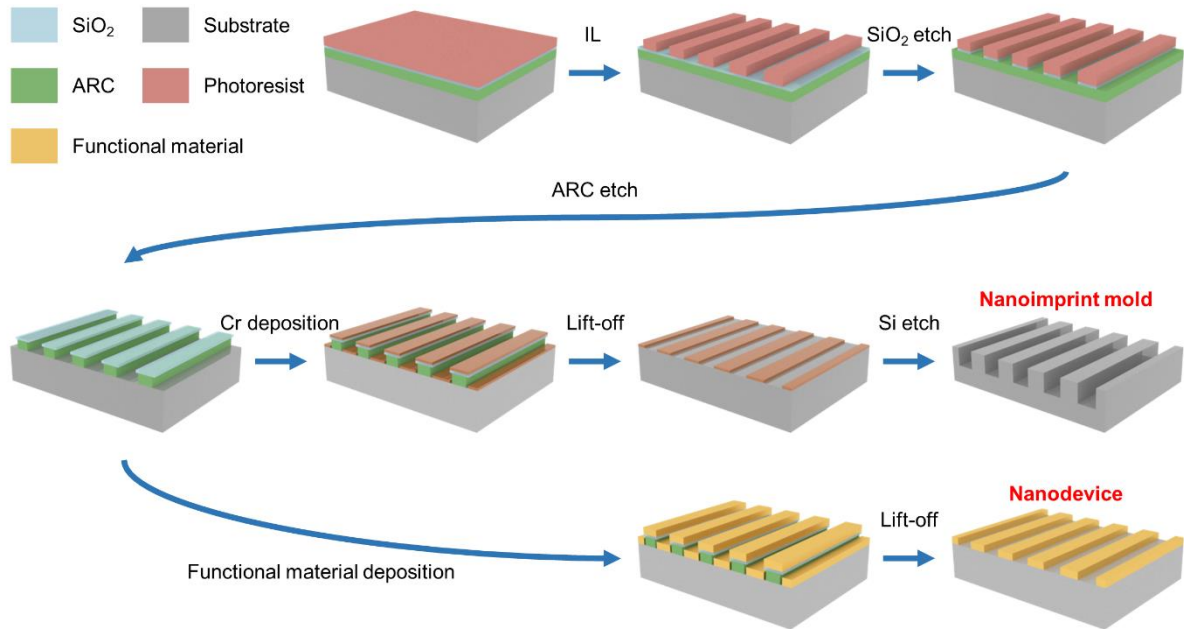


Figure 3-3 Schematic of high-fidelity tri-layer resist process for the fabrication of nanoimprint mold and functional nanodevice. Before spin-coating the photoresist, ARC and interlayer (SiO₂) layers are coated on the substrate. The substrate is patterned using IL followed by etching of SiO₂ and ARC to form undercut profiles. For the nanoimprint mold fabrication, the substrates could be performed by the Cr evaporation, lift-off, and etching processes. For the nanodevice fabrication, functional material could be evaporated followed by lift-off.

3.2 Numerical modeling of interference lithography on multi-layer substrates

To obtain a high-quality lithographic pattern that can be used in TLR process, the light interaction at each interface and electric field distribution in the photoresist are investigated through numerical modeling approaches. In the model, the refractive index n and the extinction coefficient k are the most important characteristics of each material, which are obtained from the spectroscopic ellipsometry characterization (Figure 3-4) or from the reference⁷⁶. Using TLR structure as the example, TMM analysis and FDTD simulation are performed to investigate the best parameter for IL.

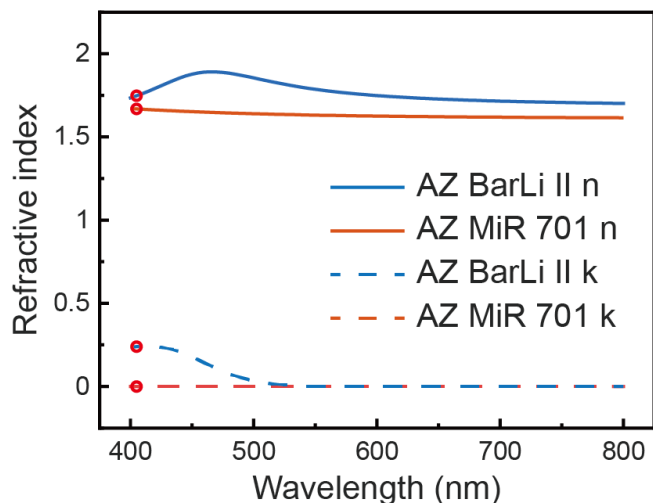


Figure 3-4 Results of measured refractive indices n and extinction coefficients k versus wavelength for ARC (AZ BarLi II 200) and photoresist (AZ MiR 701) via spectroscopic ellipsometry measurements.

3.2.1 Reflection above the photoresist interface

Using TMM analysis (details in Figure B-1), the reflectivity versus ARC thickness is plotted by applying refractive indices and extinction coefficients of several commonly used nanofabrication materials (Table 3-a) in Figure 3-5a. In this simulation, the basic process

configurations are 300-nm-thick photoresist, 25-nm-thick interlayer, and 400-nm-period interference pattern. The curves using Si, TiO₂ and SiO₂ as the interlayer will experience strongly swing characteristics, of which the total reflectivity of SiO₂ is relatively low. The first and second reflective minimal values can be down to 1.6% and 0.2%, respectively. Due to the better optical match with ARC in refractive indices, HfO₂ 和 Al₂O₃ feature stable reflective curves. Especially when the ARC thickness is thick (>200 nm), the reflectivity is approaching to zero. However, SiO₂ is still preferred as the interlayer because it can achieve a sufficiently low reflectivity no matter when the ARC is thin (< 100 nm) or thick (>180 nm), which suits diverse occasions for nanopatterning.

Table 3-a Refractive indices for Interlayer material

Interlayer material	Index ($\lambda=405$ nm)
SiO ₂	1.4836
HfO ₂	1.9348
Al ₂ O ₃	1.7857
TiO ₂	2.8717
Si	5.4376-0.3421i

Figure 3-5b shows the results for SiO₂ with different thicknesses as the interlayer. The introduction of SiO₂ interlayer enhances the swing phenomenon of reflectance curves, especially for the ones with thicker SiO₂. It is worthy to note that the troughs of the curves (known as the reflectance minimums) also become less, which benefits the standing wave elimination. Thus, it is necessary to optimize the ARC thickness in the TLR process to acquire the best exposure quality. Since the exposed period is angle-dependency, we also compare the reflectivity by assigning different periods (Figure 3-5d). When assigning the exposed nanopattern with larger periods (400 and 240 nm), the minimums of the swing

curves shift to the larger ARC thickness, which further demonstrates that a suitable thickness of ARC is very crucial in the interference exposure step of TLR process.

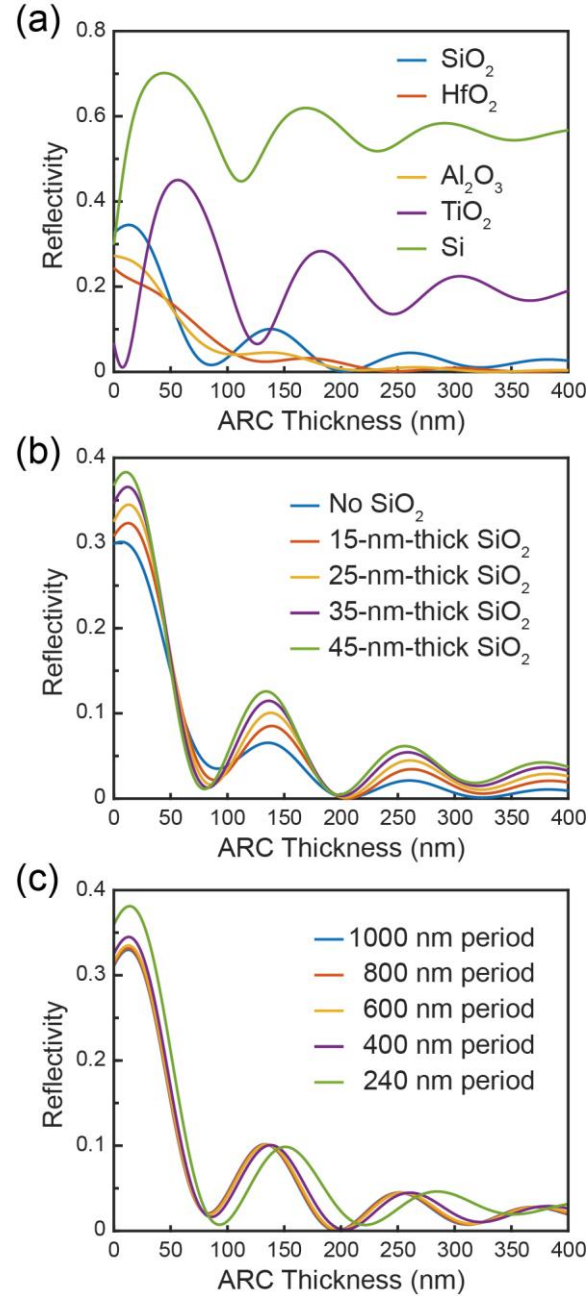


Figure 3-5 Numerical modeling results for the reflectivity at the boundary between the photoresist and underlying interlayer. Simulated reflectivity vs ARC thickness with (a) different interlayer materials, (b) different SiO_2 thicknesses, and (c) different periods.

3.2.2 Contrast of electric field distribution in photoresist

To further demonstrate the reliability of the numerical modeling, FDTD simulation is also employed to explore the electric field distribution in the photoresist of TLR stack. Calculating the spatial distribution of the electric field, a contrast parameter can be extracted to quantitatively evaluate standing wave, which is expressed as

$$\gamma = \frac{\text{MAX}[E(x)] - \text{MIN}[E(x)]}{\text{MAX}[E(x)] + \text{MIN}[E(x)]} \quad (3.1)$$

where $E(x)$ is the simulated electric field distribution in the photoresist. The contrast approaching to 0 means no standing wave is generated and vice versa. By sweeping the thicknesses in TLR combinations, the contrast distribution is mapped versus ARC and SiO_2 thicknesses in Figure 3-7 with 400 and 240-nm periods. For 400-nm period, the best ARC thickness locates around 200 nm while that of 240-nm period is about 80 nm. It is worth mentioning that a thinner ARC benefits the situations when exposing nanostructures with sub-100 nm dimensions.

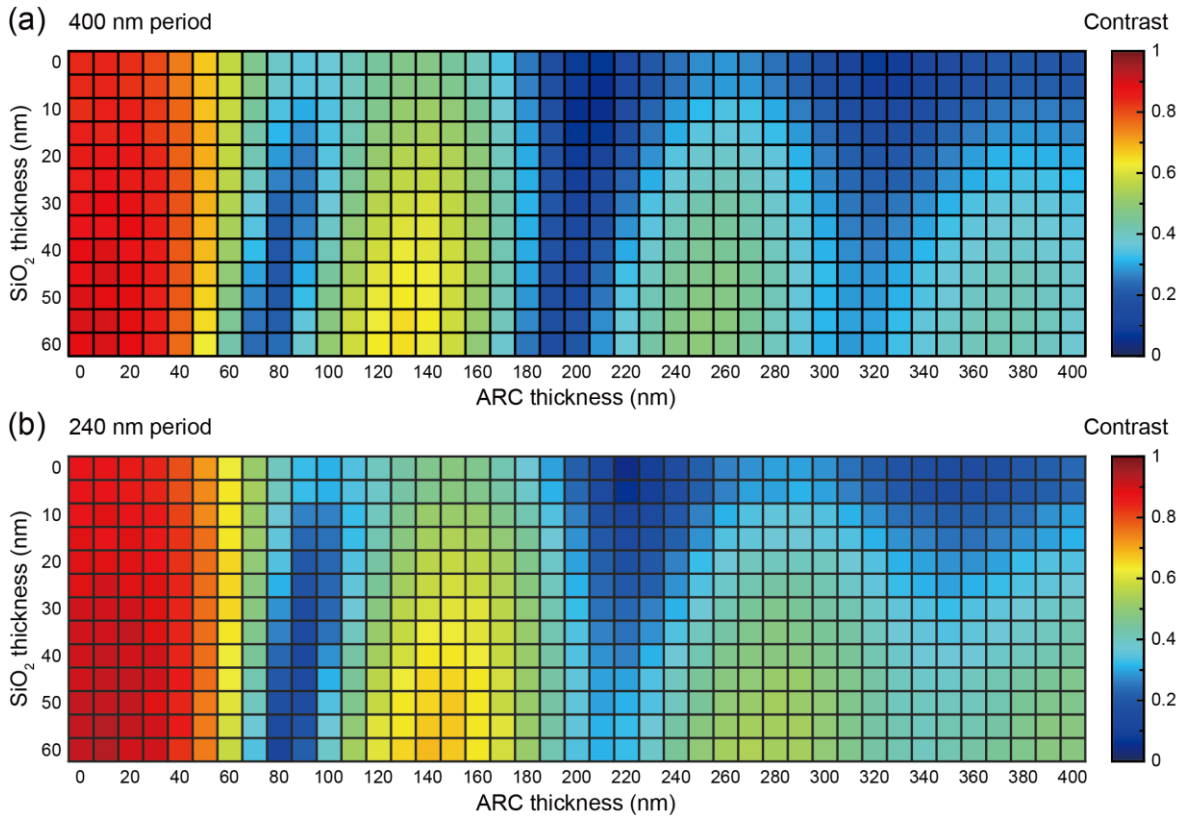


Figure 3-6 Contrast distributions versus thicknesses of SiO_2 and ARC for exposing nanostructures of different periods, (a) 400 nm and (b) 240 nm.

To further investigate the mechanism of standing wave phenomenon in TLR combinations, the simulated electric field profiles are illustrated in Figure 3-8 with typical ARC thicknesses of 80/140/210 nm and SiO_2 thicknesses of 15/25/35/45 nm. In the FDTD configuration, where the photoresist thickness and interference period are fixed at 300 and 400 nm. The stacks with 140-nm-thick ARC experience the strongest standing wave with obvious swing profiles, which are generated by the constructive interference between the incident and bottom reflective laser beams. Increasing the SiO_2 layer even deteriorates the contrast. However, the standing wave phenomenon can be effectively mitigated by the 80-nm-ARC combinations, where a suitable ARC thickness enables the destructive interference in the photoresist. In this situation, increasing SiO_2 thickness introduces the decreasing in standing wave as well as the contrast. For the results of 210-nm ARC, the

standing wave phenomenon was greatly eliminated due to not only the destructive interference but also the light absorption in the thick ARC layer. Although increasing SiO₂ slightly deteriorates the standing wave, the overall contrasts are still acceptable. Thus, the SiO₂ thickness is not a constant parameter in TLR process, which should adapt to the ARC thickness.

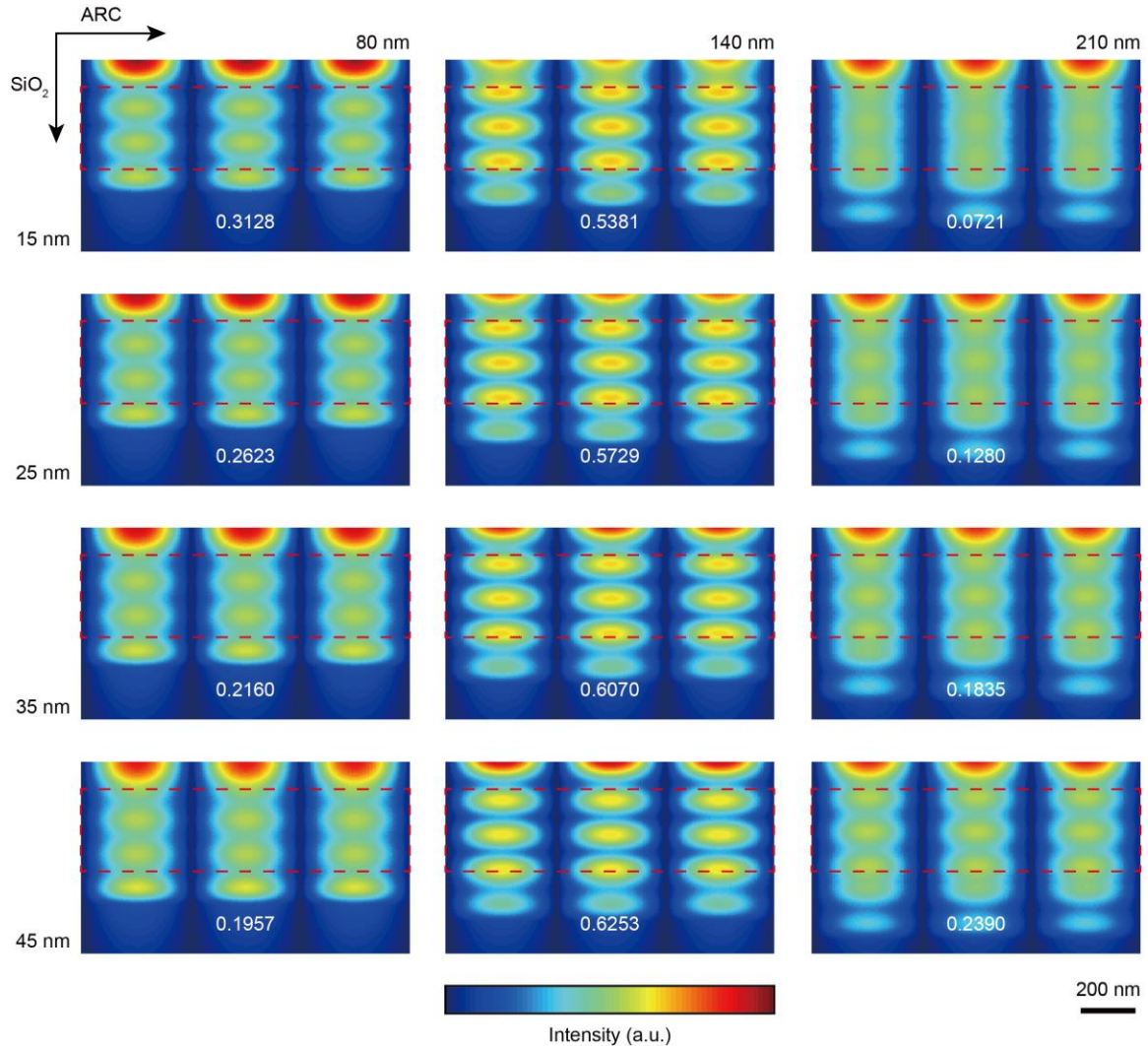


Figure 3-7 FDTD simulation of the electric field distribution in the ARC/SiO₂/photoresist stack. The best result is in the 210-nm ARC group, followed by the 80-nm ARC group, while 80-nm ARC group is the worst. The interference period and photoresist thickness are fixed at 400 nm and 300 nm, while SiO₂ and ARC thicknesses are assigned as 15/25/35/45 nm and 80/140/210 nm, respectively.

3.3 Experimental results

To verify the reliability of the above modeling, 400-nm-period gratings are experimentally exposed on tri-layer substrates with different SiO₂ and ARC thicknesses, which are recorded in SEM images of Figure 3-9. Consistent with the simulation, the 210-nm ARC group has the best morphologies, the 80-nm group comes the second, and the 140 nm is the worst. For the 80 nm ARC stack, the sidewall becomes smoother when increasing the SiO₂ thickness, which also matches the simulation that the contrast can be improved by tuning the SiO₂ thickness.

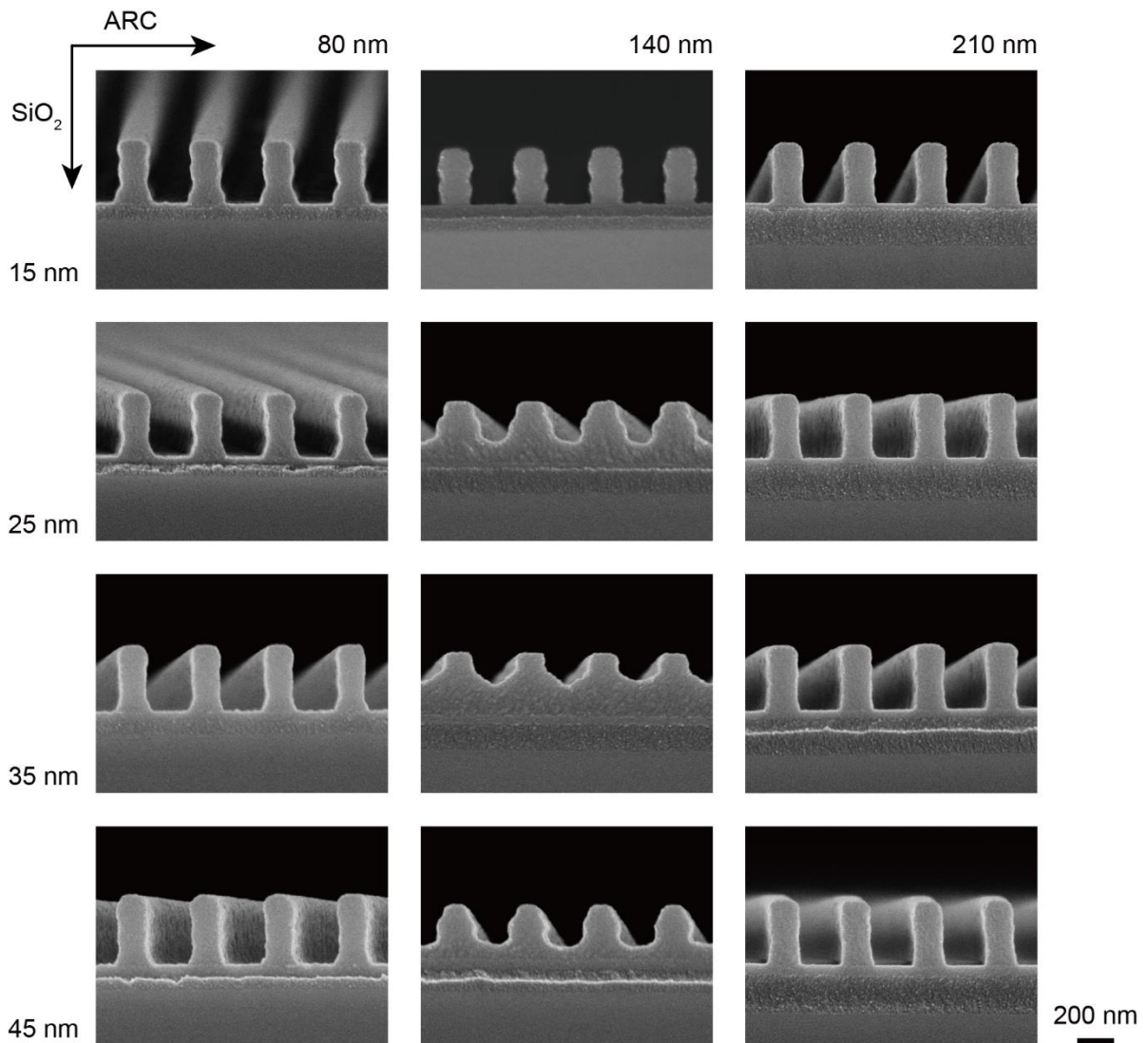


Figure 3-8 SEM images of IL-exposed 400-nm-period gratings using different ARC and SiO_2 thicknesses. Gratings with 80 and 210 nm ARC have vertical and smooth profiles due to the high contrast, while gratings with 140 nm ARC are strongly affected by the standing wave, showing rough profiles.

From the above simulated and experimental results of 400-nm interference period, the 210-nm ARC group has the best pattern quality and widest SiO_2 thickness range. However, thick ARC is not suitable for all situations. For example, when fabricating sub-100-nm nanopatterns, structures may collapse in the ARC open process because etching thick ARC shrinks more lateral dimensions induced the isotropic etching. The thin ARC

post usually cannot support the top SiO₂, resulting in structure collapse (Figure B-2). Thus, a thinner ARC that locates at the first minimum of the reflectivity curve (Figure 3-5) or contrast distribution (Figure 3-7) is recommended when exposing sub-100-nm nanostructures to avoid the collapse.

3.4 High-fidelity pattern transfer and scalability demonstration

3.4.1 High-fidelity pattern transfer using tri-layer resist process

Using the optimized SiO₂ and ARC thicknesses, a Si mold fabrication through TLR process is demonstrated in Figure 3-10, of which each main step is characterized by SEM. Before spin-coating the photoresist, ARC and SiO₂ are coated on Si substrate with 200 nm and 25 nm, respectively. After IL exposure and development, high-quality nanopillars are recorded in the photoresist with smooth profiles. Using the photoresist pattern as the etching mask, we first use ICP to etch into SiO₂. With the hard SiO₂ mask, the ARC can be then over-etched into undercut profiles, which benefits the following lift-off process. The nanopattern can be reversed into the complementary Cr pattern after the deposition and lift-off. Finally, the substrate can be etched into a nanohole array with designed depth.

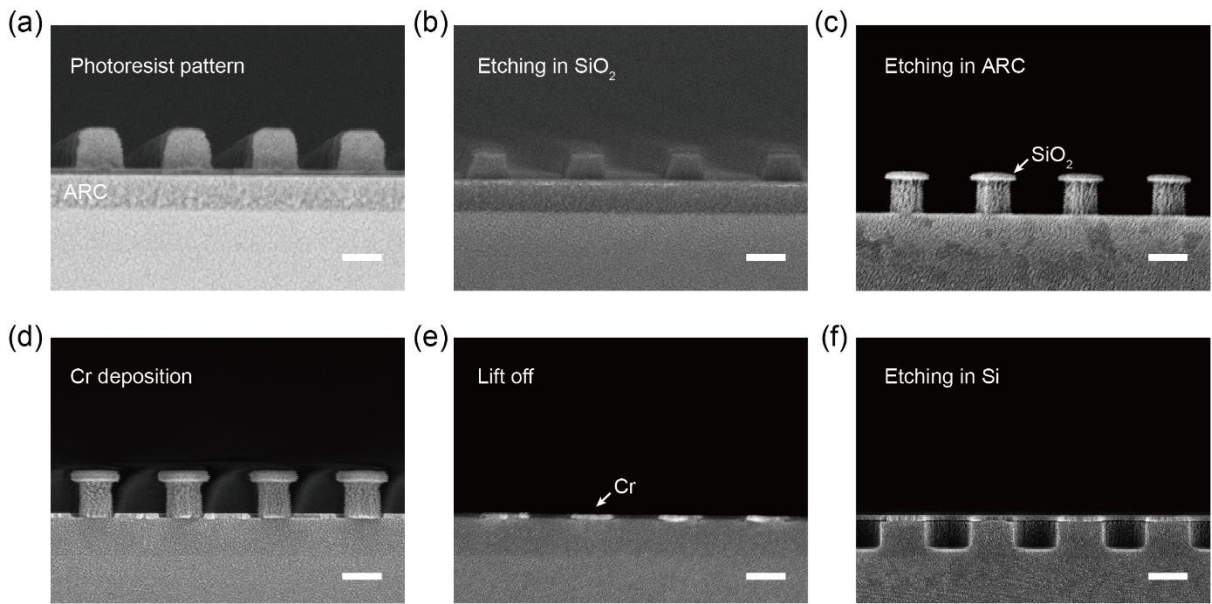


Figure 3-9 SEM images recorded for each step in TLR process. (a) High-quality photoresist nanopillar pattern exposed by IL. (b) SiO₂ interlayer etched using photoresist as the etching mask. (c) ARC layer etched using the SiO₂ as the etching mask, which forms an undercut structure. (d) Cr deposited by e-beam evaporation. (e) Cr pattern left after the lift-off process. (f) High-quality Si nanohole pattern etched using Cr as the etching mask. Scale bars, 200 nm.

The top-viewed morphologies are also recorded by SEM in the initial photoresist and final Si substrate, respectively, to quantitatively characterizing the dimension variation (Figure 3-11a, b). Measured dimensions plotted in Figure 3-11c show that the average diameter changes from 237.8 nm to 228.4 nm. The less than 4% variation demonstrates that TLR process possesses a high fidelity in the pattern transfer process.

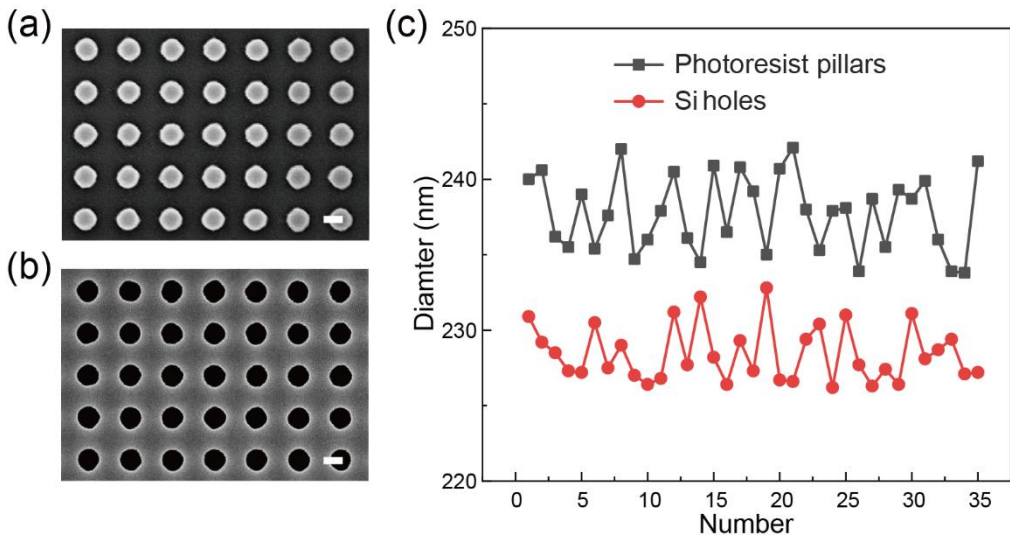


Figure 3-10 The fidelity characterization by SEM measurements. SEM images of (a) photoresist nanopillars and (b) Si nanoholes before and after TLR pattern transfer, respectively. (c) The statistical plot with the circle diameter characterization of nanopatterns in photoresist and Si, showing the size reduction of less than 4%. Scale bars, 200 nm.

3.4.2 Scalability of interference lithography on complex substrates

In addition, the numerical modeling analysis could be extended to complex substrates that have multi-layer structures for exposing high-quality pattern using IL. Recently nanodevices constructed of the metal-insulator-metal (MIM) structure are widely investigated in a variety of the research fields such as the plasmonic sensing⁷⁷⁻⁸⁰. However, considering the difficulties in etching metallic materials and lift-off process, the metallic layer usually cannot be designed and deposited over 100 nm. A simple and straightforward process using high-aspect-ratio photoresist patterns as the mask to directly etch into the underlying MIM structures is demonstrated. However, the optical lithography is challenging on such substrates because the standing wave can be easily produced due to the complicated optical interaction on the multi-layer structures. Thus, the numerical

modeling for the ARC thickness optimization is necessary before performing the IL exposure. For example, using the fused silica coated with 100 nm Au, 100 nm SiO₂, and 100 nm Au as the MIM substrate, the simulation is first employed with different ARC thicknesses to obtain the reflectivity curves, shown in Figure 3-12a and 12c. Then we experimentally expose nanogratings with the ARC layers of 240 and 175 nm, responding to contrast of 0.2703 and 0.0774. SEM images characterized in Figure 3-12b and 12d show the rough and smooth profiles, respectively, which agrees well with the simulation.

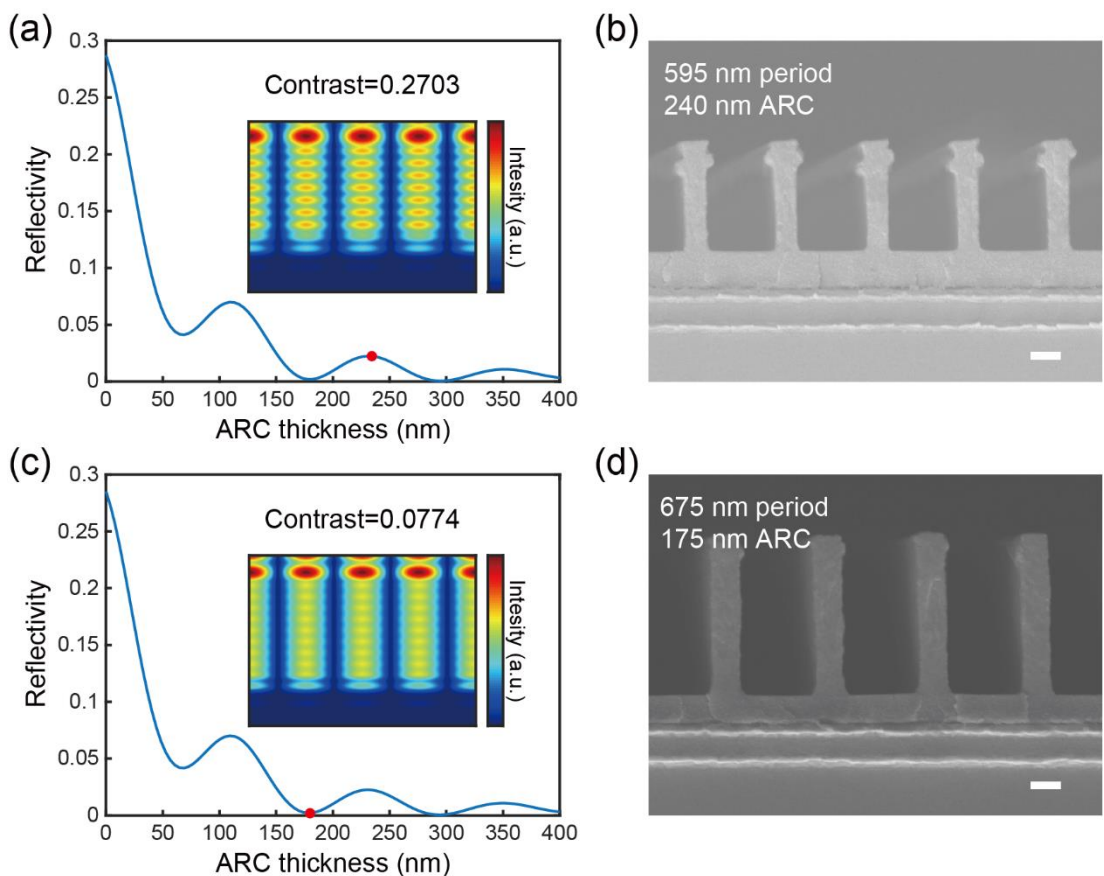


Figure 3-11 Simulated and experimental results of TMM and FDTD analysis applied on complex multi-layer substrates. (a) Simulated and (b) SEM results of IL-exposed nanogratings on 240-nm-thick ARC, which has a high contrast and undesired profiles. (c) Simulated and (d) SEM results of IL-exposed nanogratings on 175-nm-thick ARC, which has a low contrast and high-quality profiles. Scale bars, 200 nm.

With the exposed high-quality and high-aspect-ratio resist pattern, ion beam etching (IBE) is directly employed on the MIM substrate after ARC removal by RIE (Figure B-3). SEM images showed etched high-aspect-ratio MIM nanostructures, indicating that our scalable numerical analysis can be extended to the nanofabrication for versatile applications.

3.5 Summary

With regard to the standing wave phenomenon using IL on complex substrates, a numerical modeling approach is studied in this chapter to optimize process parameters. Using the high-fidelity pattern transfer technique TLR process as an example, a set of numerical analysis strategies is constructed to optimize the ARC and SiO₂ thicknesses according to different exposure targets. With the numerically optimized TLR process, the resist pattern is successfully transferred in Si substrate with only 4% feature size variation. Besides, the scalability of this strategy is also demonstrated on other complex multi-layer substrates for diverse applications.

Chapter 4 High-fidelity and Clean Nanotransfer

Lithography Using Structure-embedded and Electrostatic-adhesive Carrier

In this chapter, we propose a high-fidelity, clean nanotransfer lithography method that can efficiently transfer metallic nanostructures, initially patterned by IL or NIL, onto unconventional substrates. In this technique, a polyvinyl acetate (PVA) film is employed as the transferring carrier and promoting the electrostatic adhesion through triboelectric charging. The water-soluble PVA film embeds the transferred metallic nanostructures and maintains their spacing with a remarkably low variation of less than 1%. When separating the PVA film from the donor substrate, electrostatic charges are generated due to triboelectric charging and facilitate the adhesion to the receiver substrate, resulting in a high large-area transfer yield up to 99.93%. We successfully transferred metallic structures of a variety of materials (Au, Cu, Pd, etc.) with different geometries of sub-50-nm spacing, high aspect ratio (>2), and complex 3D structures. Moreover, the thin and flexible carrier film enables the transfer on highly curved surfaces such as the single-mode optical fiber with a curvature radius of 62.5 μm . With this strategy, we demonstrate the transfer of metallic nanostructures for a compact spectrometer with Cu nanogratings transferred on a convex lens and for surface-enhanced Raman spectroscopy (SERS) characterization on graphene with reliable responsiveness.

4.1 Introduction

Nanoscale metallic structures and their potential applications are currently investigated in many emerging fields such as plasmonics^{54,81,82}, electronics^{83,84} and

biosensors^{85,86}. However, a variety of these applications need to pattern nanostructures on unconventional substrates, such as curved optical components (optical fiber, lens, etc.) and soft biomimetic materials, where traditional nanofabrication strategies such as photolithography, plasma etching, and vacuum deposition are difficult to apply. For example, spin-coating photoresist is challenging on curved surfaces to form a uniform layer of photoresist, and high-vacuum evaporation is not suitable for porous substrates. Thereby, patterning metallic nanostructures with high fidelity and quality on arbitrary surfaces still represents a substantial challenge. Recently, nanotransfer lithography (NTL) has become one of the most adopted methods for patterning on unconventional surfaces due to its process simplicity, high throughput, and cost-effectiveness⁸⁷⁻⁹².

Generally, the transfer carrier plays an essential role in the transfer process due to its close relationship with both the donor and receiver substrates. In most published nanotransfer research, functional material was first deposited on the nanostructured carrier by evaporation or sputtering and then transfer-printed onto the specific receivers⁹³. However, this approach normally introduces undesirable edge roughness on the transferred pattern because the material is deposited on the surface of nanostructures with no confinement. It also limits the transferred pattern geometries to planar structure, but thick and three-dimensional (3D) structures are difficult to transfer. Besides, chemical adhesive promoters are also needed to improve the transfer yield, which can generate a chemical bonding construction via surface treatments to increase the adhesion^{94,95}. However, most chemical adhesive media is environmentally harmful, and the residues may negatively affect the performance of fabricated devices. Although the adhesive-layer-free nanotransfer is also feasible, the receivers are generally specified to be textiles⁹⁶, thermoplastic polymers⁹⁷, or sticky scotch tape⁹⁸. To date, it remains a challenge to develop an NTL

process that simultaneously satisfies three conditions of (1) high fidelity and high transfer yield, (2) no additional residues, and (3) arbitrary receivers.

Herein, we develop a high-fidelity, clean structure-embedded and electrostatic-adhesive NTL (SENTL) process to address the above challenges. Used as the transfer carrier, the water-soluble polyvinyl acetate (PVA) film embeds the transferred structures and maintains their original order to ensure a high fidelity with less than 1% spacing variation. The PVA transfer carrier also provides triboelectric charges generated from the peeling off process, facilitating the adhesion to the receiver substrate that leads to a high transfer yield of 99.93%. The encapsulating carrier is not only suitable for planar structures of different materials (Au, Cu, Pd, etc.) but also enables the transfer of high-aspect-ratio (>2) gratings with 600-nm thickness and 3D structures. Moreover, the electrostatic-adhesive approach leaves no residues after dissolving the PVA carrier. Besides, the flexible carrier film enables full contact with arbitrary receivers, including rigid, soft, planar, and curved surfaces. As one demonstration, a large-area nanoscale pattern is successfully transferred onto a single-mode optical fiber with a small curvature radius of 62.5 μm . We also demonstrate nanogratings transferred onto a convex lens as a light-dispersive element for a compact spectrometer and gold nanodisks transferred on graphene for surface-enhanced Raman spectroscopy (SERS) analysis.

4.2 Fabrication procedure and mechanisms

4.2.1 Fabrication process of the structure-embedded and electrostatic-adhesive nanotransfer lithography

Using electroplated metallic nanostructures as an example, the process flow of SENTL is schematically illustrated in Figure 4-1. Firstly, a nanoscale structure is patterned

in the resist on ITO glass by nanoimprint or interference lithography and electroplating on the exposed ITO surface grows metallic nanostructures^{99,100}. Then, after removing the resist, PVA aqueous solution is spin-casted on the patterned substrate and cured to form a layer of PVA film that encapsulates the nanostructures. Next, the PVA film with the nanostructures embedded can be easily peeled off from the ITO substrate while effectively maintaining the order of the nanostructures. During this process, triboelectric charges are also induced by the detachment of the PVA film from ITO surface. Then, the PVA film is attached to the receiver substrate and the induced charges contribute to electrostatically enhanced binding between the film and the receiver surface, resulting in a high transfer yield. Finally, after dissolving PVA in water, the metallic nanostructures are firmly transferred onto the receiver.

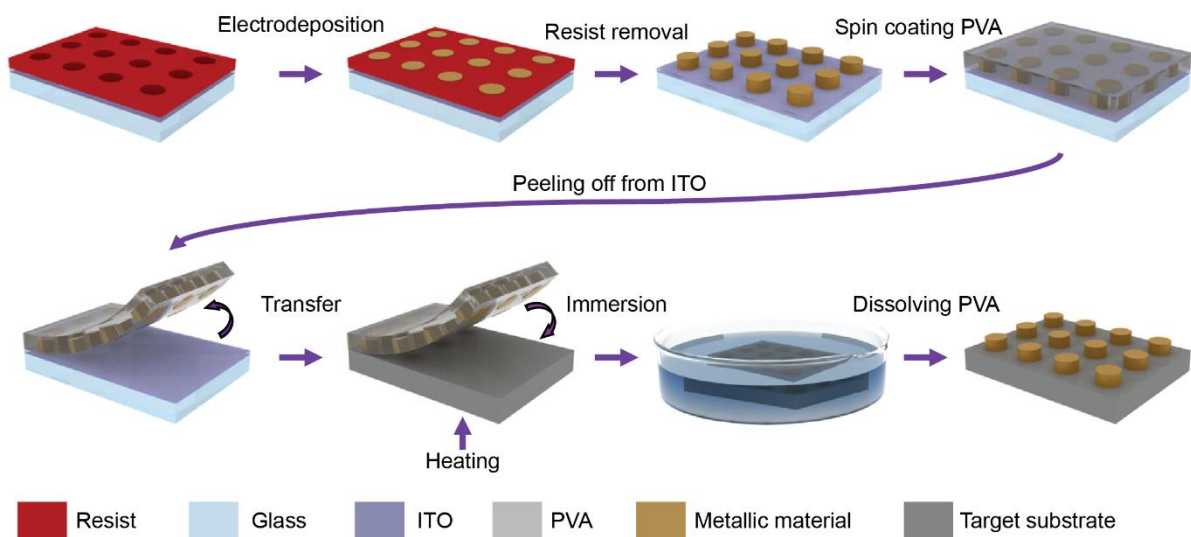


Figure 4-1 Process flow of SENTL applied on electroplated metallic nanostructures.

SEM was implemented to characterize the pattern morphologies at different fabrication steps. Figure 4-2a and 4-2b show the imprinted nanoholes in the resist and electroplated Cu nanodisks on ITO substrate, respectively, featuring the complementary morphologies due to the resist confinement. Figure 4-2c shows the separated PVA film

with Cu nanodisks embedded. The film has a 15- μm thickness as observed in Figure C-1. And Figure 4-2d shows the transferred Cu nanodisks on a glass substrate after dissolving PVA. The inset photographs in Figure 4-2c and 4-2d display the complete pattern with light diffraction.

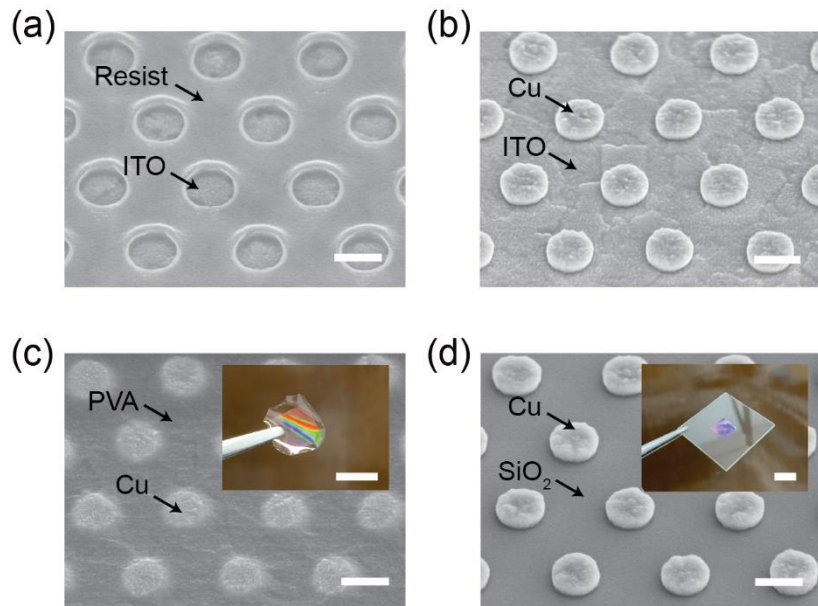


Figure 4-2 SEM images recorded for key steps in SENTL process. (a) Imprinted nanoholes in resist on ITO. (b) Electrodeposited Cu nanodisks on ITO. (c) Cu nanodisks-embedded PVA film. (d) Transferred Cu nanodisks on a glass substrate. Scale bars, 300 nm (a-d), 1 cm (insets in c, d).

4.2.2 High-fidelity order-maintaining by polymeric embedding and high transfer yield owing to electrostatically enhanced adhesion.

In SENTL process, the PVA carrier plays a crucial role in maintaining the nanostructure order and providing a reliable adhesion to the receiver substrate (Figure 4-3). The cured PVA exhibits moderate elasticity under small stretching that happens during peeling off and sample handling, which can help to maintain the nanostructure dimensions

and the horizontal spacing between neighbouring nanostructures in the short range to achieve high transfer fidelity. Meanwhile, its flexibility can allow necessary deformation to conform non-planar or irregular receiver surfaces.

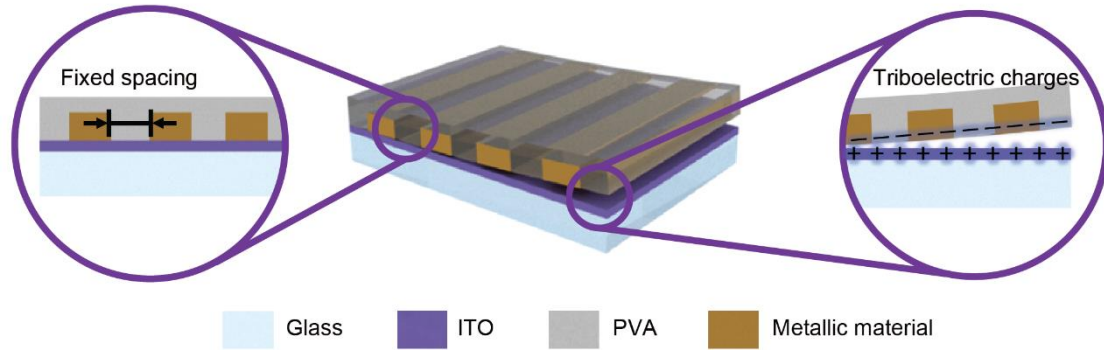


Figure 4-3 Schematic illustration of the high-fidelity lateral dimension maintaining and high transfer yield due to triboelectric electrostatic adhesion.

When the aqueous PVA solution is spin-casted on pre-fabricated nanostructures on the donor substrate, it flows and fills the gap among nanostructures. Then the cured PVA encapsulates nanostructures into a solid film, maintaining the order. In the subsequent peeling off, transferring and attaching steps, the solid PVA keeps the local spacing well maintained by elastically responding to temporary mechanical stress. We performed SENTL process to transfer 600-nm-period Cu gratings from the ITO donor to the Si receiver (Figure 4-4a and 4-4b) and quantitatively characterized the spacing variation before and after the transfer using SEM. A box chart plotted in Figure 4-4c shows that the average line spacing between gratings changes from 243.6 nm to 245.9 nm. The spacing change is less than 1%, indicating SENTL possesses a high fidelity. And the 3σ deviation of line edge roughness (3σ -LER) also exhibits a small change of less than 1 nm from 6.3 nm to 7.2 nm.

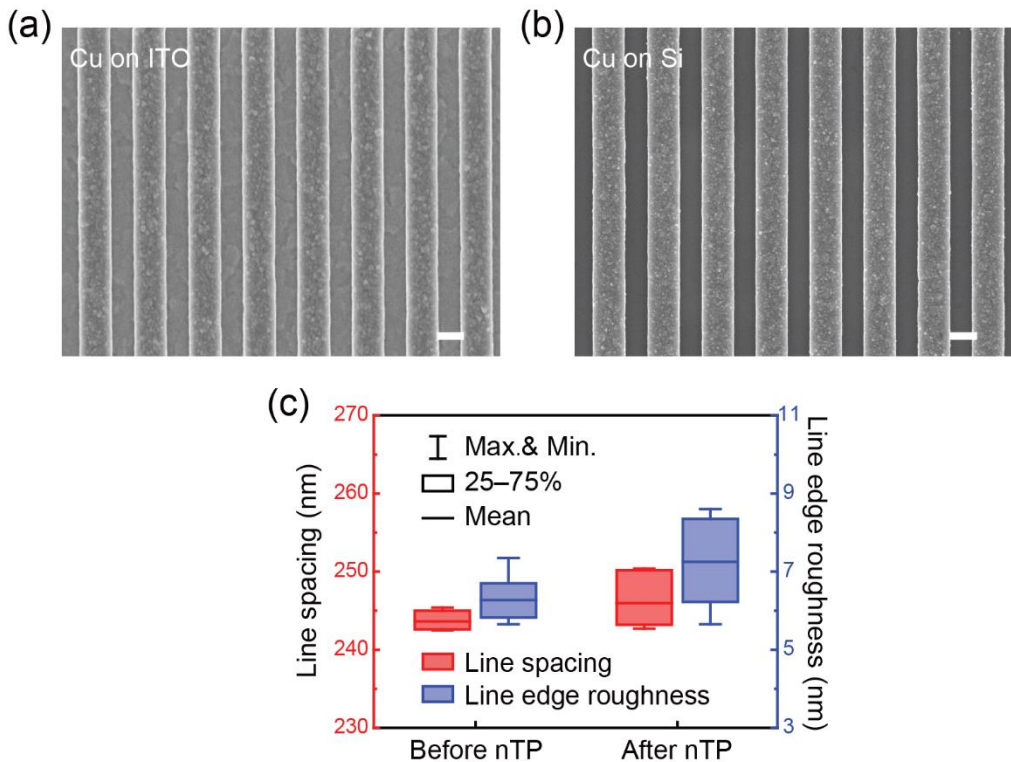


Figure 4-4 High fidelity characterization of SENTL. (a) and (b), SEM images of Cu nanogratings before and after SENTL transfer, respectively. (c) The statistical box plot with the mean, maximum, minimum, and 25-75% range of the distribution of the line spacing and line edge roughness of Cu nanogratings before and after transfer. Scale bars, 300 nm.

On the other hand, triboelectric charges induced on the surface of the PVA carrier during its separation from the donor ITO substrate contribute to significantly improve the transfer reliability with enhanced electrostatic adhesive force. According to the electron transfer mechanism and triboelectric series¹⁰¹⁻¹⁰³, electrons will transfer from the ITO to the PVA carrier at the interface when the two are in contact as the ITO is prone to give up electrons and the PVA prefers to grab them. When the PVA film is peeled off from the ITO substrate, the pristine PVA surface surrounding the transferred nanostructure is exposed and becomes negatively charged with the total charge amount proportional to the exposed PVA surface area^{104,105}.

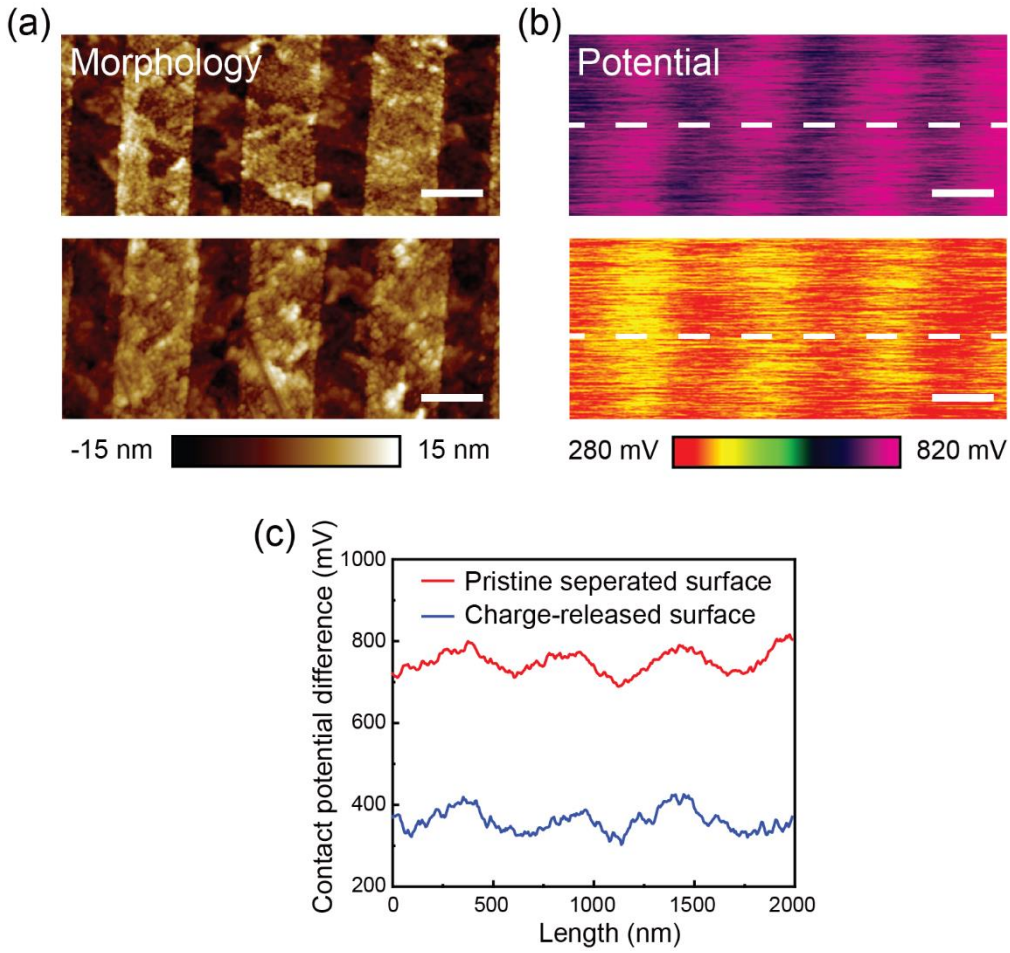


Figure 4-5 Triboelectric charges characterization in SENTL. (a) and (b), the KPFM surface topography and surface potential mapping of the PVA carrier film with embedded Au nanogratings immediately after separation and after charge releasing, respectively. (c) The KPFM surface potential difference variation before and after charge releasing. Scale bars, 300 nm.

To confirm the existence of the induced triboelectric charges, surface potential variation was quantitatively characterized using Kelvin probe force microscopy (KPFM). We measured the morphologies and contact potential differences on the PVA carrier film immediately after the separation and after releasing the surface charges, which are shown in Figure 4-5a and 4-5b, respectively. Although both exhibit similar surface morphology, on the pristine PVA surface, the surface potential was approximately up to 750 mV, while

that of the charge-released surface was about 300 mV, indicating more negative charges existing on the pristine PVA surface (Figure 4-5c). The charges on the PVA carrier enable the electrostatic adhesion enhancement when attached to the receiver substrate. As a result, centimeter-scale nanopatterns can be completely transferred by SENTL with a transfer yield up to 99.93%, as examined on 5 different positions of 1-cm²-area transferred nanodisk pattern (Figure 4-6).

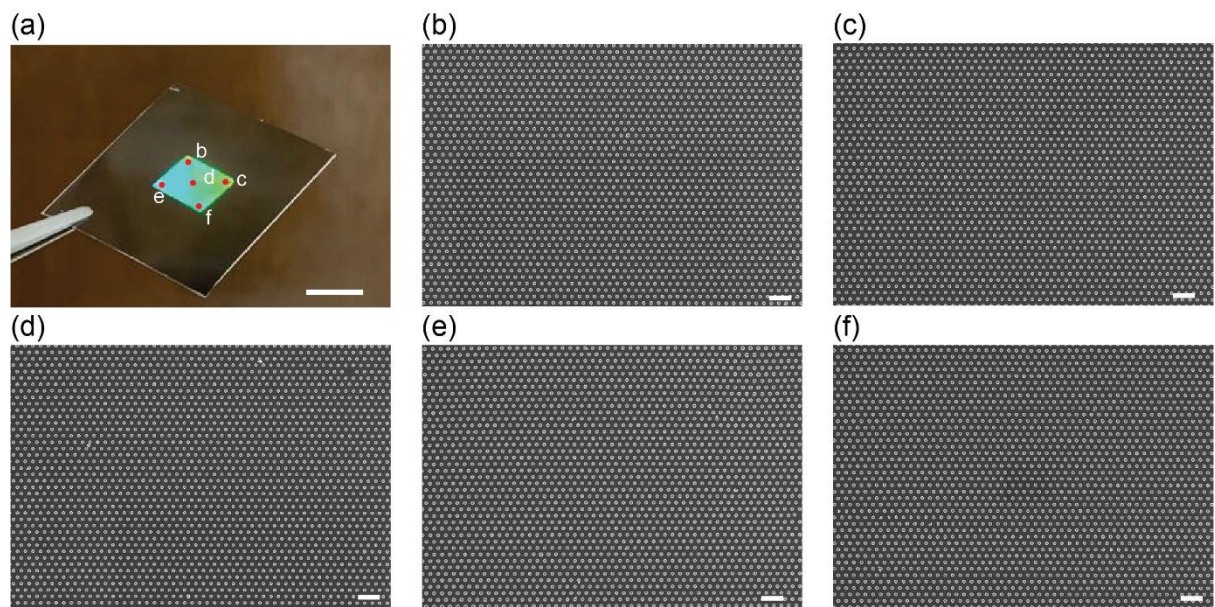


Figure 4-6 High transfer yield of SENTL. (a) Photograph of the 1-cm²-area transferred nanodisk pattern. (b-f) SEM images obtained from five different points on the transferred pattern. Scale bars, 2 μm in (b-f) and 1 cm in (a).

4.3 Experimental results

4.3.1 Structural and material versatility in SENTL process

SENTL enables the transfer of nanostructures with various geometries and materials. Figure 4-7a shows the SEM image of transferred Au nanogratings on Si substrate with down to 40-nm spacing, indicating the high resolution that SENTL can achieve. SENTL

also exhibits high fidelity in transferring discrete 2D nanopattern. For example, an array of Cu nanodisks with hexagonal order was transferred onto a glass substrate, maintaining a pristine order and a uniform disk diameter of 2.8 nm standard deviation (Figure 4-7b). Figure 4-7c presents a transferred continuous Au nanohole array for structural color and sensing application.

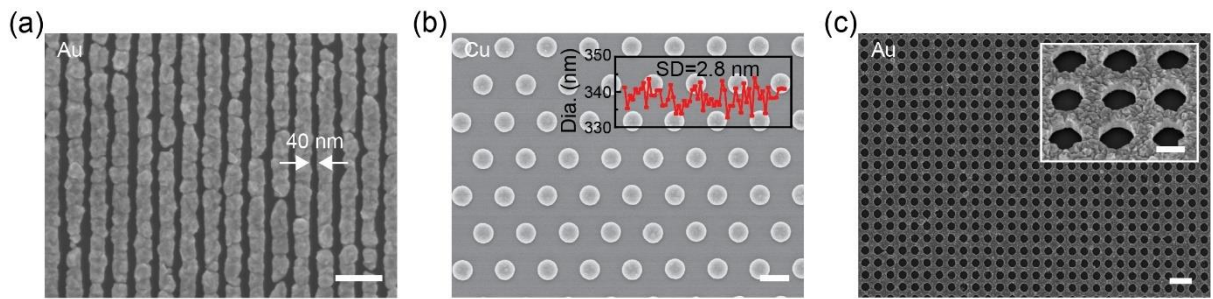


Figure 4-7 SEM images of various 1D/2D nanostructures transferred by SENTL. (a) High-resolution Au nanogratings with 40-nm spacing. (b) 700-nm-period Cu nanodisks of uniform diameters with a standard deviation of 2.8 nm. (c) 550-nm-period Au nanohole array. Scale bars, 300 nm (a, inset in c), 500 nm (b), and 1000 nm (c).

Encapsulating the nanostructure into the transfer carrier, SENTL opens further opportunities to transfer challenging complex patterns such as high-aspect-ratio and complex 3D nanostructures. Figure 4-8a shows the cross-sectional SEM image of transferred 300-nm-width and 600-nm-height rectangular nanogratings on Si, featuring an aspect ratio of 2. Compared to most reported methods for transferring evaporated material with the nanostructured carrier, SENTL is advantageous in transferring more than 100-nm-thick nanostructures on subwavelength scale. In addition, using the transferred thick metallic pattern as etching mask instead of conventional metal evaporation and lift-off processes, the underlying substrates can be directly etched with a high aspect ratio. For example, using the transferred pattern as the etching mask, silicon substrate can be etched up to 800 and 1500 nm, respectively, as demonstrated in Figure C-2. Moreover, The

SENTL also supports the transfer of 3D nanostructures like Z-shaped gratings (Figure 4-8b) as the PVA aqueous solution could fill into the complex gap and support the hollow structure after cure (Figure C-3). Besides, the multi-step layer-by-layer transfer is also allowed in SENTL for fabricating stacked 3D nanostructures. As demonstrated in Figure 4-8c, stacked-nanomesh can be constructed by orthogonally transferring the nanogratings twice, which have been reported in applications such as gas sensing due to its high specific area¹⁰⁶. Using the stacked-nanomesh as an etching mask, the square nanohole array pattern can also be transferred to the underlying silicon substrate, as shown in Figure C-4.

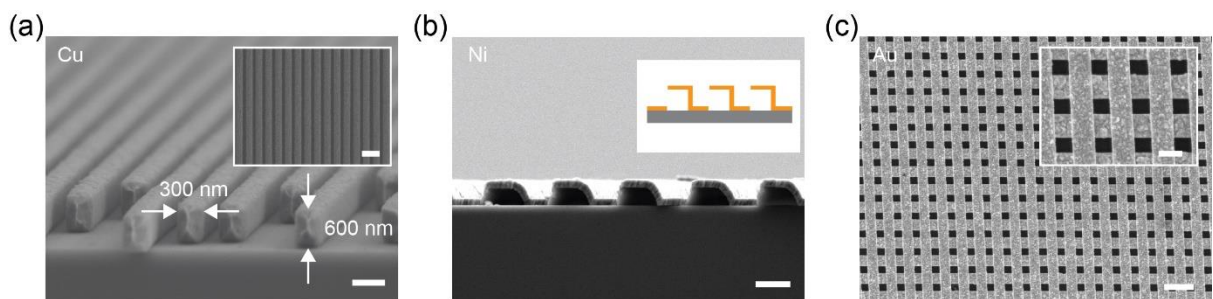


Figure 4-8 SEM images of high-aspect-ratio and 3D nanostructures transferred by SENTL.

(a) High-aspect-ratio Cu nanogratings with 300-nm width and 600-nm height. (b) Quasi-3D Z-shaped Ni nanostructures. (c) Stacked-mesh nanostructure fabricated by double SENTL transfer. Scale bars, 300 nm (inset in c), 500 nm (a, b), and 1000 nm (c, inset in a).

Our SENTL process is compatible with nanostructures of a wide range of materials. When applied on electrodeposited nanostructures, the SENTL process is demonstrated on nanostructures made of Au (Figure 4-7a,c and 4-9c), Cu (Figure 4-7b and 4-8a), Ni (Figure 4-8b), and other metals that can be electrodeposited, such as Pd and Co (Figure 4-9a,b), respectively. Energy-dispersive X-ray (EDX) spectroscopy results obtained from the transferred metallic structures show that nearly no polymer residue (C, H, O) remains (Figure 4-9d, C-5) since the adhesive promoter in SENTL is the triboelectric charges and the transfer media is the water-soluble PVA, which contribute to the clean transfer.

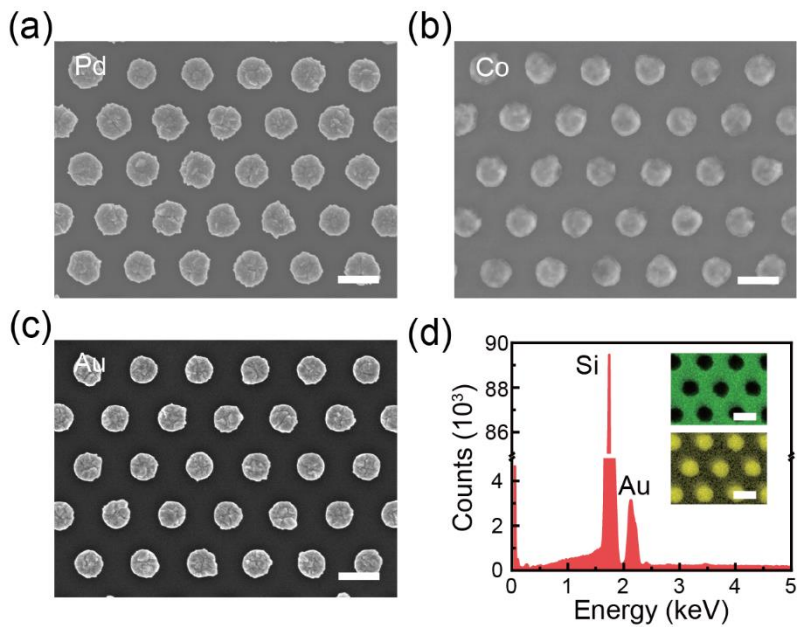


Figure 4-9 SEM images of various nanostructures transferred by SENTL. (a, b) 700-nm-period Pd and Co nanodisks. (c) 700-nm-period Au nanodisks and (d) corresponding EDX spectrum indicating a residue-free transfer. Scale bars, 500 nm.

4.3.2 Receiver substrate compatibility in SENTL process

SENTL can be applied on various receiver substrates, rigid or flexible, planar or curved, adhesive or non-adhesive, owing to its flexible PVA carrier and electrostatic adhesion. Besides the rigid Si and glass substrates used in previous demonstrations, we have also successfully transferred Cu nanodisks onto the polydimethylsiloxane (PDMS) soft pad and polyimide (PI) thin film (Figure 4-10a and 10b), which have potential applications in flexible wearable electronics¹⁰⁷⁻¹⁰⁹. Besides, SENTL also supports the transfer on polytetrafluoroethylene (PTFE) substrates with ultralow friction coefficient, as shown in Figure 4-10c, where the transferred nanodisks were firmly adhered to the rugged low-surface-energy surface and still maintained well-ordered arrangement. In addition, SENTL is also capable of fabricating hierarchical structures for security identification¹¹⁰.

and super-hydrophobic surfaces. As a demonstration, Figure 4-10d shows the Cu nanodisks transferred onto a 10- μm -diameter and 2- μm -height micropost array.

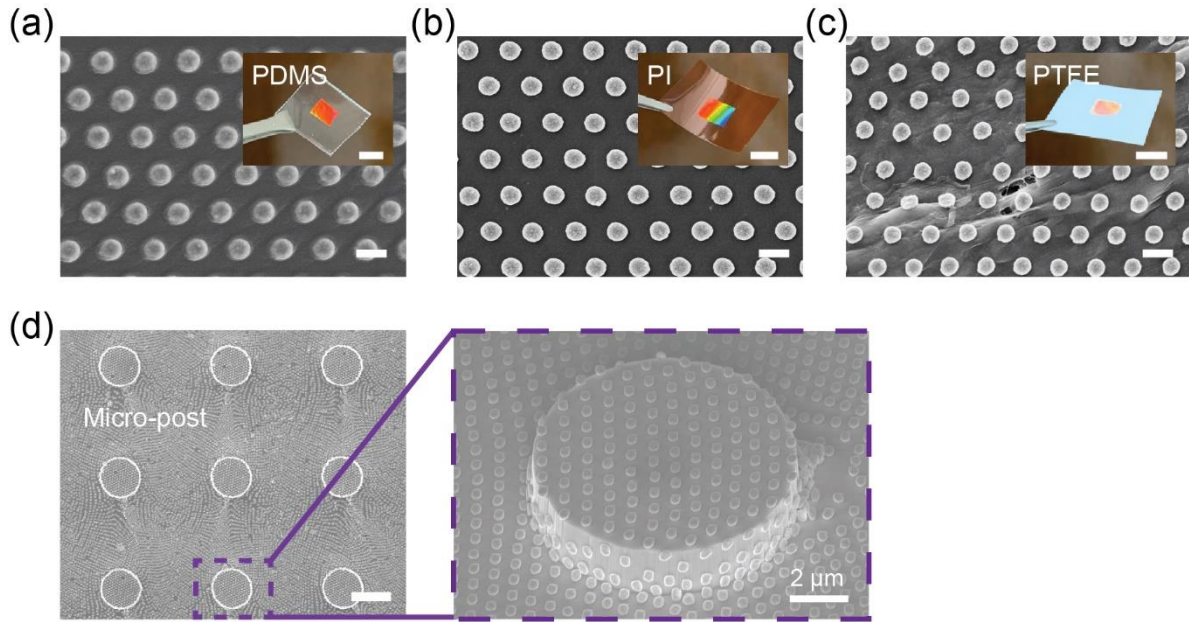


Figure 4-10 Experimental results of SENTL-transferred nanostructures on flexible and patterned substrates. Including (a) PDMS pad, (b) PI film, (c) PTFE film, (d) 10- μm diameter and 2- μm height Si micropost array. Scale bars, 500 nm (a-c), 10 μm (d), and 1 cm (insets in a-c).

Moreover, SENTL also offers opportunities to transfer nanostructures on highly curved substrates such as a 2-cm-diameter glass ball (Figure 4-11a) and a 1-mm-diameter plastic optical fiber (Figure 4-11b). And the Cu and Au nanodisk arrays were transferred by SENTL on both the inner and outer surfaces of a glass vial (Figure 4-11c), which may find applications in directly detecting low-concentration molecules dispersed in a solution¹¹¹. Particularly, we demonstrated SENTL for transferring 700-nm-period and 350-nm-diameter Cu nanodisk array on quartz optical fiber, a highly miniaturized optoelectronic platform¹¹²⁻¹¹⁵, where conventional nanofabrication techniques face great

challenges. In Figure 4-11d, a 125- μ m-diameter single mode (SM) optical fiber is wrapped with transferred nanodisks with high fidelity and high transfer yield.

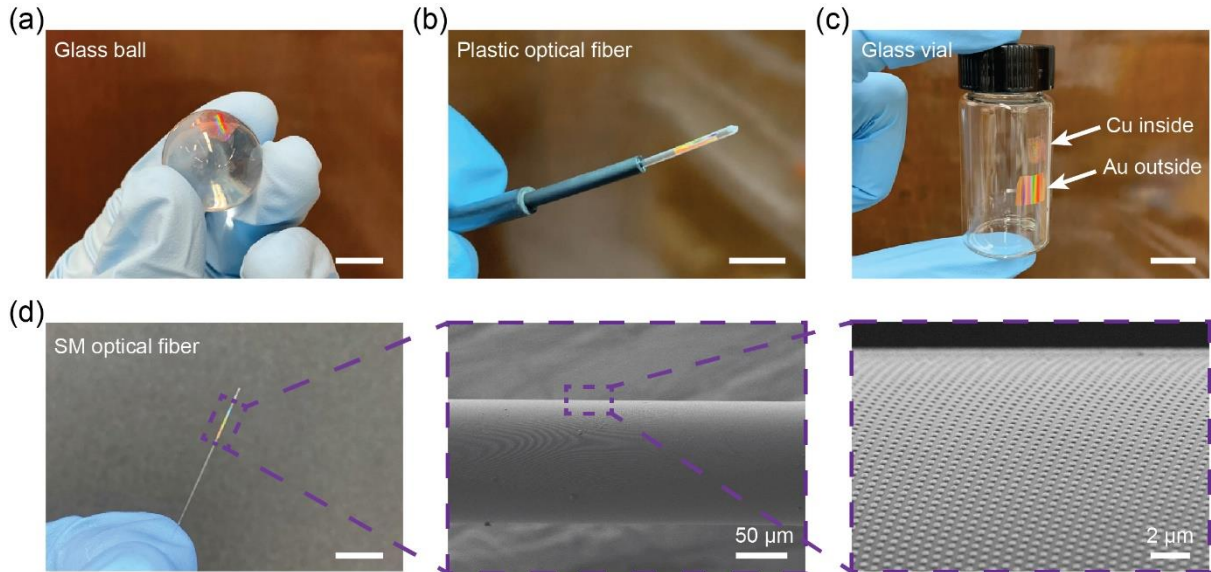


Figure 4-11 SEM images and photographs of SENTL-transferred nanostructures on curved substrates. Including (a) glass ball, (b) plastic optical fiber, (c) inner and outer wall of a glass vial, and (d) 125- μ m diameter single-mode optical fiber. Scale bars, 1 cm.

4.4 Demonstrations of compact spectrometer with convex nanogratings and SERS analysis on graphene

SENTL enables the fabrication of unconventional devices that feature functional nanostructures on non-planar, flexible, or irregular substrates. We first demonstrate a compact spectrometer that is based on a convex lens with the surface patterned with diffractive gratings, so that the wavelength dispersion and imaging can be performed using a single component, as shown in Figure 4-12a. SENTL was used to transfer 600-nm-period Cu nanogratings on the convex lens. The light from a white light-emitting diode is dispersed by the grating and focused by the lens, forming a rainbow-like stripe image on the screen. By recording this image using a monochromatic complementary metal-oxide-

semiconductor (CMOS) detector (Figure 4-12b) and mapping the spatial position to corresponding wavelength (Figure 4-12c), we can reconstruct a spectrum of the incident light beam (Figure 4-12d). The relation between the spatial position and the corresponding wavelength is determined through calibration using narrow-band light beams of known wavelengths¹¹⁶ (e.g., 470, 532 and 650 nm, Figure C-6). The reconstructed spectrum in Figure 4-12d exhibits good consistency with the spectrum obtained using a commercial spectrometer (Figure 4-12e).

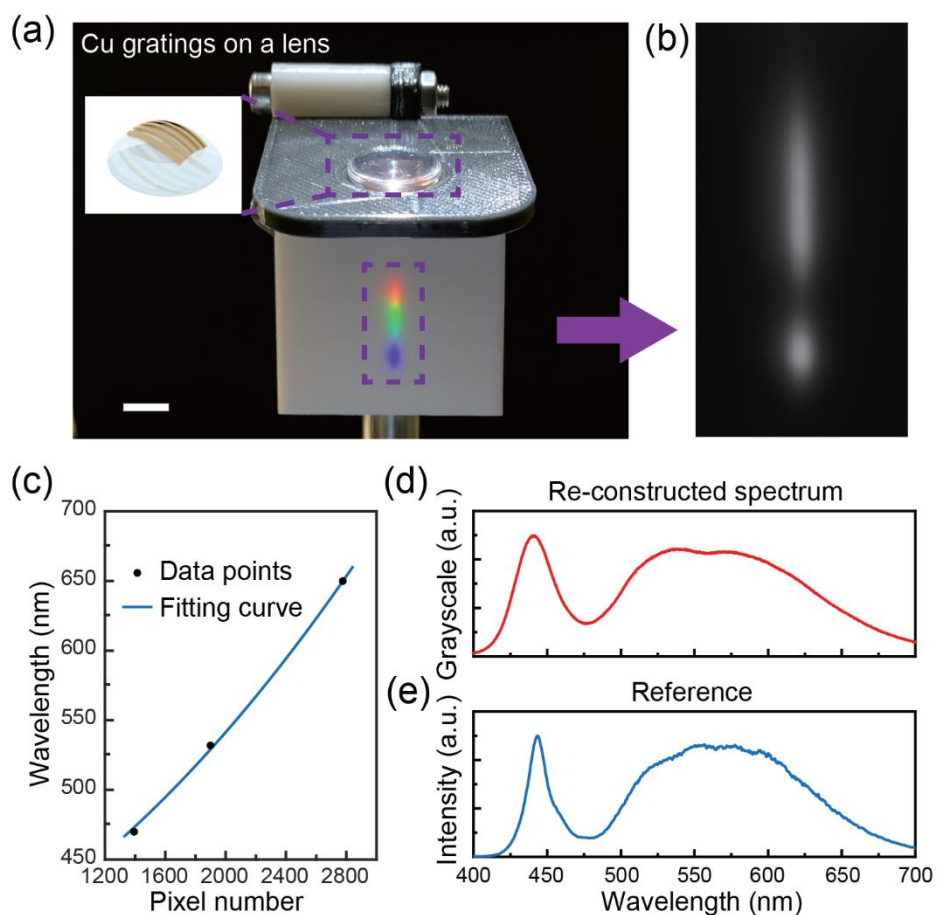


Figure 4-12 Compact spectrometer enabled by SENTL. (a) Photograph of rainbow-like stripe image formed by dispersing and focusing the light from a white LED using the transferred nanogratings on a convex lens. (b) Greyscale image of the stripe captured by a monochromatic CMOS detector. (c) Plot that maps the pixel position to the calibrated

wavelength. (d) Reconstructed spectrum obtained from the greyscale image. (e) Reference spectrum measured by a commercial spectrometer. Scale bar, 1 cm.

We also transfer Au nanodisks, which can greatly enhance Raman spectroscopic signals through local electrical field concentration, onto atomically thin materials for SERS characterization (Figure 4-13a). Figure 4-13b shows Au nanodisks transferred on monolayer graphene supported by a SiO₂-coated substrate. As demonstrated in Figure 4-13c, the transferred Au nanodisks significantly enhanced the weak Raman signature on bared graphene, as well as quenched the fluorescence of SiO₂ substrate.

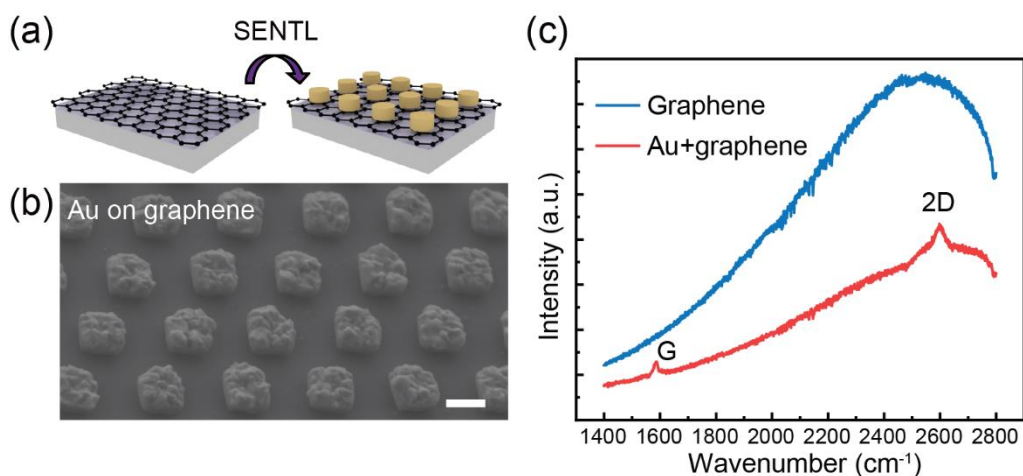


Figure 4-13 SERS analysis on graphene enabled by SENTL. (a) Schematic diagram and (b) SEM image of transferred Au nanodisks on monolayer graphene. (c) Raman spectra showing an enhancement of Raman signatures of Au-covered graphene over that measured from bare graphene under 785-nm excitation. Scale bar, 300 nm.

4.5 Summary

In summary, we reported a facile and efficient nanotransfer lithography approach to achieve clean, high-fidelity and high-transfer-yield nanopatterning on arbitrary substrates with no polymeric residues. As the water-soluble transfer carrier, the spin-casted PVA film

effectively embeds the pre-fabricated nanostructures and provides electrostatic adhesion for transfer-printing. With the SENTL strategy, we achieved a high fidelity of less than 1% transfer spacing variation and a high transfer yield up to 99.93%. Nanostructures of various geometries and materials were reliably transferred onto diverse substrates that are rigid, soft, planar, and curved, even including a single-mode optical fiber. SENTL enables the fabrication of unconventional devices and the exploration of new applications. we demonstrated a compact spectrometer application using a convex lens integrated with diffractive nanogratings and the SERS analysis for 2D materials through SENTL. It is foreseeable that SENTL may provide exciting implications for electronic, plasmonic, and other devices that can benefit from its reliable responsiveness and broad compatibility.

Chapter 5 Spatial Modulation of Feature Size Using Interference Lithography and Grayscale-patterned Secondary Exposure

In this chapter, we advance a novel nanolithography towards wafer-scale, arbitrary modulation of feature size distribution by introducing a lithographic portfolio combining interference lithography and grayscale-patterned secondary exposure (IL-GPSE). Employed after the high-throughput interference lithography, a secondary exposure with patterned intensity distribution spatially modulates the dimensions of photoresist nanostructures. Based on this approach, we successfully fabricated 4-inch wafer-scale nanogratings with uniform linewidths of less than 5% variation, using grayscale-patterned secondary exposure to compensate for the linewidth difference caused by the Gaussian distribution of the laser beams in the interference lithography. Besides, we also demonstrated a wafer-scale structural painting by spatially modulating the filling ratio to achieve gradient grayscale color using secondary exposure.

5.1 Introduction

The precise control of feature size exhibits great importance in fabricating nanodevices for optoelectronics^{55,117}, plasmonics^{118,119}, metasurface^{45,120} and biosciences^{54,121}, just to name a few. Some applications highly require uniform critical dimensions of nanostructures such as nanogratings applied in astronomy^{56,122}, precision measurements¹²³, or laser applications¹²⁴, of which non-uniform feature sizes are regarded as defects or aberrations, deteriorating the device performance. But some devices heavily rely on nanostructures with spatially varying feature sizes, such as structural color paintings^{125,126}, metalenses¹²⁷⁻¹²⁹ and diffractive waveguides^{130,131}. For example, functional

nanostructures can directly generate structural color by separating light via scattering and diffraction, while the color is mainly dependent on the dimensions and material¹³²⁻¹³⁴. Moreover, spatially arranging the dimensions and orientations of nanostructures enables the manipulation on light propagation via phase control^{135,136}, which has been widely adopted in the emerging metalenses.

To date, the precise manipulation of feature size for nanopatterning on large area is still challenging. Generally, the mainstream approaches for accurate nanopatterning are electron beam lithography (EBL)^{49,137} and focused ion beam (FIB) milling^{138,139}. However, both are serial pixel-by-pixel writing processes, placing a limitation on the patterning area and suffering from low writing efficiency. Although high-throughput nanofabrication techniques such as interference lithography (IL)^{28,140} and nanoimprint lithography (NIL)^{68,69} are capable of large-area patterning, the former is mainly for fabricating periodic structures and the latter heavily relies on the master imprint mold. Additionally, the Gaussian-distributed beam profile in the IL has been utilized to fabricate spatially varying nanostructures with a circular gradient profile and demonstrate their applications in wettability manipulation and biosensing^{75,141}. However, because the circular gradient profile is due to the Gaussian-distribution of the beam intensity, it is still impossible to achieve arbitrary modulation profile of the nanostructure feature sizes. Therefore, devising a nanopatterning approach that simultaneously satisfies (1) high-throughput and large-area patterning and (2) precisely and spatially modulating feature size, remains a challenge.

5.2 The dimension modulation using secondary exposure

5.2.1 Mechanism of the dimension modulation using secondary exposure

The feature size modulation using IL-GPSE was achieved by a combination of two exposure processes, a high-contrast IL for fabricating large-area periodic nanostructures and a secondary exposure for locally tailoring structural dimensions, as illustrated in Figure 5-1. Using positive photoresist as the example, a typical two-beam IL is first implemented to form periodic latent exposed regions with sinusoidal dose profile^{29,142}. The positive photoresist that receives exposure dose above the clearing threshold would be “washed out” during the development while that below the threshold remains^{143,144}. The linewidth of the developed gratings mainly depends on the area proportion exposed below the threshold^{145,146}. In the IL-GPSE fabrication, a secondary exposure will follow the IL exposure and provide additional dose that superimposes on the IL sinusoidal dose profile to increase the effective dose applied on the photoresist, therefore increasing the portion of photoresist that receives above-threshold dose and leaving less photoresist after development. Thus, a linewidth modulation can be achieved by superimposing the IL exposure dose with a patterned secondary exposure dose.

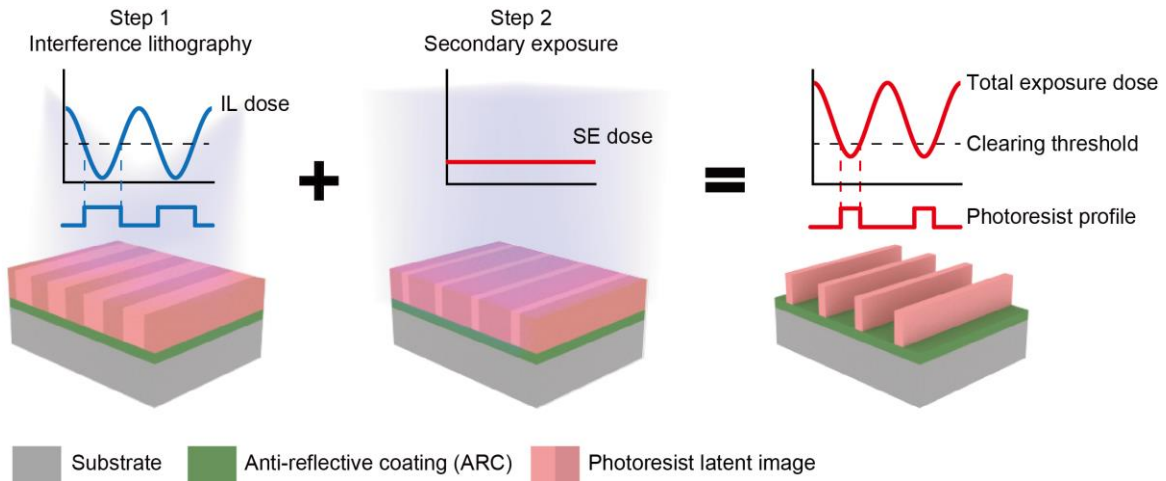


Figure 5-1 The schematic diagram of the IL-GPSE process. Step 1, a two-beam IL is performed on the photoresist to form periodic latent exposed regions with sinusoidal dose profile. Step 2, a secondary exposure follows the IL exposure and increases the effective dose applied on the photoresist which increases the portion of photoresist that receives above-threshold dose, and then leaves less photoresist after development.

Generally, the tunability of IL-GPSE method depends on two important factors, the photoresist contrast and the distribution of the exposure dose. In this part, we construct a numerical model to verify the influence of these factors.

5.2.2 Photoresist characteristics

The photoresist contrast relates to not only the resist's material properties but also baking and development conditions and can be experimentally characterized using the photoresist characteristic curve¹⁴⁷. Figure 5-2a reveals the relation between the normalized photoresist remaining thickness and the exposure dose. The raw data was recorded by exposing 800-nm-thick photoresist (AZ MiR 701, MicroChemicals, GmbH) on ARC/Si substrates with different exposure doses and then measuring the corresponding residual thicknesses after development. The remaining photoresist thickness, T , was then

normalized to the initial unexposed thickness and plotted as a fitting function of the dose, D , to fit the characteristic curve¹⁴⁸:

$$T(D) = \frac{1}{1+e^{\gamma(D-D_c)}} \quad (5.1)$$

where D_c is the clearing dose and γ is the photoresist contrast, extracted to be 40.77 and 0.2474. As a convenience, D_c and γ are regarded as basic units of parameters in simulations. The slope of the transition region in the curve largely determines the sidewall angle of the gratings. When assigning different photoresist contrast characteristics in the model to simulate the morphological variation, the sidewall angle changes with the photoresist contrast and it is roughly maintained during the linewidth tailoring by secondary exposure (Figure 5-2b-d).

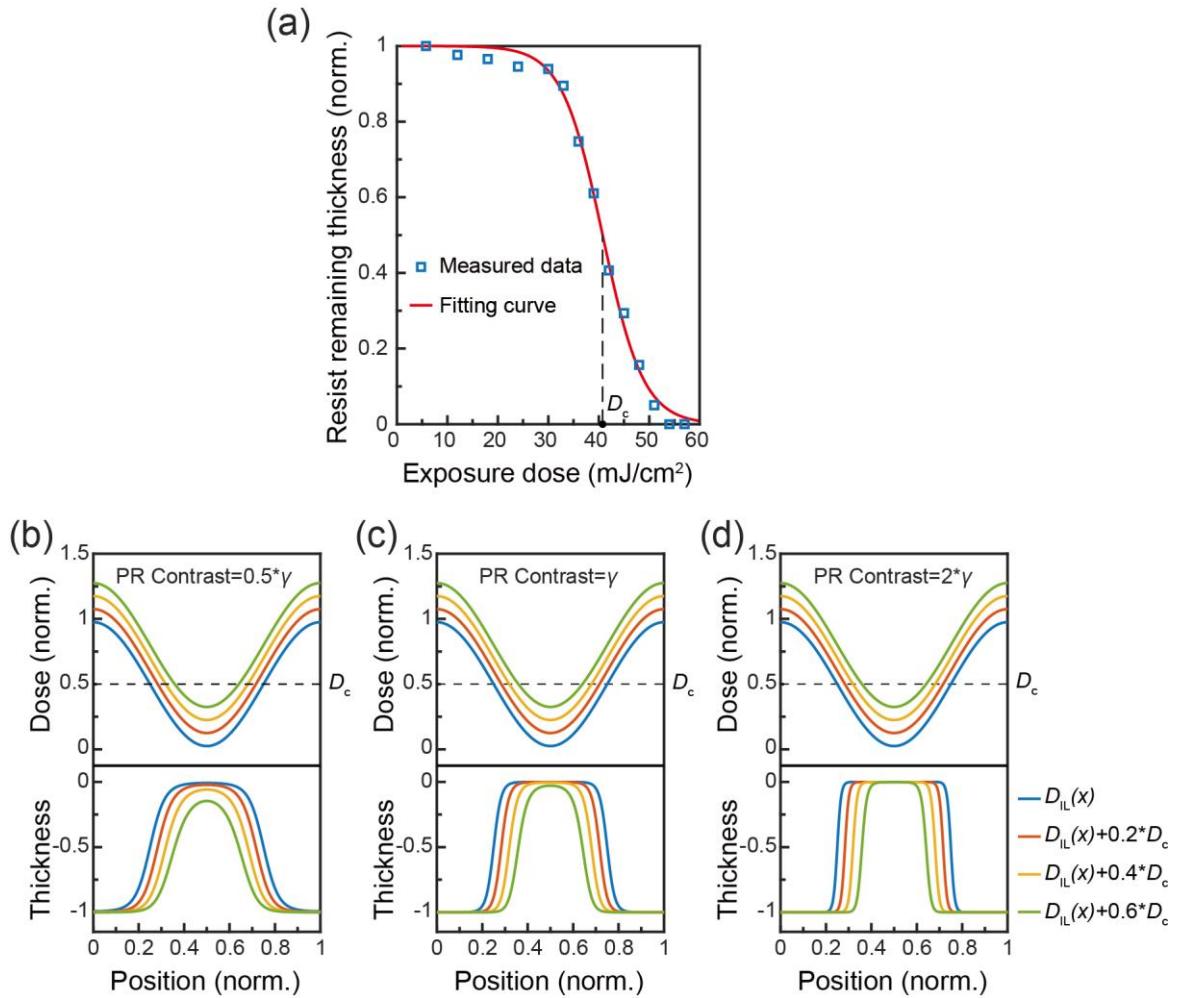


Figure 5-2 The influence of photoresist contrast on IL-GPSE process. (a) Normalized measured photoresist remaining thickness as a function of exposure dose (blue squares) and the corresponding best fitting curve (red line). (b-d) Simulated photoresist profiles using IL-GPSE model by assigning different photoresist (PR) contrasts.

5.2.3 Interference lithography exposure dose distribution

The other factor is the distribution of the IL exposure dose, particularly its contrast, as defined as the relative ratio between the local doses in the constructive and destructive interference regions, which also shows a significant influence on the pattern morphology. The dose distribution in the IL exposure can be numerically modeled from the spatial distribution of the electrical field of the two interference coherent laser beams, by taking

into account the fringe drifting due to environmental disturbance (details in **Chapter 2**), which can be calculated as

$$D_{IL}(x) = D_{IL} \left[1 + \Gamma \cos \left(\frac{2\pi x}{p} \right) \right] \quad (5.2)$$

where Γ is the contrast of the interference exposure dose distribution, p is the grating period, and x is the horizontal position. The total exposure dose distribution is the summation of the IL exposure dose and the secondary exposure dose, which can be described as

$$D_T(x) = D_{IL}(x) + D_{SE}(x) \quad (5.3)$$

where $D_{SE}(x)$ is the distribution of secondary exposure dose. When the secondary exposure is a flood exposure, $D_{SE}(x)$ should be a constant; when it is a grayscale-pattern exposure, $D_{SE}(x)$ should be a variable depending on spatial distribution. The actual nanostructure pattern can be simulated by combining the experimental photoresist characteristic curve in Figure 5-2a and the total exposure dose distribution, enabling the morphology prediction and process analysis in our IL-GPSE method.

Figure 5-3 demonstrates how different interference exposure dose distributions affect the simulated photoresist morphologies with different secondary exposure doses from 0 to $0.6*D_c$, where D_c represents the clearing dose used in simulation for convenience. The full width at half-maximum (FWHM) linewidth shrinks as the secondary exposure dose increases, which conceptually confirms the linewidth modulation achieved by secondary exposure after IL. The comparison of different IL dose distributions shows that a high contrast in the interference exposure significantly enlarges the process window of the linewidth tunability since a low-contrast exposure results in photoresist height loss.

Notably, our home-built IL system has a high contrast (>0.95 , details in **Chapter 2**), which exhibits excellent linewidth tunability.

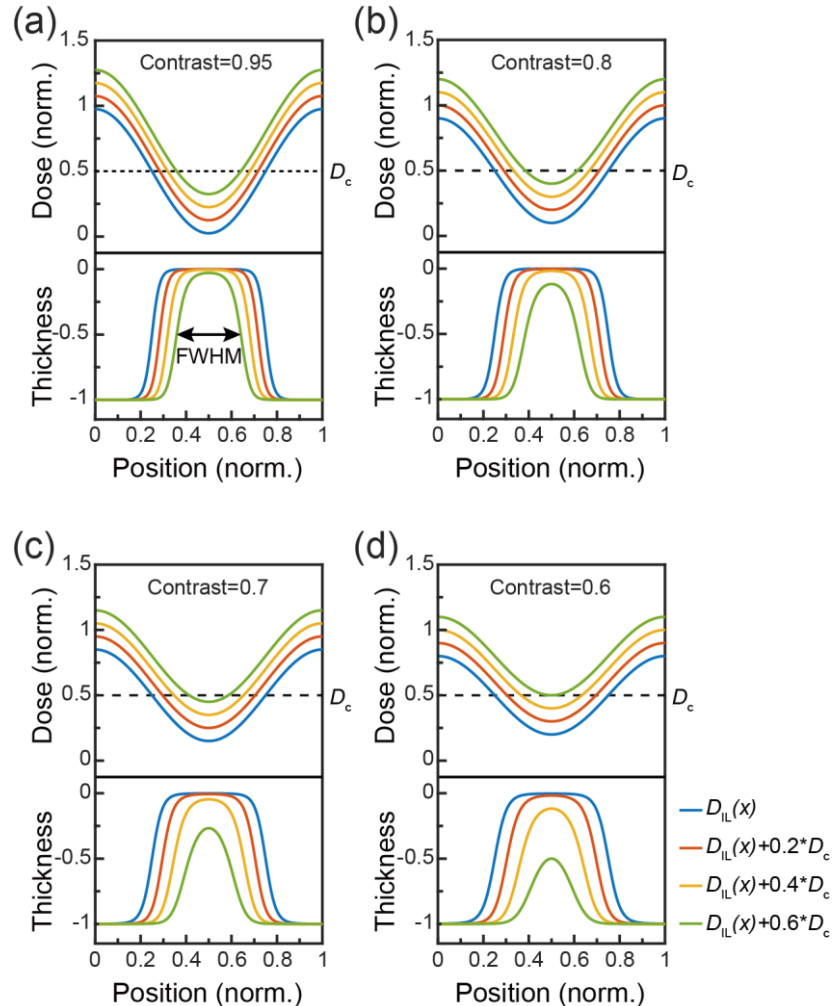


Figure 5-3 The influence of IL dose distribution on IL-GPSE process. Simulated photoresist profiles using IL-GPSE model by assigning different contrasts of the interference exposure dose distribution: (a) 0.95, (b) 0.8, (c) 0.7 and (d) 0.6.

5.3 Experimental demonstration using secondary exposure

To demonstrate the linewidth tunability of the above lithographic strategy, a series of nanogratings with various linewidths were fabricated through the IL-GPSE with different combinations of IL dose and secondary exposure dose. The samples were first exposed

with 1000-nm-period grating patterns with various IL doses from 27.6 to 55.2 mJ/cm², and then followed by the secondary exposure of 8 flood doses ranging from 0 to 13.2 mJ/cm², respectively. Figure 5-4a shows the SEM characterization of these nanogratings, demonstrating a reliable control of the feature sizes by modulating both the initial IL and secondary exposure doses. The FWHM linewidth of the nanogratings was quantitatively characterized and recorded with the corresponding exposure doses in Figure 5-4b, indicating that the samples exposed by different initial IL doses show different linewidth modulation ranges during secondary exposure. For example, the samples of 1000-nm-period gratings exposed by 27.6-mJ/cm² IL dose has a 180-nm modulation range of the linewidth from 590 to 410 nm, while that of 55.2 mJ/cm² IL dose can be tuned for about 140 nm from 300 to 160 nm. Another notable phenomenon is that nanogratings exposed by different exposure combinations may have the similar FWHM linewidth, however, the sidewall morphologies show a great difference since increasing IL dose benefits vertical sidewall while the secondary exposure dose has less effect.

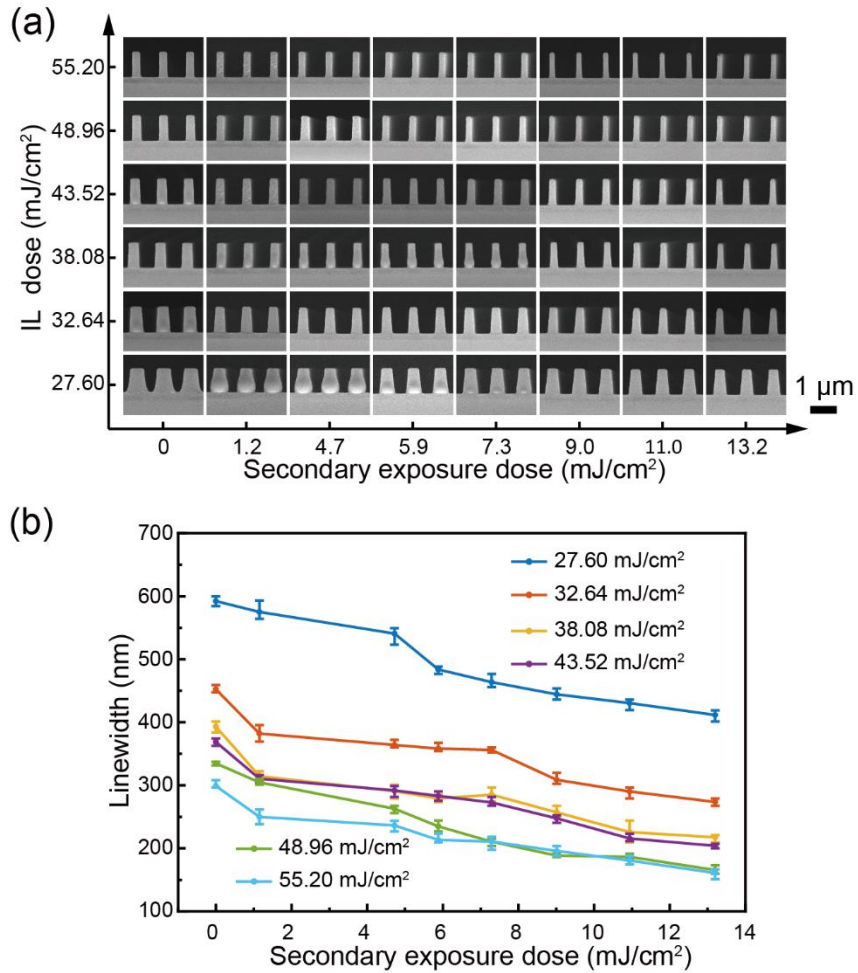


Figure 5-4 Experimental results of IL-GPSE with different combinations of IL and secondary exposure doses. (a) SEM image matrix of 1000-nm-period gratings with various linewidths fabricated by different IL and secondary exposure doses. (b) The FWHM linewidths measured in (a), showing the linewidth is negatively correlated to both IL and secondary exposure doses.

Using the above-mentioned numerical model, we can also simulate the tuning range of the linewidth or the duty cycle with various initial IL exposure doses (Figure 5-5), which exhibit the similar trend as in the experimental measurement in Figure 5-4. Although the above investigation is mainly based on positive-tone photoresist, it's worth to note that the IL-GPSE process can also be applied to negative-tone photoresist (AZ 5206 E,

MicroChemicals, GmbH), as shown in Figure D-1. The linewidth can be modulated from 704 to 831 nm with increasing secondary exposure dose.

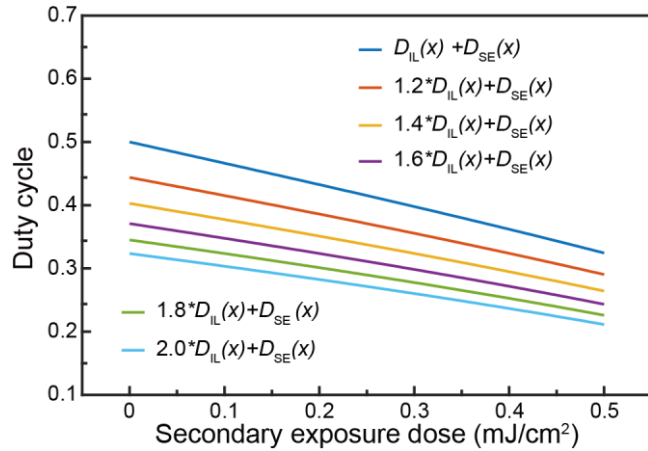


Figure 5-5 The simulated duty cycle variation as a function of the secondary exposure dose using various initial IL exposure doses.

The linewidth manipulation mechanism makes it possible to modulating the nanostructure feature sizes according to a given spatial pattern. The patterned secondary exposure can be realized through a UV projector, a UV mask aligner, or direct laser writing (DLW).

5.3.1 UV projection lithography

In this section, we employ a digital micromirror device (DMD) UV projector for spatially modulating the dimensions of IL-exposed nanopatterns, since the DMD is capable of converting a digital grayscale image into the UV intensity distribution. The photoresist was first exposed with 600-nm-period gratings using IL and then a grayscale image of an HKU logo was projected through a 405-nm projector. The grayscale pattern projected on the pre-exposed photoresist spatially modulates the linewidths according to the digital grayscale image (Figure D-2). Figure 5-6 shows a 3-inch Si wafer carrying the HKU logo, consisting of 600-nm-period photoresist gratings with the linewidths in different regions

modulated by the projected grayscale pattern. SEM images were taken on different parts of the image, including the areas of background, “H”, “K”, and “U” letters respectively, demonstrating the corresponding linewidths of 250, 190, 140 and 110 nm, which indicates a more than 55% linewidth modulation range.

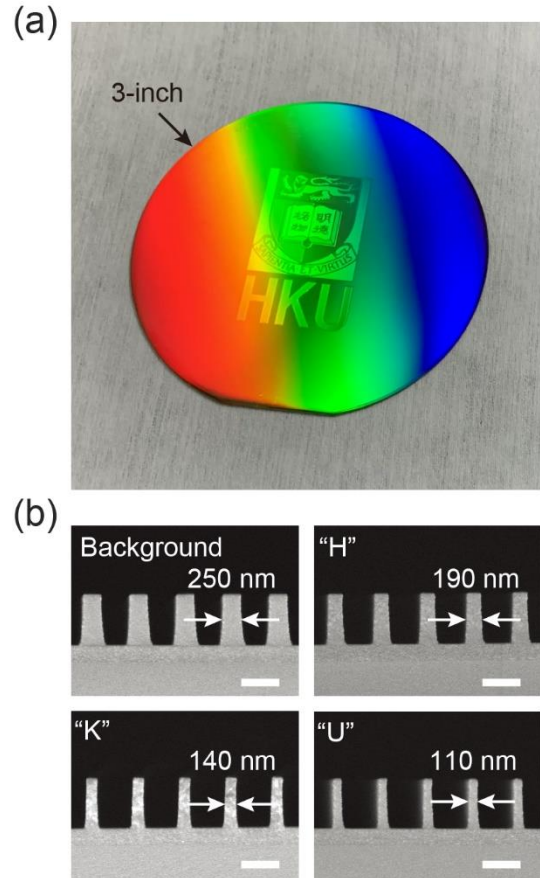


Figure 5-6 Experimental results of IL-GPSE using UV projection lithography. (a) A 3-inch wafer carrying the HKU logo consisting of 600-nm-period photoresist gratings with the linewidths in different regions modulated by projected grayscale pattern. (b) SEM images taken on background, “H”, “K”, and “U” letters on the wafer, showing corresponding linewidths of 250, 190, 140, and 110 nm. Scale bars, 500 nm.

5.3.2 Direct laser writing

Our proposed strategy allows feature size tuning at micrometer scale, subject to the spatial resolution of the grayscale image of the patterned secondary exposure. Since IL exposure creates a nearly uniform or slowly varying latent dose image in the photoresist, the resolution of the feature size modulation mainly depends on the resolution of the secondary exposure. We investigated the spatial resolution of secondary exposure using DLW at different critical dimensions (Figure 5-7a). SEM images show the IL-exposed nanohole array in which some holes are transformed into pillars with a secondary exposure modulation. By characterizing the photoresist variation in Figure 5-7a(iii), the filling ratio of the modulated patterns ranges from over 0.7 to less than 0.4 and demonstrates a spatial resolution of approximately 1.7 microns (Figure 5-7b).

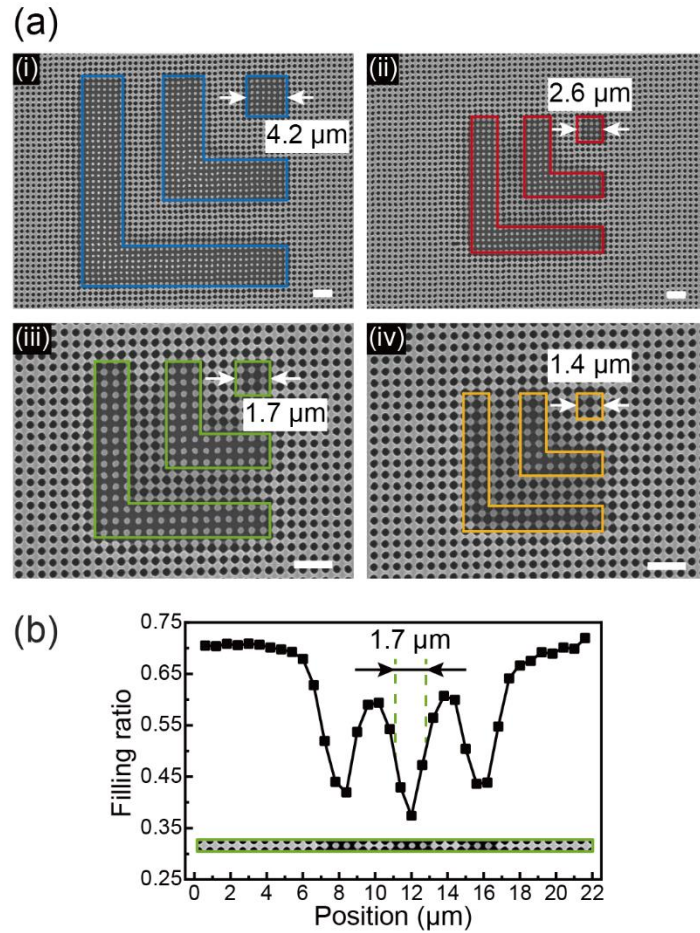


Figure 5-7 Experimental results of IL-GPSE using direct laser writing. (a) SEM images of the spatial resolution test for secondary exposure using direct laser writing with different critical dimensions of (i) 4.2, (ii) 2.6, (iii) 1.7 and (iv) 1.4 μm . (b) Plot of the filling ratio of nanostructures in the green box in (iii) versus the horizontal position, showing a resolution of 1.7 μm . Scale bars, 2 μm .

With single-pixel exposure, we further achieve the fabrication of a photonic crystal pattern with a defect, providing an innovative way to fabricate photonic crystal cavities over a large area for fundamental photonics research and practical device applications, as shown in Figure 5-8.

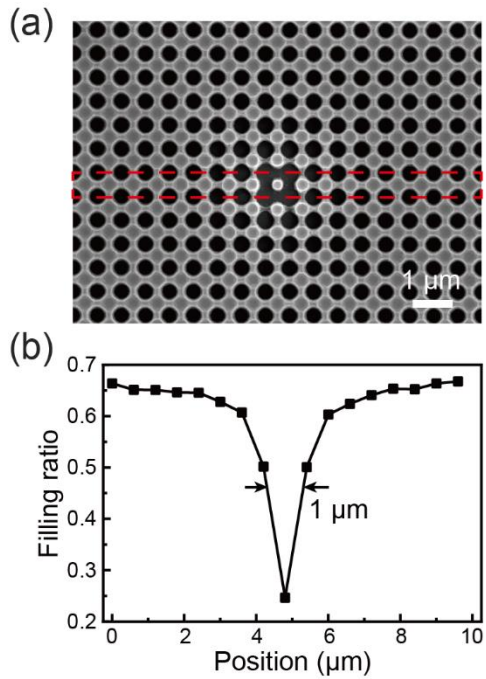


Figure 5-8 Single-pixel modulation using IL-GPSE. (a) SEM image of a 600-nm-period hole array modulated by single-pixel secondary exposure. (b) Plot of the filling ratio of nanostructures in the red box in (a) versus the horizontal position, showing a resolution of 1 μm.

5.3.3 UV contact photolithography

In addition, we also carried out the linewidth modulation on a uniform nanograting using contact photolithography with a photomask. The optical microscope (OM) image in Figure 5-9a shows a 12-point-star pattern consisting of 600-nm-period gratings with 245-nm linewidth inside and 170-nm outside. Figure 5-9b and 9c show the SEM images of the photoresist gratings recorded in the tip regions, labelled using green and yellow boxes, in which the grating linewidth changes within a short distance at the pattern edge. The linewidth distribution is mapped in Figure 5-9b(ii) and 9c(ii) clearly exhibited the tip outlines with a transition distance of approximately 2 microns, as quantitatively analysed in Figure 5-9d. The precise quantitative characterization by measuring the linewidth every

200 nm along a grating line (white) shows a 35-nm/ μ m grating linewidth gradient induced by the edge diffraction of patterned secondary exposure.

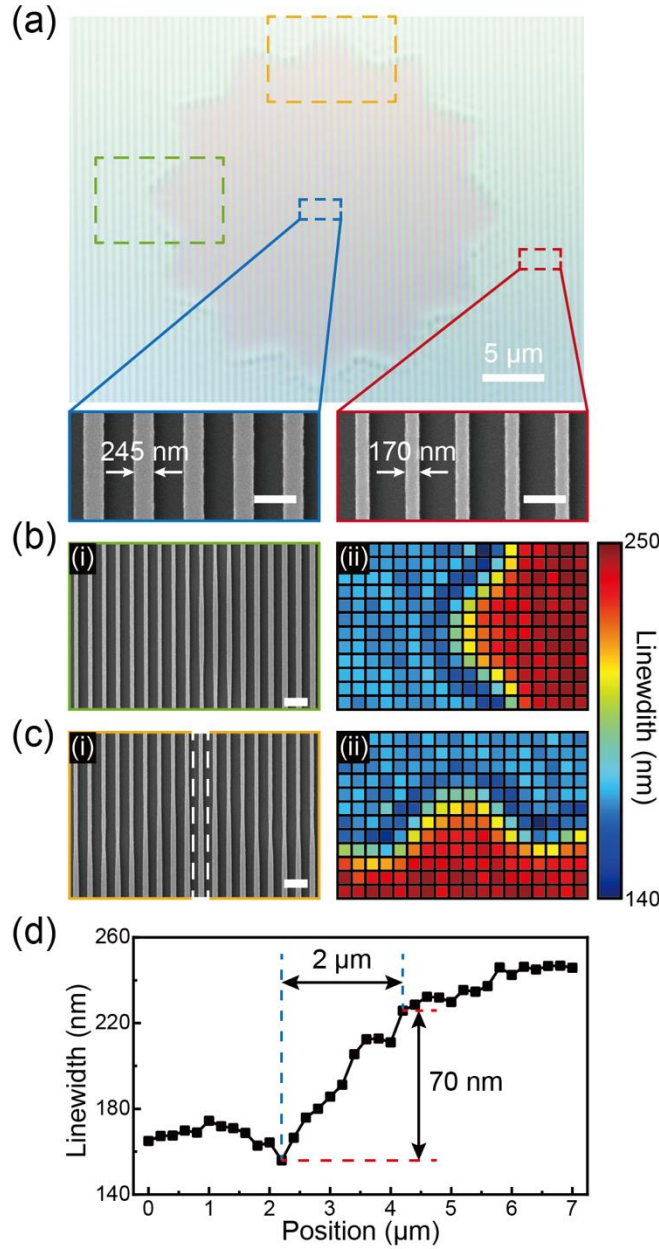


Figure 5-9 Experimental results of IL-GPSE using UV contact Photolithography. (a) The OM image of a 12-point-star pattern, consisting of 600-nm-period gratings with linewidths modulated by contact photolithography using a photomask. SEM images taken inside and outside the secondary exposure pattern, showing the 245-nm and 170-nm linewidths,

respectively. (b) Green-box and (c) yellow-box regions in (a), characterized by (i) SEM images and (ii) linewidth distributions. (d) The linewidth variation measured every 200 nm along a grating line (white), showing the grating linewidth gradient of 35 nm/ μ m. Scale bars, 500 nm (a), 1 μ m (b, c).

5.4 Large-area uniform grating patterning

The proposed IL-GPSE can also be applied on non-uniform nanostructures, which can be caused by the non-uniform laser beam intensity during IL, to compensate the spatial variation for improved uniformity, which is essential in many optical applications that demand large-area uniform gratings^{149,150} and precise interferometry¹⁵¹. Generally large-area nanogratings fabricated by IL suffer radial gradient linewidths due to the Gaussian profile in the interference beams, and researchers often expand the Gaussian beam¹⁵² or implement beam shaping devices to transform the Gaussian distribution to a flat top distribution¹⁵³ to acquire a relatively uniform intensity at the central exposure area. However, the former wastes a large amount of exposure energy and decreases the production capacity while the latter introduces a new challenge of fabricating high-quality large-area beam shaping devices. Employing the secondary exposure with a properly designed intensity distribution after the conventional IL with Gaussian intensity profile offers a new and efficient approach of compensating the linewidth variation (Figure 5-10).

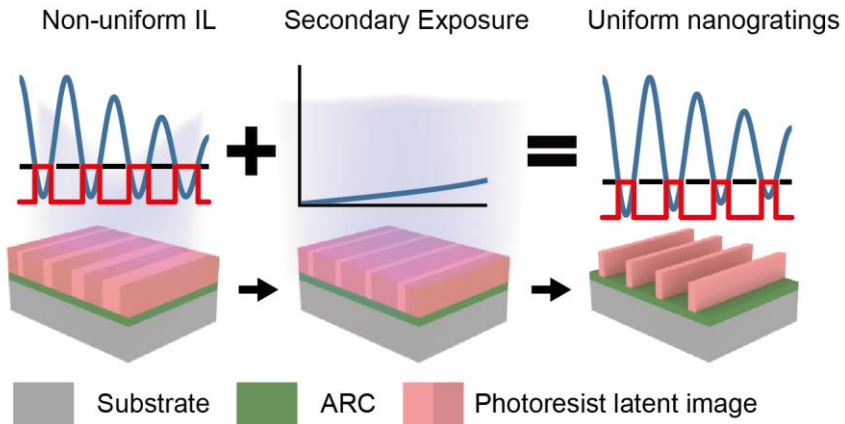


Figure 5-10 Schematic of uniform nanopatterning using secondary exposure to compensate the linewidth variation due to the non-uniform Gaussian beam for IL.

Figure 5-11a shows IL-exposed 400-nm-period gratings over a 4-inch wafer. The diffracted blue light intensity gradually decreases from the center to the edge due to Gaussian intensity distribution (details in Chapter 2), resulting in an increasing linewidth variation from the center to the edge due to the spatially decreasing intensity. We recorded SEM images every 2.5 mm along the radius of the 4-inch wafer (Figure D-3), morphologies of 4 typical positions were illustrated in Figure 5-11b to show the linewidths of 127, 135, 158, and 270 nm, of which a poor control of both linewidth and linewidth roughness was observed near the edge.

In contrast, by performing the secondary exposure with a designed intensity distribution complementary to the Gaussian distribution, the pattern uniformity and line edge roughness can be significantly improved. By referring to SEM images and corresponding linewidth under different IL and secondary exposure doses, as shown in Figure D-4 and D-5, respectively, the secondary exposure intensity map required for compensating the non-uniform IL linewidth variation on the 4-inch wafer can be designed. Figure 5-11e shows the 4-inch intensity map for linewidth tailoring and the devised grayscale image, transformed by using the characterized relation between the digital

grayscale value and projected light intensity via the UV projector (Figure D-6). After applying the secondary exposure with the projected grayscale pattern, a 4-inch wafer carrying gratings with highly homogeneous linewidths was obtained and uniformly diffracted blue light, as shown in Figure 5-11c. SEM images were obtained on both uncompensated and compensated grating samples for comparison, as in Figure 5-11b and 11d, and showed a significant improvement on grating linewidth uniformity and line edge roughness.

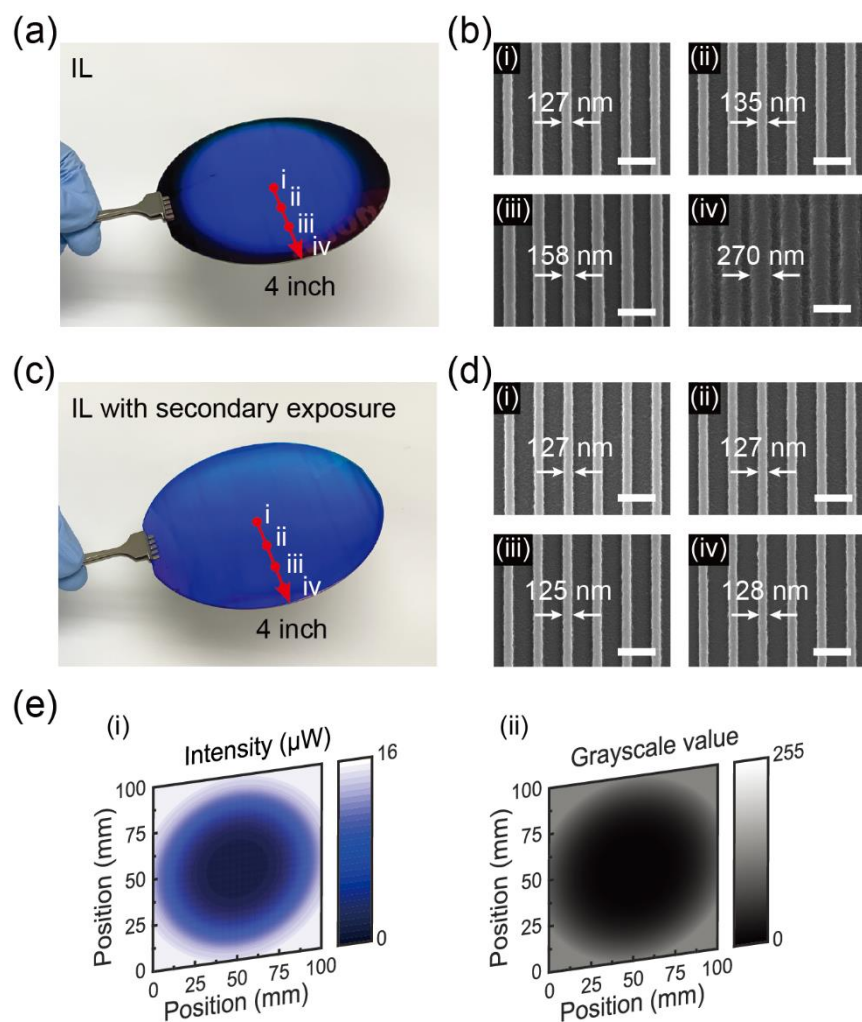


Figure 5-11 4-inch wafer-scale uniform nanogratings fabricated by IL-GPSE. (a) Photograph of IL-exposed 400-nm-period gratings over a 4-inch wafer with the diffracted blue light intensity gradually decreasing from the center to the edge. (b) SEM images taken

in the labelled positions in (a), showing a poor control of linewidth and roughness. (c) Photograph of 400-nm-period gratings over a 4-inch wafer using secondary exposure with a designed projected grayscale pattern after IL exposure, diffracting uniform blue light. (d) SEM images recorded in the labelled positions in (c), showing the uniform linewidth and linewidth roughness. (e) The 4-inch (i) intensity distribution for linewidth tailoring and (ii) devised grayscale image transformed by the characterized relation between the digital grayscale value and projected light intensity via the UV projector. Scale bars, 500 nm.

The linewidth distributions were statistically analyzed by measuring the linewidth of SEM image captured every 2.5 mm along the radius from the wafer center to the edge (Figure D-7). The comparison of linewidth distributions in Figure 5-12a shows that gratings tailored by secondary exposure had a linewidth deviation of 3.2 nm, which is over 1100% reduced from 36.2 nm, that of the gratings exposed only by IL. The SEM images also show that the linewidth roughness was significantly improved through secondary exposure, especially for the gratings near the edge. The difference originates from the total exposure dose on the photoresist, of which a higher dose facilitates the diffusion of photoacid compound. As a result, a more than 580% improvement (from 8.7 nm to 1.5 nm) is obtained in the linewidth roughness characterization when the secondary exposure is employed (Figure 5-12b).

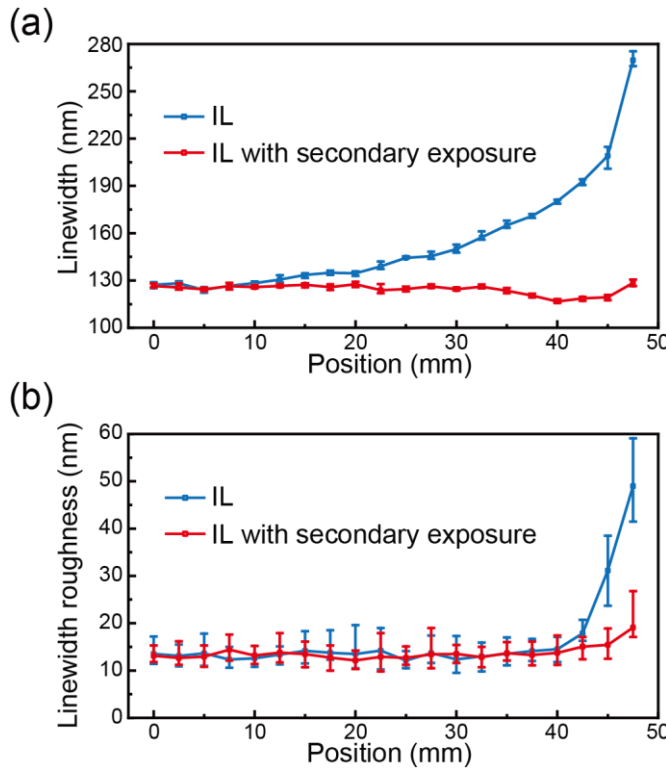


Figure 5-12 Morphological comparison of 4-inch nanogratings fabricated by IL and IL-GPSE. The comparison of (a) linewidth and (b) linewidth roughness distributions over the radius of 4-inch wafers with and without the secondary exposure.

5.5 Summary

In summary, we have invented a practical and scalable lithographic strategy that supports spatial modulation of the feature size of periodic nanostructures on a large area. Our fabrication portfolio uses interference lithography to efficiently fabricate large-area periodic nanostructures and grayscale-patterned secondary exposure to spatially modulate the feature sizes. We successfully fabricated highly uniform nanogratings on a 4-inch wafer by compensating the effect of non-uniform Gaussian profile of the interference laser beams using a grayscale-patterned secondary exposure. Combined with other nanofabrication techniques, we believe that our lithographic strategy can open new

avenues in fabricating large-area nanodevices like flat optics, high-resolution display and portable biosensing.

Chapter 6 High-Resolution and Large-area Grayscale and Structural Color Painting

Combining IL-GPSE lithographic process and pattern transfer techniques, this chapter demonstrates the metasurface application, structural color painting. Using the high-throughput IL-GPSE method to achieve large-area nanopatterning with designed feature size distribution and transferring the pattern into functional materials, the fabricated metasurfaces exhibit various colors due to the unique optical response. Highly relying on electron beam lithography (EBL), most current metasurfaces can only be fabricated on small areas of millimeter scale or less, which limits many practical applications. By adopting the proposed IL-GPSE method, metasurfaces such as structural color paintings can be fabricated on wafer scale, because both the IL and patterned secondary exposure can be done at large scale while maintaining sufficiently high resolution. Using the photoresist pattern as an example, various paintings constructed of nanostructures are demonstrated including grayscale, color, high resolution, and wafer-scale size, etc. Transferring the lithographic resist pattern into solid material using the aforementioned TLR process, the metasurface based on Mie resonator is also demonstrated with high stability and durability.

6.1 Introduction

Colors play crucial roles in daily lives due to the ability of carrying information^{154,155}. Generally, colors are generated from pigments or dye by absorbing light of certain wavelengths, such as paints and flowers¹⁵⁶. However, the coloration using pigments or dye has a poor resolution (eg. <1000 dpi) because the particle sizes are at least dozens of micrometers. Moreover, limited by the intrinsic material characteristics, the colors

produced by pigments and dyes are not easy to be finely tuned for exhibiting grayscale details. Recently, structural color, based on the light-matter interaction with artificial structures, has been deeply investigated and developed, including diffraction of periodic nanopattern^{157,158}, plasmonic colors of metallic structures^{159,160}, Mie scattering of dielectric materials^{161,162}, bionic colors of photonic crystal^{163,164}, thin-film interference iridescence^{165,166}, etc. The structural coloration using nanoscale building blocks attracts the most interest for its ultrahigh resolution due to the sub-micrometer-scale pixel sizes. Besides, these structural colors are resistant to fading because they can be made of solid metallic or dielectric materials.

Most structural color metasurfaces using artificial nanostructures highly rely on serial writing techniques such as EBL or FIB, which need a long processing time for large-scale nanopatterning. Although photolithography and NIL are feasibly demonstrated for mass production, there are concerns that the fabrication of large-area photomasks and templates is still challenging. Thus, employing the proposed IL-GPSE strategy to achieve the high-throughput nanofabrication large area, the structural color paintings constructed of spatially varying nanostructures can be easily obtained. A variety of paintings are demonstrated using the photoresist, including grayscale, colors, high resolution, and wafer-scale sizes. By transferring the pattern into specific materials, more colors based on mechanisms of the Fabry-Pérot cavity and Mie resonator are also demonstrated, indicating the scalability and versatility of our methods in broader areas.

6.2 Grayscale paintings

In addition to linewidth modulation of nanogratings introduced in **Chapter 5**, the secondary exposure also enables the filling ratio tunability of IL-exposed 2D nanostructures, as shown in Figure 6-1a. By employing IL on the photoresist twice

followed by secondary exposure with designed spatial dose distribution, the filling ratio of the IL-exposed 2D nanopattern can be spatially modulated. SEM images recorded in Figure 6-2b show the resist evolution during secondary exposure, demonstrating the nanopattern can be transited from the initial nanoholes to nano-checkerboards and then to nanopillars.

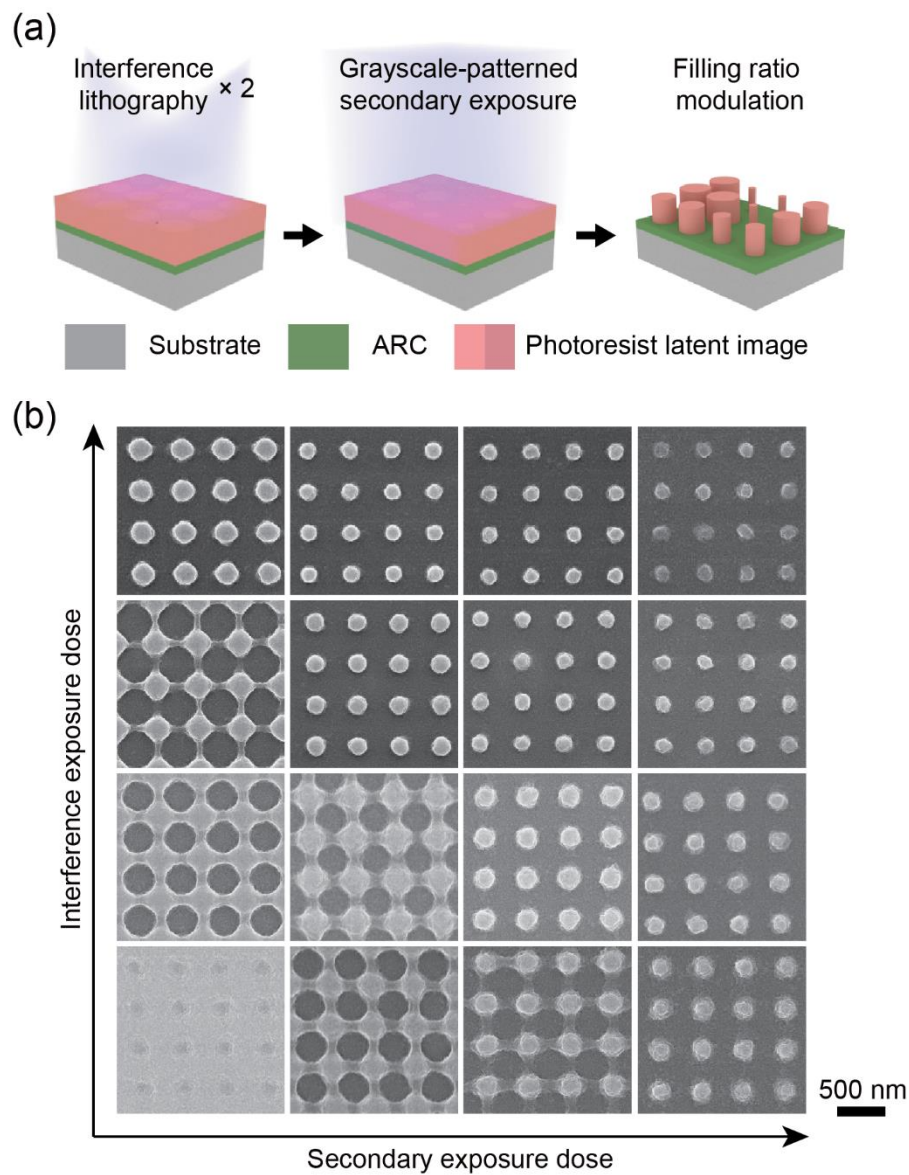


Figure 6-1 (a) Schematic of spatial modulation of filling ratio for 2D nanostructures using IL-GPSE. (b) SEM image matrix of 400-nm-period 2D pattern with various filling ratios fabricated by different IL and secondary exposure doses.

6.2.1 High-resolution grayscale painting

Using DLW as the secondary exposure, the spatial resolution of the size-modulated nanopattern can achieve sub-1 μm resolution (Figure 5-8). Thus, high-resolution painting can be realized by constructing nanoscale building blocks via tuning localized dimensions of IL-exposed periodic nanopatterns. The grayscale details of the micrometer-scale painting can be observed in SEM characterization through the nanostructures' filling ratio change. Figure 6-2 shows several miniaturized grayscale paintings of Girl with a Pearl Earring, The Starry Night, and a cute American shorthair cat, with the painting size of only dozens of micrometers. The grayscale details of original images are perfectly preserved in the SEM images, which enables the ability to achieve high resolution up to 25, 400 dpi. Such ultrahigh resolution paintings are promising in applications of optical data archival, anti-counterfeiting, and encoding, etc.

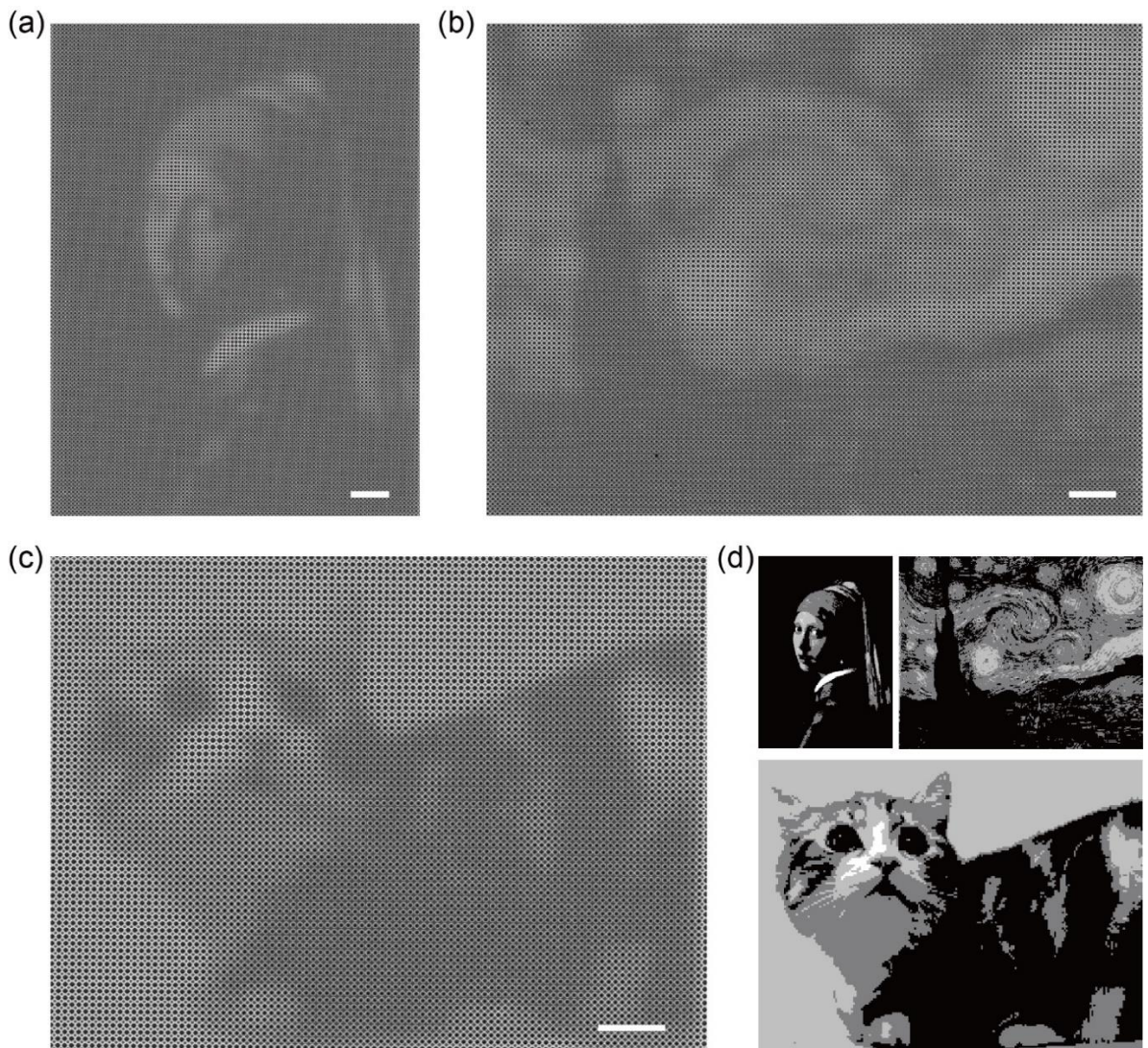


Figure 6-2 Ultrahigh-resolution grayscale paintings constructed of nanostructures patterned by IL-GPSE. SEM images show the paintings of (a) *Girl with a Pearl Earring*, (b) *The Starry Night*, and (c) a cute American shorthair cat. (d) The original grayscale images for secondary exposures, where the grayscale implies doses. Scale bars, 10 μm .

6.2.2 Large-area grayscale painting

Most reported structural color research using 2D nanostructures is demonstrated on small areas such as millimeter scale or less because they need to use EBL, which is extremely expensive and time-consuming for large-area patterning. By adopting IL-GPSE method, structural color paintings can be fabricated on wafer scale, because both the IL

and patterned secondary exposure can be done at large scale while maintaining sufficiently high resolution. However, a factor that needs to be considered is that the diffraction-induced coloration caused by the nanostructure periodicity will interfere with the designed structural color, especially over large-area samples^{167,168}. We intentionally adopt a microscopically roughened surface to mitigate this diffraction effect by randomly scattering the diffracted light. We applied the IL-GPSE process on the unpolished side of a Si wafer and investigated the structural color variation under various secondary exposure intensities. As shown in Figure 6-3a, 25 squares of 700-nm-period 2D patterns on photoresist modulated by secondary exposure projection show a clear grayscale color change from dark brown to light gold, of which the corresponding reflectance increases (Figure E-1). SEM characterization shows non-uniform 2D periodic nanopatterns on the microscopically irregular surface (Figure 6-3b and Figure E-2), from which the filling fraction of photoresist can be extracted (details in Section 6.4). Figure 6-3c demonstrates that the photoresist filling ratio is negatively correlated to the secondary exposure dose, which confirms the lateral filling ratio modulation by secondary exposure enables the grayscale tunability.

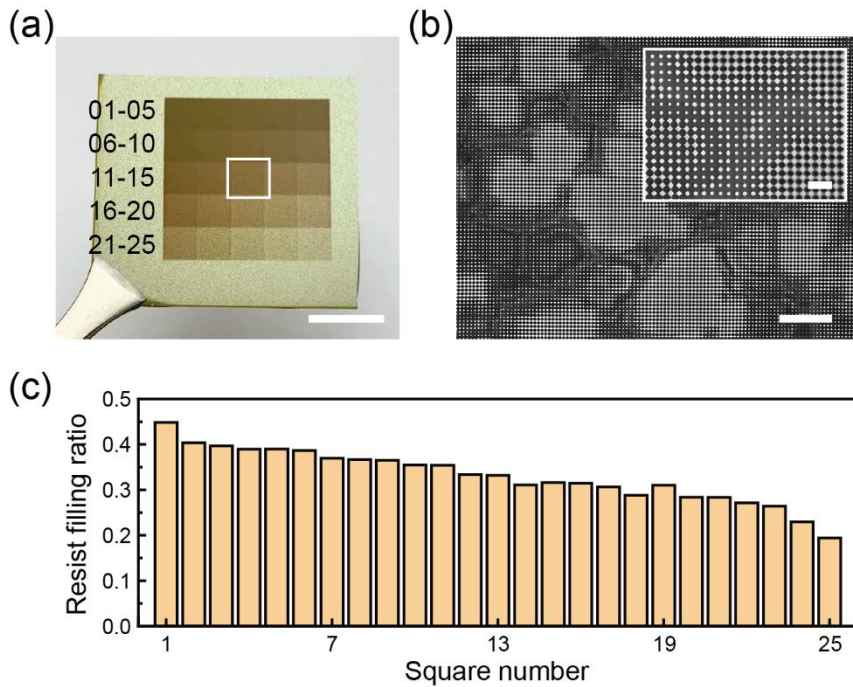


Figure 6-3 The grayscale tuning on wafer scale. (a) The photograph of 25 squares of 700-nm-period 2D patterns on photoresist modulated by secondary exposure projection, showing a clear grayscale change from dark brown to light gold. (b) SEM images of the region labelled using white box in (a). (c) Fraction area of photoresist calculated from SEM images of Figure E-2, showing a negative correlation between the photoresist filling ratio and the secondary exposure dose. Scale bars, 2 μm (inset in b), 10 μm (b), and 1 cm (a).

Therefore, the wafer-scale grayscale painting can be demonstrated by employing wafer-scale IL-GPSE. The secondary exposure projects part of the renowned Chinese artistic painting *Along the River During the Qingming Festival* (Chinese name: *Qingming Shanghe Tu*) by Zhang Zeduan (1085-1145) (Figure E-3) on a 3-inch wafer, consisting of a latent image of 700-nm-period 2D patterns in the photoresist. After photoresist development, a grayscale replication of the painting appears on the Si substrate (Figure 6-4a). When the wafer is tilted at different angles, a dynamic structural color due to the residual diffraction can also be observed (Figure 6-4b), indicating potential applications in

cryptography or anti-counterfeiting. Moreover, pattern transfer into other materials can be realized by combining IL-GPSE strategy with other nanofabrication techniques such as RIE and electron beam evaporation (EBE). As an example, Figure 6-4c and 4d show the grayscale paintings of *Girl with a Pearl Earring* engraved in a 300-nm-thick SiO₂-coated Si wafer and deposited with 50-nm-thick Ag on a glass substrate, respectively.

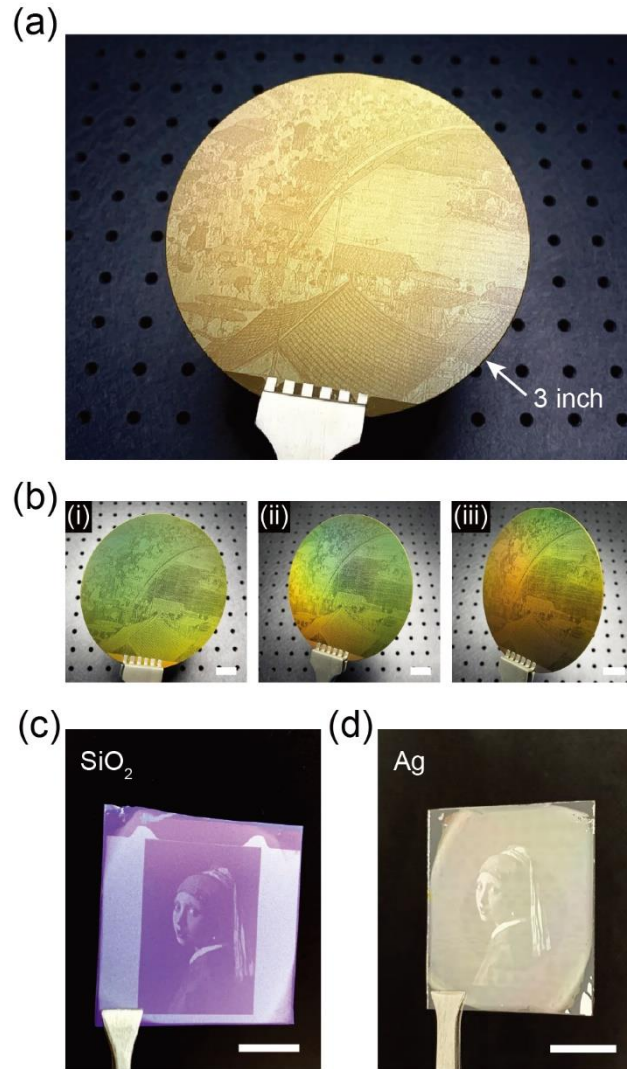


Figure 6-4 Large-area grayscale painting on 3-inch wafer. (a) A photograph of the 3-inch grayscale painting of *Along the River During the Qingming Festival* in photoresist patterned by IL-GPSE. (b) A dynamic structural color due to the residual diffraction at tilting angles. Grayscale paintings patterned by IL-GPSE are further (c) etched into 300-

nm-thick SiO₂-coated Si wafer, and (d) deposited with 50-nm-thick Ag on glass. Scale bars, 1 cm (b-d).

6.3 Structural color paintings

Assigning the nanostructures with different geometries and materials, a variety of colors can be produced due to mechanisms of light diffraction, surface plasmon resonance or Mie resonance, etc. For example, exposing the photoresist into a butterfly pattern composed of two different geometries of 1-μm-period orthogonal and 360-nm-period hexagonal 2D patterns, OM images in Figures 6-5 show different colors (green and blue on wings), indicating the versatility and utility of IL-GPSE in structural color metasurfaces.

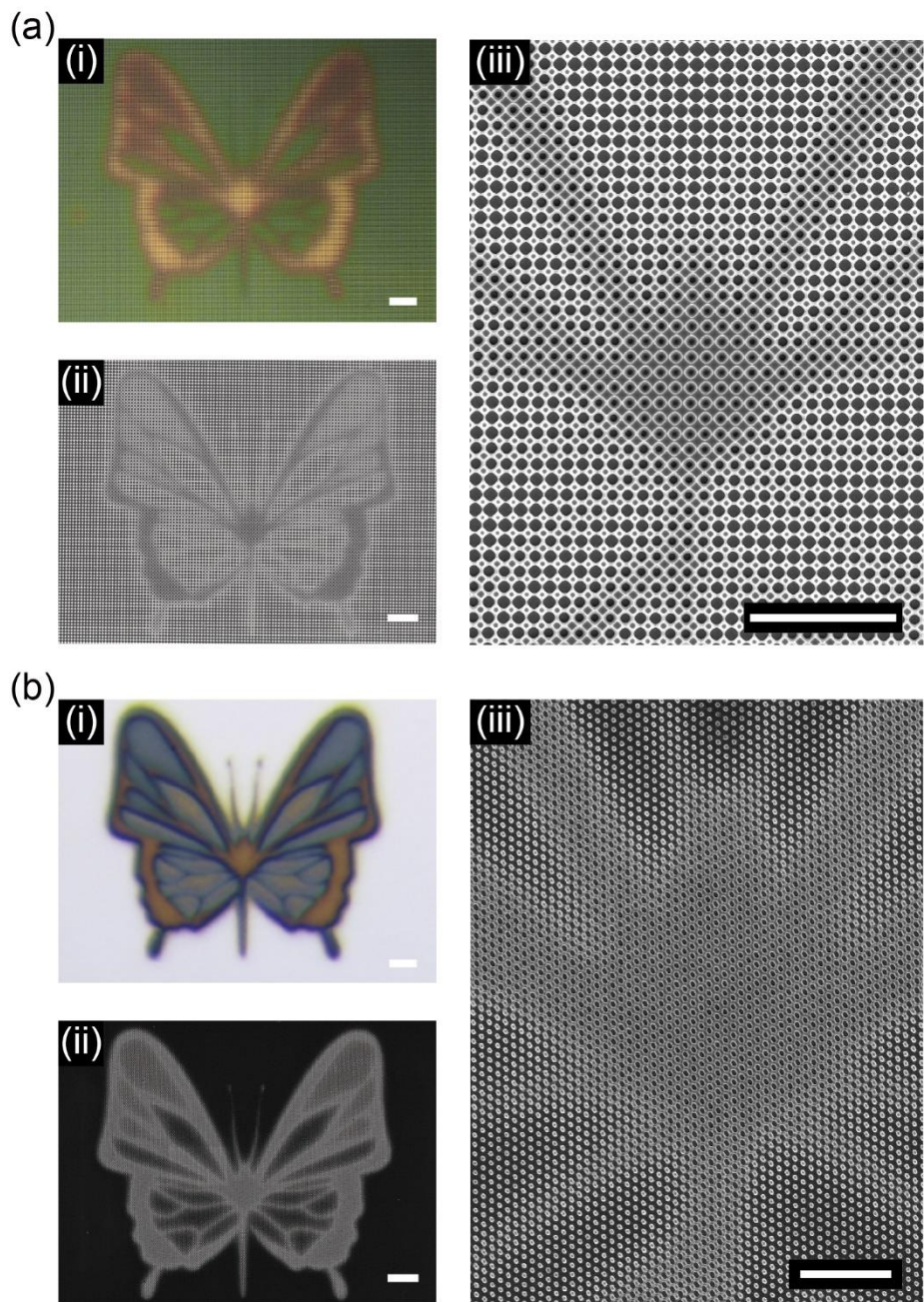


Figure 6-5 Different colors produced by different nanostructures. (a) (i) OM, (ii) SEM and (iii) zoom-in SEM images showing a butterfly pattern composed of 1- μm -period nanostructures with orthogonal lattices. (b) (i) OM, (ii) SEM and (iii) zoom-in SEM images showing a butterfly pattern composed of 360-nm-period nanostructures with hexagonal lattices. Scale bars, 10 μm .

6.3.1 Structural color based on Fabry-Pérot cavity resonances

In addition to the period and lattice of the nanoscale building blocks, we also demonstrate the structural color for higher color coverage by devising structures. By adopting a simple structure of a size-tuned photoresist pillar array on the silicon substrate followed by etching the ARC layer, a vivid structural color with a larger coverage based on Fabry-Pérot cavity resonance¹⁶⁹⁻¹⁷¹ is demonstrated in Figure 6-6.

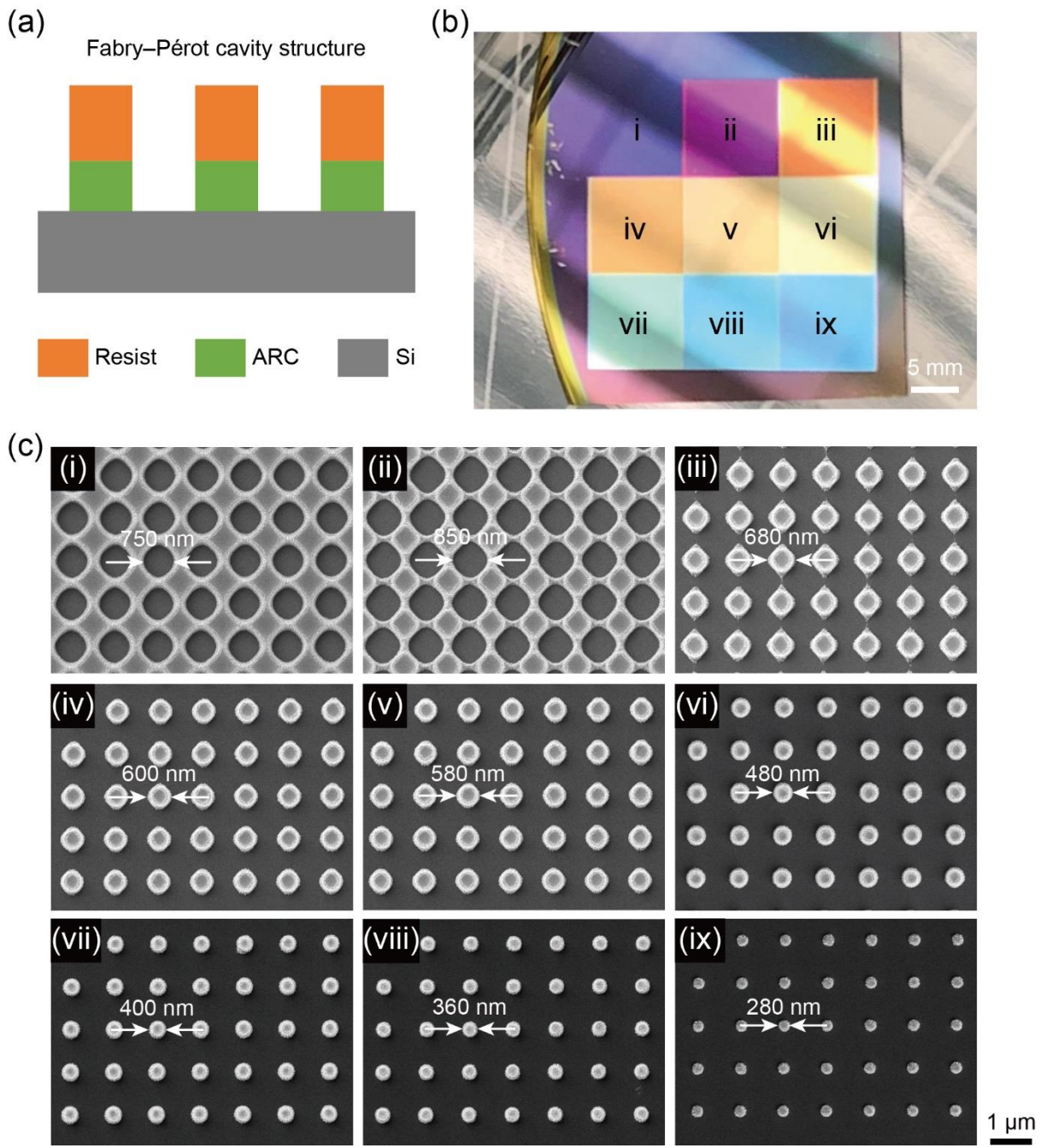


Figure 6-6 Structural color demonstration based on Fabry-Pérot cavity resonance. (a) Schematic of the Fabry-Pérot cavity structure using photoresist, etched ARC and Si substrate. (b) The fabricated centimeter-scale metasurface displaying various structural colors. (c) SEM images of different regions in (a), showing nanostructures with different feature sizes modulated by IL-GPSE.

6.3.2 All-dielectric structural color paintings

Transferring the size-modulated pattern into other functional material, we also demonstrate the structural coloration with all dielectric metasurface. Due to the high refractive index (Figure E-4), high compatibility with mature CMOS fabrication and long-time durability for common use, Si is chosen as the Mie resonator^{133,172,173}. Figure 6-7a depicts the schematic illustration of the metasurface unit cell, composed of a Si nanopillar placed on the fused silica substrate. The height and period are fixed at 220 and 400 nm, and the diameter is varying parameter that can be tuned by IL-GPSE method. FDTD simulation is employed for calculating the metasurface's reflectance with different Si pillar diameters ranging from 80 to 180 nm, corresponding to the colors from green to pink (Figure 6-7b). Resonances can be clearly observed at 554 and 634 nm when assigning the nanopillars with diameters of 100 and 160 nm, of which the electric and magnetic field distribution can be seen in Figure 6-7c, respectively. Therefore, we fabricated a centimeter-scale structural color metasurface based on the Mie resonances of Si nanopillars, showing a Chinese map (Figure 6-7d). The provinces and regions are distinguished by tuning the color and saturation through modulating the nanopillar diameters.

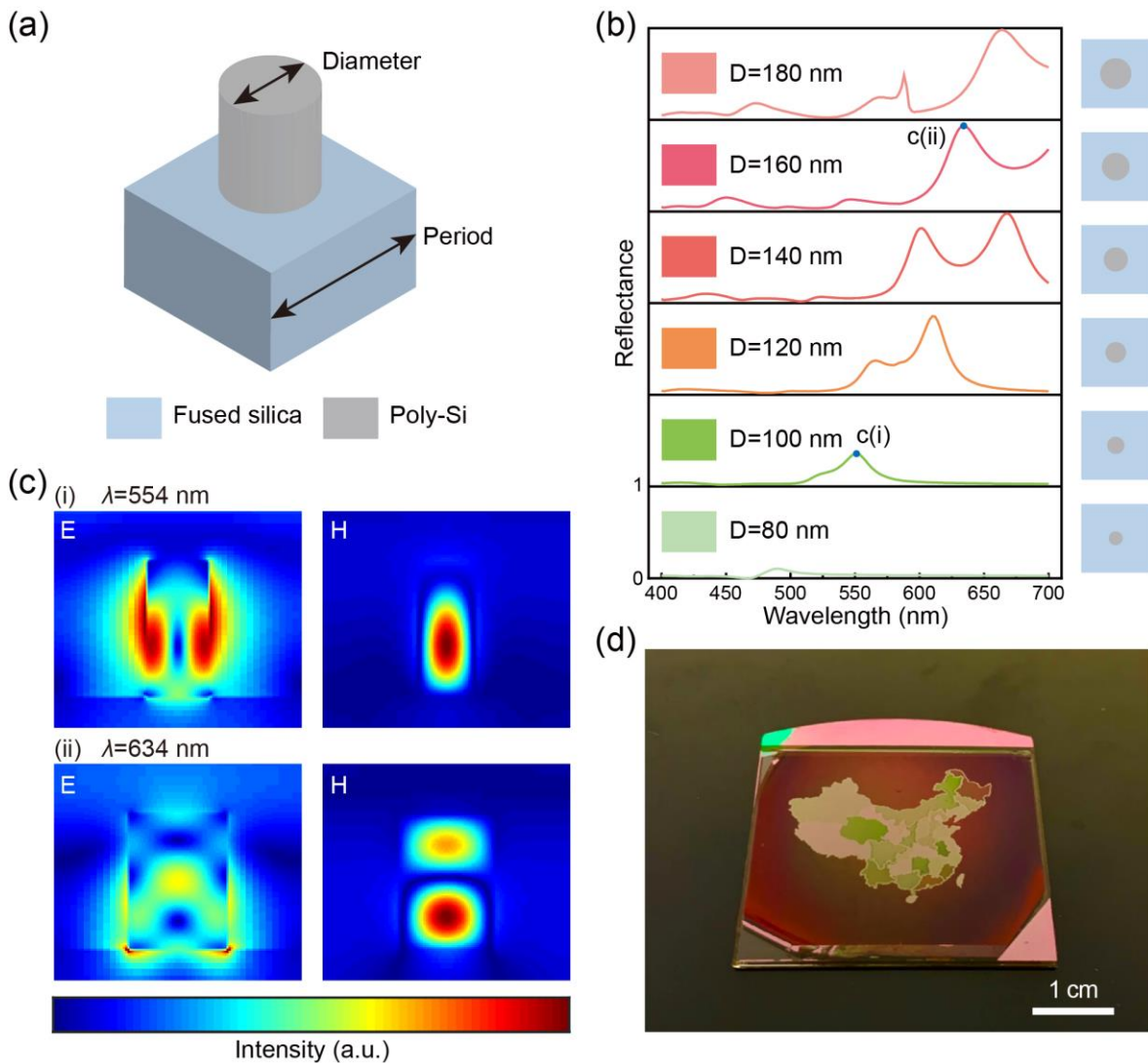


Figure 6-7 All-dielectric structural color painting based on Mie resonances. (a) Schematic illustration of the metasurface unit cell composed of Si nanopillar on a fused silica substrate. The height of the pillars is 220 nm, the period is 400 nm, and the diameter is a varying parameter. (b) FDTD simulated reflective spectra of the Si metasurface with different diameters ranging between 80 nm (light green) and 180 nm (pink). The insets are the corresponding structural color. (c) Spatial distributions of the simulated electromagnetic field for Si nanopillars with diameters of (i) 100 nm and (ii) 160 nm. (d) The photograph of the all-dielectric Si metasurface, showing a map of China with the provinces distinguished by structural colors.

6.4 Experimental details

6.4.1 Fabrication methods

For the grayscale painting of *Along the River During the Qingming Festival* in Figure 6-4a, IL-GPSE was employed on the backside of a 3-inch 200-nm-thick SiO₂-coated silicon wafer, spin-coated with 200-nm-thick ARC and 800-nm-thick photoresist. For the grayscale painting of Girl with a Pearl Earring in Figure 6-4c, IL-GPSE was first employed on the backside of a 300-nm-thick SiO₂-coated silicon substrate, spin-coated with 200-nm-thick ARC and 800-nm-thick photoresist. After patterning on the photoresist, the underlying ARC and SiO₂ layers were etched using O₂ plasma and CHF₃/H₂ in a reactive ion etching system (RIE-10NR, Samco), respectively, to transfer the pattern into SiO₂. Finally, the photoresist and ARC residues were removed to complete the grayscale painting. For the grayscale painting of Girl with a Pearl Earring in Figure 6-4d, IL-GPSE was first employed on a glass substrate, spin-coated with 200-nm-thick ARC and 800-nm-thick photoresist. After patterning in the photoresist, the underlying ARC layer was etched using O₂ plasma to expose the surface of glass. Next, 50-nm-thick Ag was deposited using electron beam evaporation (EB500-I, Shenyang Scientific Instrument Ltd.). Finally, a lift-off process was performed with ultrasonic cleaning in RCA-1 solution (NH₃·H₂O: H₂O₂: H₂O = 1: 1: 5) at 80 °C for 3 min, leaving the glass substrate with Ag grayscale pattern.

For the structural color painting of the Chinese map Figure 6-7d, the cleaned fused silica was first deposited with a 220-nm-thick polycrystal Si layer using low pressure chemical vapor deposition (LPCVD). Next, IL-GPSE was employed on the substrate coated with 200-nm-thick ARC, 25-nm-thick SiO₂ and 300-nm-thick photoresist, generating the size-modulated Chinese map composed with nanopillars with different

diameters. With the tri-layer resist process mentioned in **Chapter 3**, the pattern can be etched into poly-Si layer to form the Mie resonator.

6.4.2 Instrument and characterization

Extraction of the photoresist filling ratio

SEM images are saved as uint16 data type which shows morphological information of nanostructures using 256 grayscale values. In the SEM images, the photoresist appears brighter while the exposed silicon surface appears dark. By obtaining the grayscale values of all pixels and setting a properly chosen threshold, the number of pixels that are covered by photoresist can be counted and the photoresist filling ratio can be calculated.

Instrument for grayscale and color characterization

SEM (Zeiss Sigma 300) was performed to characterize the morphologies of the nanostructures. SEM images were analyzed by a commercial software ProSEM (GenISys Ltd.) statistically calculate the linewidth and roughness. The photoresist thickness was measured by an ellipsometer (TF-UVISEL, HORIBA Jobin Yvon). The light intensity was measured by a commercial digital power meter (PM160, Thorlabs, Inc.). The reflective spectra were collected using a commercial spectrometer (QE65Pro, Ocean Optics).

6.5 Summary

In summary, grayscale and structural color paintings using nanostructures are demonstrated through IL, grayscale-patterned secondary exposure, and pattern transfer techniques. Using IL-GPSE to modulate feature sizes that enable the grayscale and color tuning, high-resolution, wafer-scale paintings are demonstrated. Separating high-resolution patterning of metasurface building blocks and the size modulation to achieve high-throughput, large-area patterning of nanostructures with spatially modulated sizes, this

approach can improve the patterning efficiency by orders of magnitude when compared with EBL. Additionally, this lithographic process enables easy compatibility with pattern transfer techniques for fabricating functional nanostructures that can be widely used in metasurface applications.

Chapter 7 Conclusions and Outlooks

7.1 Concluding marks

As a traditional classical nanopatterning approach, IL has been investigated and developed for several decades and adopted in many research fields due to its advantageous fabrication abilities of high resolution, high throughput, and large scale. In regard to the drawbacks of conventional IL of complicated optical configurations and poor pattern flexibility, we propose a versatile IL system and devise process portfolios to transfer the exposed pattern into functional materials or onto unconventional surfaces (Figure 7-1).

The innovations in IL, have been discussed in **Chapter 2, 3 and 5**. In **Chapter 2**, we introduced a novel IL configuration that uses flexible fiber-optics to guide and expand the laser beam, enabling the fast period reconfigurations. The self-designed active phase-locked system ensures the high-level interference pattern contrast, which has been numerically and experimentally demonstrated of great importance in the feature size modulation of IL. Using the setup, we demonstrate the nanopatterning of super-resolved linewidth of sub-50 nm, ultra-high aspect ratio (>6), and wafer-scale (3-inch). Based on the high-aspect-ratio nanostructures that benefit deposition and etching processes, we also demonstrate the fabrication of NIL molds with diverse profiles.

Chapter 3 proposed a process optimization strategy for IL, using TMM and FDTD numerical modeling. Applying the simulation in the high-fidelity tri-layer process to optimize the resist coating combinations, the experimental results demonstrated that different combinations would cause the standing wave phenomenon with different levels. We also extend this strategy to more complex substrates to obtain IL patterns of higher

quality, which indicates that our reliable optimization strategy is very practical in the nanofabrication process.

In **Chapter 5**, we invented a lithographic process portfolio that enables spatial modulation of feature size for IL-exposed nanostructures. Just adding a step of secondary exposure after IL, the spatial modulation of dimensions can be achieved, of which the resolution can be down to sub-wavelength scale and the area can be up to wafer-scale. Different from the conventional pixel-by-pixel writing (EBL, FIB, DLW) and batch replicating (photolithography, NIL) techniques, this method separates high-resolution nanopatterning and the size modulation, significantly enhancing the patterning efficiency and flexibility. Using this novel process, we demonstrated the highly uniform 4-inch nanogratings with and impressively fancy 3-inch structural color painting.

The other part of this dissertation mainly focuses on developing large-area, high-fidelity pattern transfer techniques. The above-mentioned high-aspect-ratio resist nanostructures are beneficial for deposition and etching processes, enabling the fabrication of NIL molds with diverse profiles (**Chapter 2**). The tri-layer process optimized by numerical simulation also offers opportunities for fabricating perfect nanopatterns on complex substrates, achieving high-fidelity pattern transfer into functional materials (**Chapter 3**). In **Chapter 4**, we introduced a nanotrasnfer technique that can transfer the pre-fabricated nanostructures onto diverse unconventional surfaces. This approach uses water-soluble material to embed nanostructures and then attaches to the targets via electrostatic adhesion, which ensures the nanopatterning of cleanliness, high fidelity, and high transfer yield. Based on this, we demonstrated nanotrasnfer on various substrates including lens, optical fiber, and 2D materials, etc.

The numerical analysis and fabrication techniques mentioned in this dissertation can be flexibly combined with each other and integrated with other advanced nanoscience techniques for broadening application fields. Using the structural coloration as the example (**Chapter 6**), the proposed structure generation, size modulation, and pattern transfer techniques are integrated for the demonstration of solid structural color metasurface based on Mie resonance.

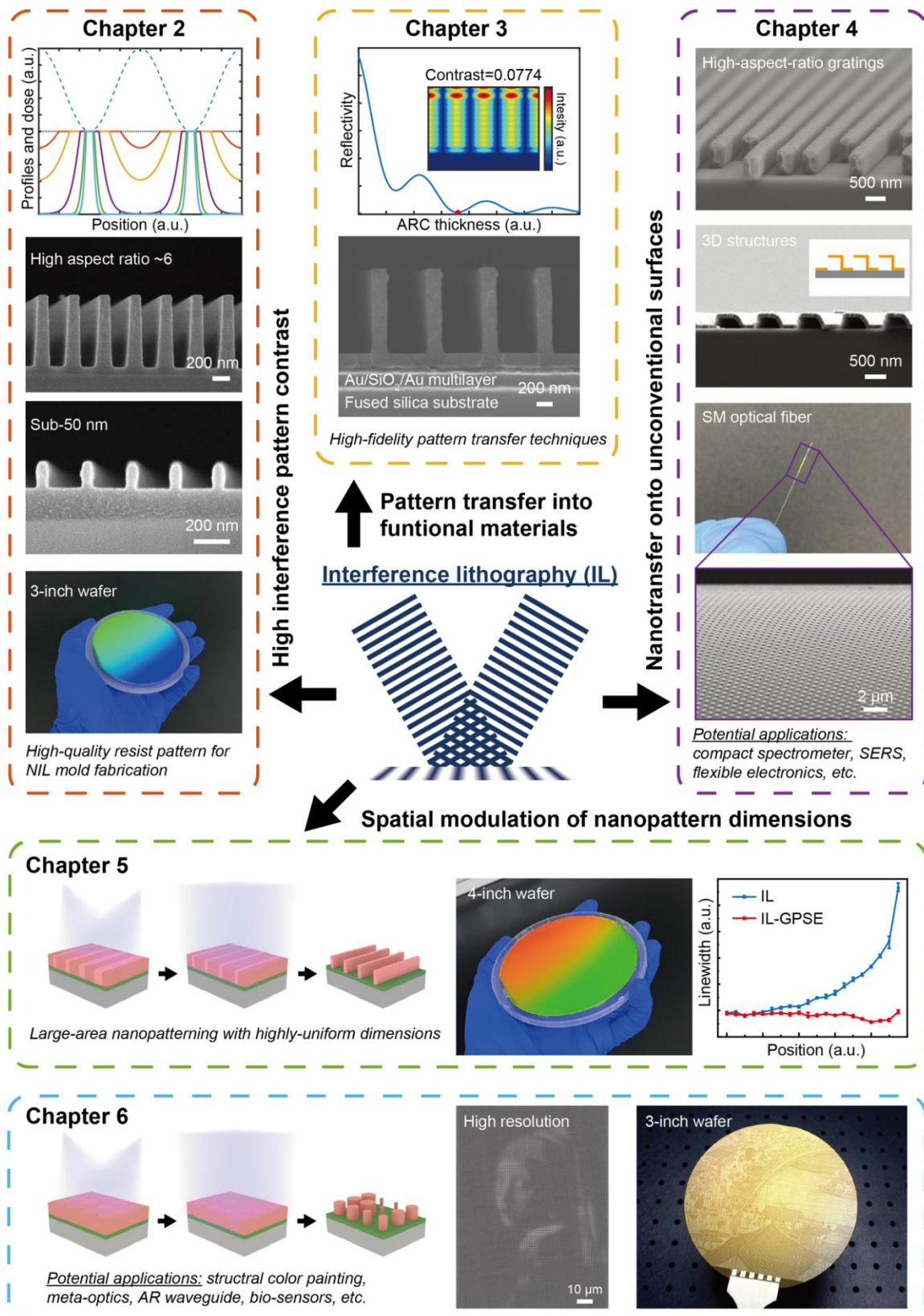


Figure 7-1 Conclusions of this dissertation: The fabrication and applications of nanostructures through interference lithography and pattern transfer techniques.

7.2 Future directions

The fast-reconfigurable 2-FOIL system introduced in **Chapter 2** can be combined with multi-axis motorized stages for versatile functions such as the nanopatterning of multiple periods. An emerging application of the AR display using surface-relief diffraction gratings needs to place nanogratings of different periods on specific positions for light in-coupling, turning, and out-coupling¹⁷⁴. Figure 7-2 shows the initial prototype of our designed automated 2-FOIL system and the fabricated nanopattern for the diffractive waveguide.

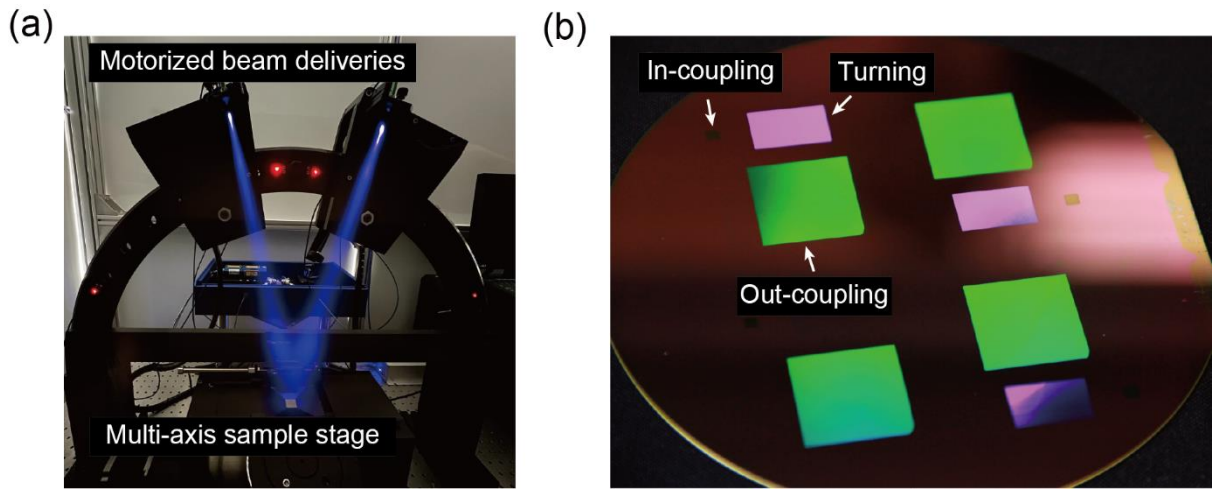


Figure 7-2 (a) Initial prototype of home-built automated 2-FOIL system. (b) Fabricated nanopattern with different periods for the AR diffractive waveguide.

The numerical process optimization strategy proposed in **Chapter 3** will be practically useful in modern nanodevices fabrication, which greatly decreases the test number and process turn-around time. The fabrication process and resist coatings can be devised beforehand according to the numerical simulation for the complex substrates, which is adaptable and scalable for the fabrication of diverse nanodevices.

The high-fidelity and clean nanotransfer technique introduced in **Chapter 4** is promising for the fabrication of low-cost and compact nanodevices such as high-

performance micro-spectrometer or flexible nanoelectronics. The reliable pattern transfer makes the nanopatterning unlimited to geometries and materials of substrates, equipment, and environmental conditions. A potential extension of this research is to fabricate re-usable templates using solid electroplating masks, which may be suitable for mass production (Figure 7-3).

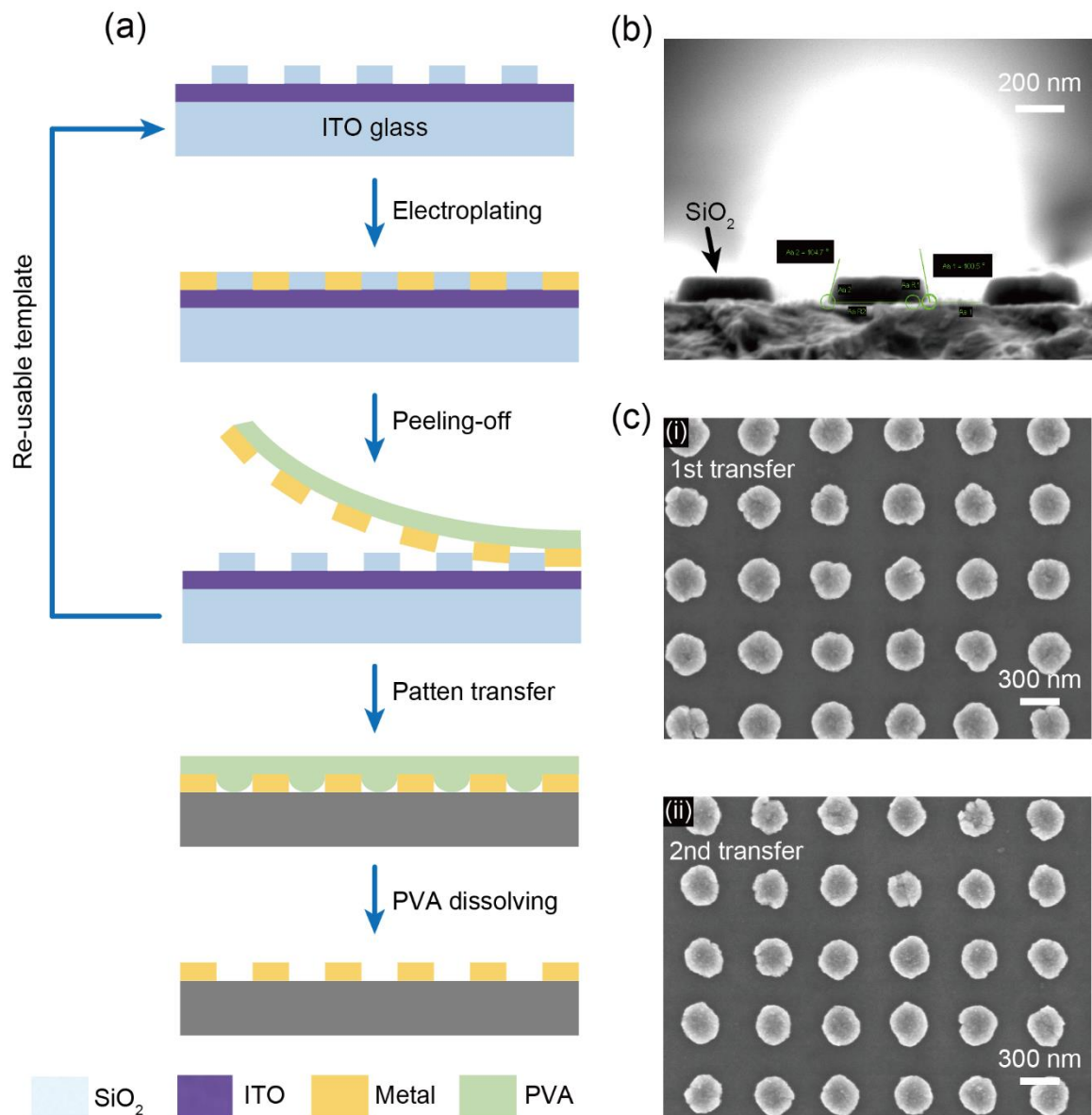


Figure 7-3 (a) Schematic of re-usable template-based nanotransfer lithography. (b) SEM image of the transfer template using SiO₂ nanostructures as masks. (c) SEM images of the transferred Cu nanopillars after (i) 1st and (ii) 2nd transfers.

The IL-GPSE process portfolio proposed in **Chapter 5** has been demonstrated with the strength in large-area uniform nanopatterning and structural color metasurface. But this size modulation approach cannot achieve arbitrary dimension tunability within the period because the secondary exposure deteriorates the interference pattern contrast of the exposure field distribution resulting in poor morphology control, which constrains the pattern diversity. However, it can be still expected that with fancy numerical design, upgraded 2-FOIL system, and other advanced nanotechnologies, the IL-GPSE approach can be applied to more emerging applications such as metalens, metaholograms and vortex beam converters, etc.

Appendix A

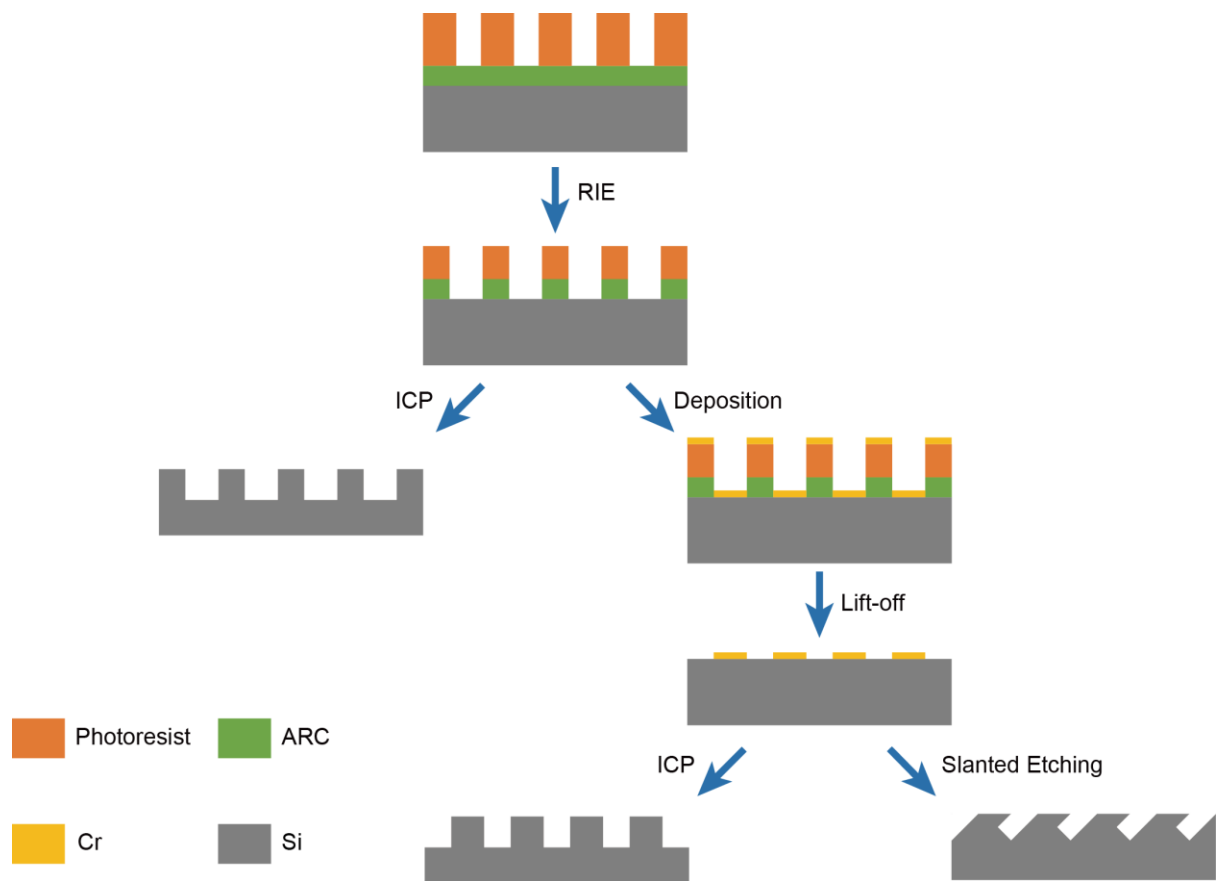


Figure A-1 The schematic illustration of different pattern transfer techniques.

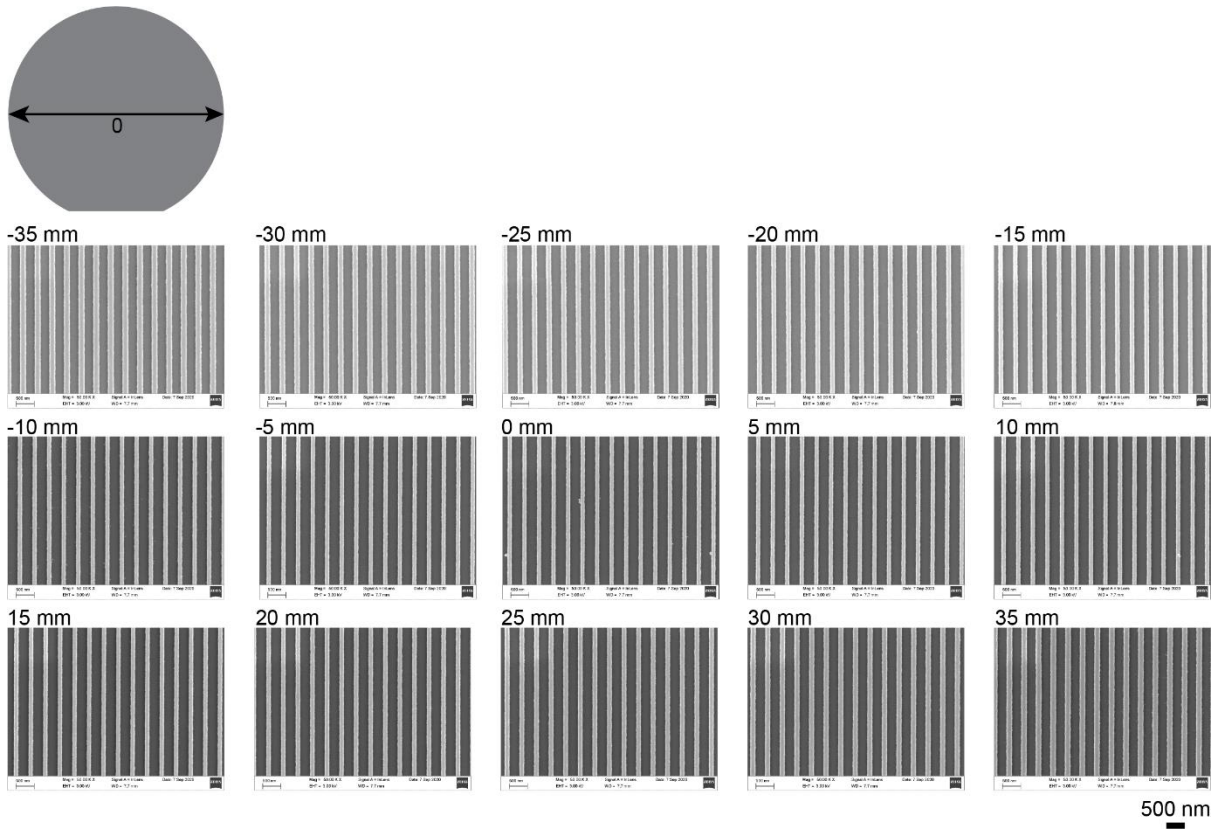


Figure A-2 SEM images recorded every 5 mm along the diameter of the 3-inch wafer patterned by 2-FOIL.

Appendix B

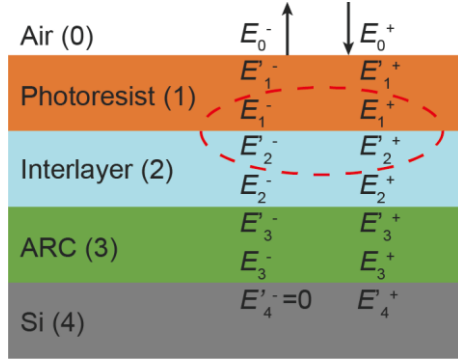


Figure B-1 The illustration of tri-layer structure for TMM analysis

The light transmission and reflection at each interface can be calculated by applying the transfer matrix method to the tri-layer structure. When the light propagates through the multi-layer stack including photoresist, interlayer, ARC, and substrate, the electrical field across the interface ($m-1$ and m layers) can be expressed as,

$$\begin{pmatrix} E_{m-1}^+ \\ E_{m-1}^- \end{pmatrix} = \frac{1}{t_{m-1,m}} \begin{pmatrix} 1 & r_{m,m-1} \\ r_{m,m-1} & 1 \end{pmatrix} \begin{pmatrix} E_m^+ \\ E_m^- \end{pmatrix} = \mathbf{T}_{m-1} \begin{pmatrix} E_m^+ \\ E_m^- \end{pmatrix} \quad (\text{B. 1})$$

where t and r are the refractive and reflective coefficients of TE mode incident light, \mathbf{T} is the transmission matrix. In addition, the electrical field variation in the $m-1$ layer is,

$$\begin{pmatrix} E_{m-1}^+ \\ E_{m-1}^- \end{pmatrix} = \begin{pmatrix} e^{-ikd_{m-1}} & 0 \\ 0 & e^{ikd_{m-1}} \end{pmatrix} \begin{pmatrix} E_{m-1}^+ \\ E_{m-1}^- \end{pmatrix} = \mathbf{P}_{m-1} \begin{pmatrix} E_{m-1}^+ \\ E_{m-1}^- \end{pmatrix} \quad (\text{B. 2})$$

where k is the wave vector, d is the film thickness, and \mathbf{P} is the propagation matrix. Thus, the electrical field change between $m-1$ and m layers can be derived as,

$$\begin{pmatrix} E_{m-1}^+ \\ E_{m-1}^- \end{pmatrix} = \mathbf{P}_{m-1} \mathbf{T}_{m-1} \begin{pmatrix} E_m^+ \\ E_m^- \end{pmatrix} = \mathbf{M}_{m-1} \begin{pmatrix} E_m^+ \\ E_m^- \end{pmatrix} \quad (\text{B. 3})$$

where \mathbf{M} is the transfer matrix. Based on the theoretical model, the electrical field just above the bottom boundary of the photoresist layer can be deduced as,

$$\begin{pmatrix} E_1^+ \\ E_1^- \end{pmatrix} = \frac{1}{t_{12}} \begin{pmatrix} 1 & r_{12} \\ r_{12} & 1 \end{pmatrix} \mathbf{M}_2 \mathbf{M}_3 \begin{pmatrix} E'_4^+ \\ E'_4^- \end{pmatrix} = \begin{pmatrix} \mathbf{M}_{\mathbf{T},11} & \mathbf{M}_{\mathbf{T},12} \\ \mathbf{M}_{\mathbf{T},21} & \mathbf{M}_{\mathbf{T},22} \end{pmatrix} \begin{pmatrix} E'_4^+ \\ E'_4^- \end{pmatrix} = \mathbf{M}_T \begin{pmatrix} E'_4^+ \\ E'_4^- \end{pmatrix} \quad (\text{B. 4})$$

where E'_4^- equals to 0, because we assume that all the residual light is absorbed in Si substrate. Thus, the reflectivity can be defined as the intensity ratio of the backward wave to the forward wave at the photoresist/interlayer boundary,

$$R_{PR, SiO_2} = |r_{PR, SiO_2}|^2 = \left(\frac{E_1^-}{E_1^+} \right)^2 = \left(\frac{\mathbf{M}_{\mathbf{T},21}}{\mathbf{M}_{\mathbf{T},11}} \right)^2 \quad (\text{B. 5})$$

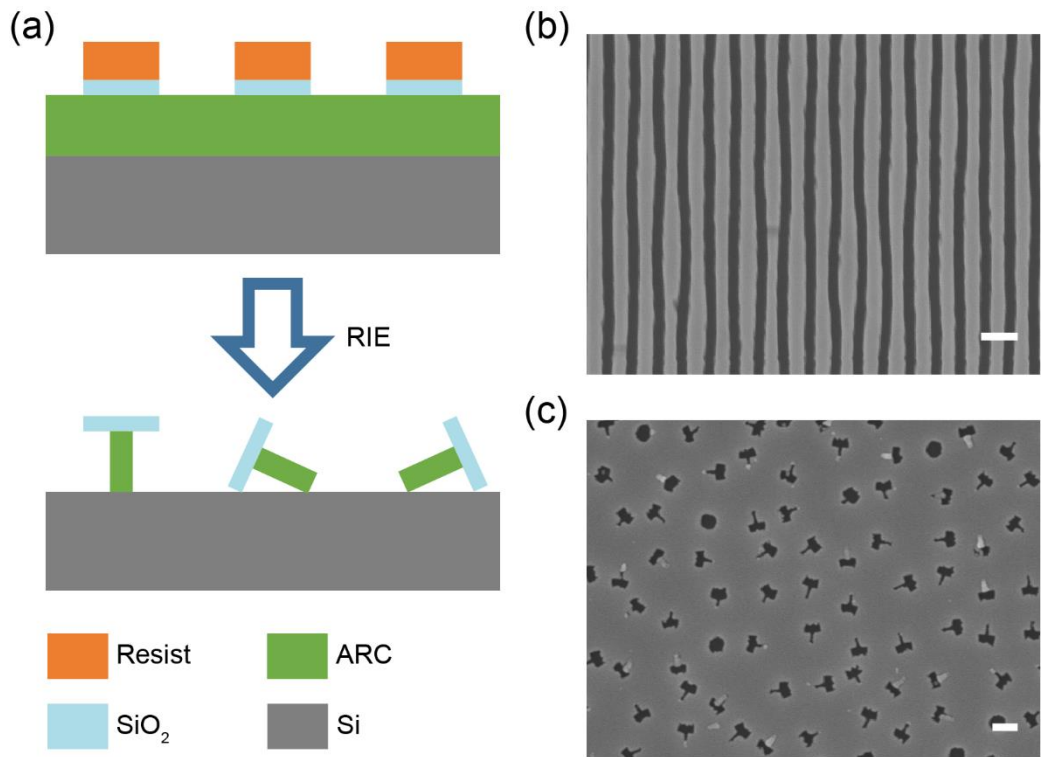


Figure B-2 Collapse of the undercut structure when exposing sub-100-nm pattern using thick ARC. (a) schematic of the collapse happened when etching ARC to form the undercut structure. SEM images of final etched pattern (b) nanogratings and (c) nanopillars in Si when the collapse happened. Scale bars, 200 nm.

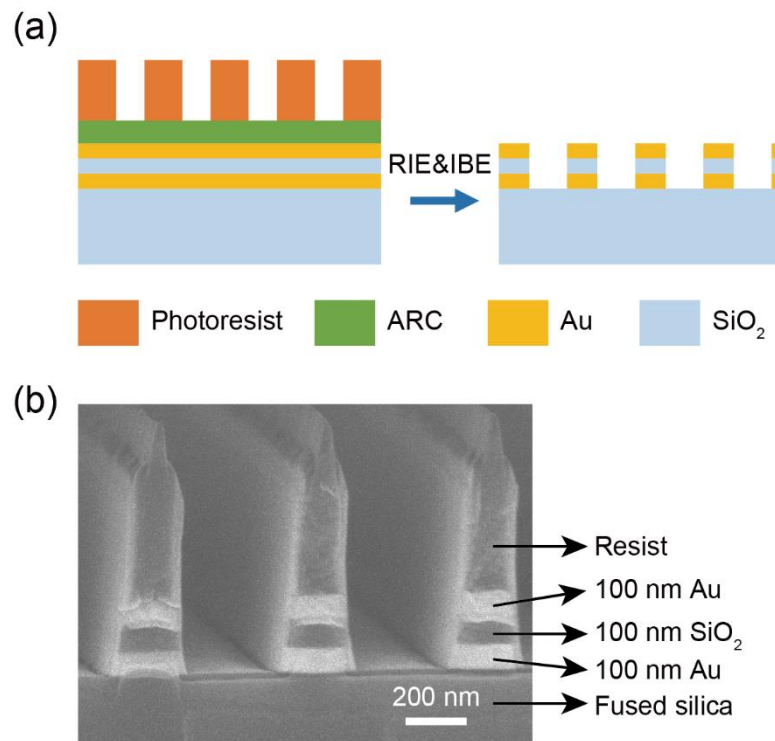


Figure B-3 Fabrication of high-aspect-ratio MIM nanostructures. (a) Schematic of the fabrication of Au-SiO₂-Au nanostructures using RIE and IBE subtractive manufacture. (b) The SEM image of high-aspect-ratio Au-SiO₂-Au nanogratings fabricated by IL, RIE and IBE.

Appendix C

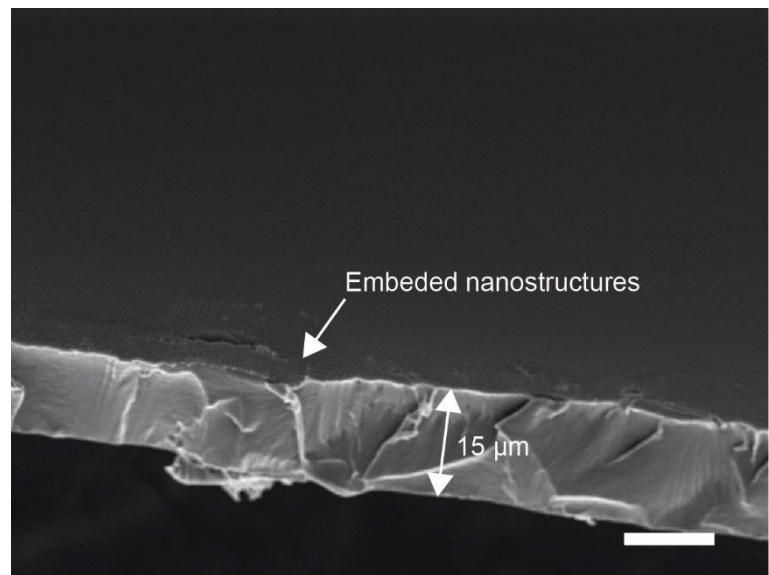


Figure C-1 SEM image of the PVA film with nanostructures embedded. Scale bar, 10 μm .

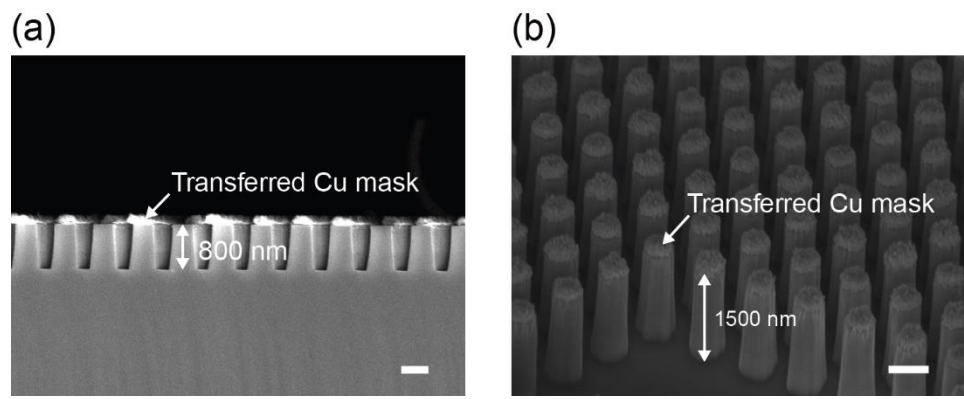


Figure C-2 SEM images of the etched high-aspect-ratio Si nanostructures using transferred Cu pattern as the mask, (a) 800-nm-height nanogratings, (b) 1500-nm-height nanopillars. Scale bars, 500 nm.

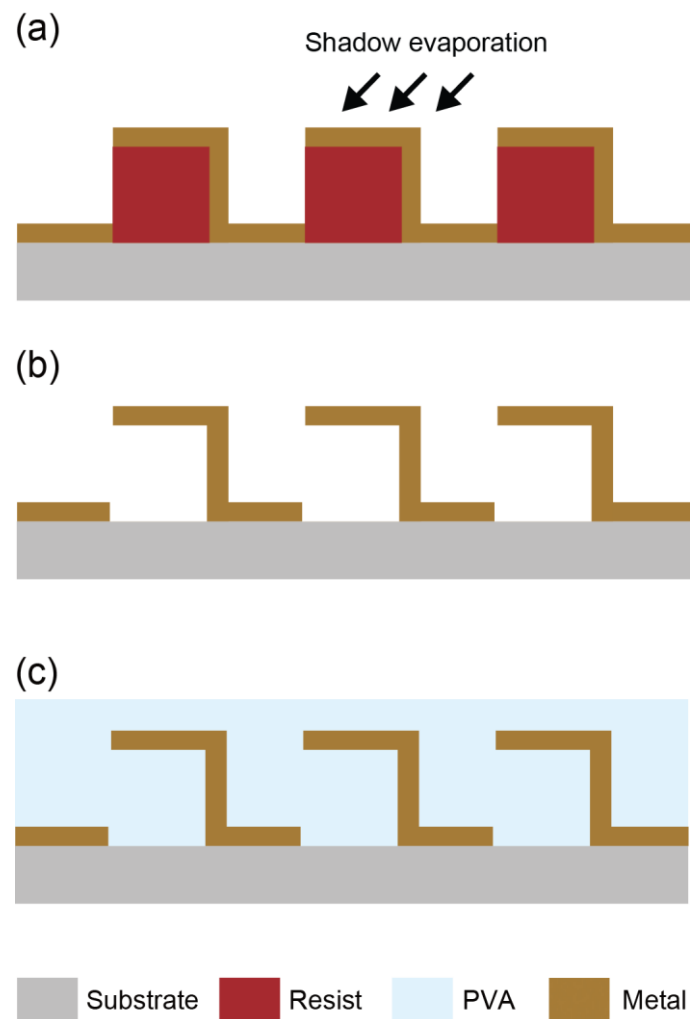


Figure C-3 The schematic process flow of fabricating Z-shaped nanostructures. (a) Shadow evaporation on the resist grating. (b) Dissolving the resist. (c) Spin-casting PVA solution to fill the space among nanostructures.

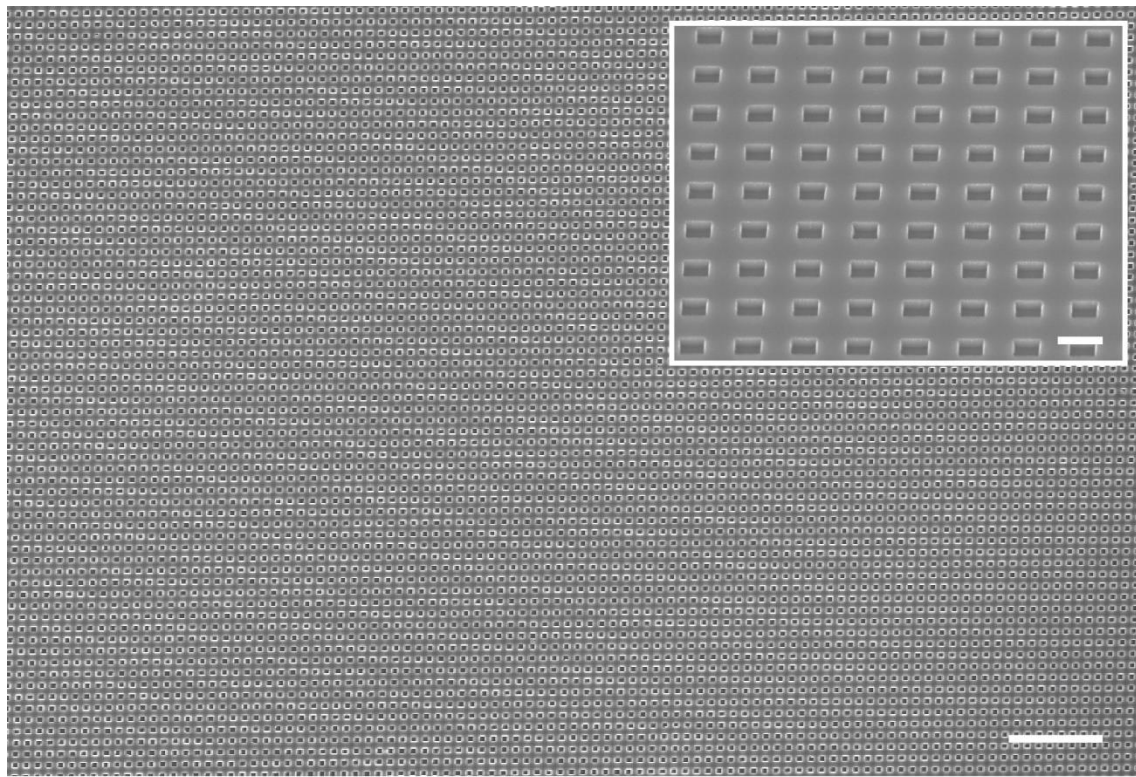


Figure C-4 SEM images of the etched Si square nanohole array using transferred stack-mesh as the mask. Scale bars, 5 μm and 500 nm (inset).

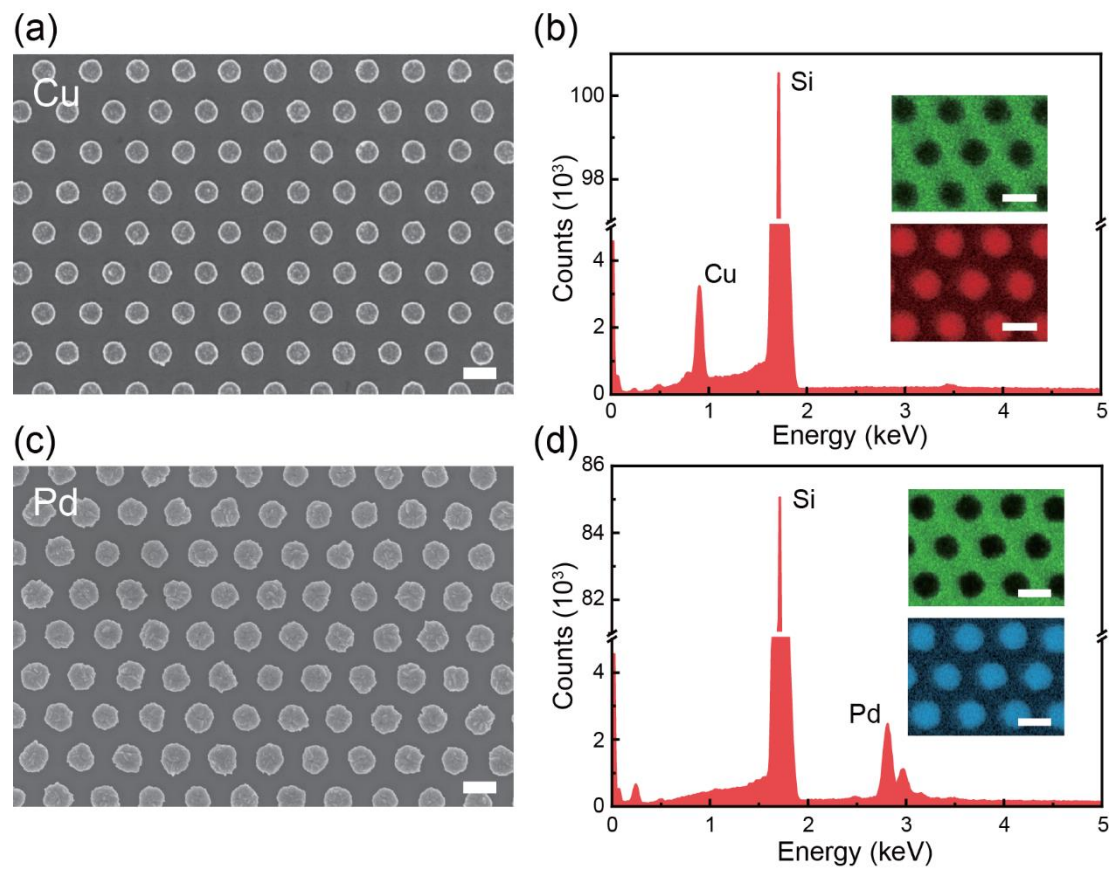


Figure C-5 SEM images and corresponding EDX spectra and mapping of the transferred (a, b) Cu and (c, d) Pd nanodisks on Si. Scale bars, 500 nm.

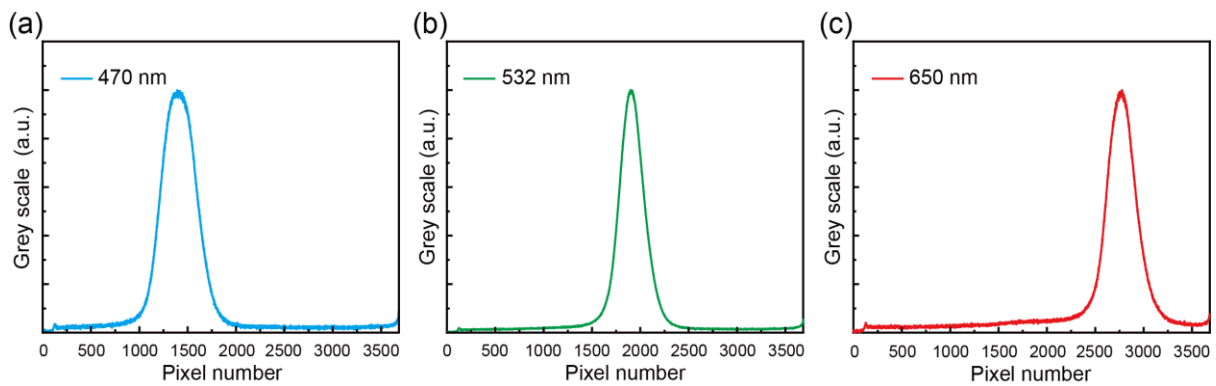


Figure C-6 Spectra for wavelength calibration of (a) 470 nm, (b) 532 nm and (c) 650 nm.

Appendix D

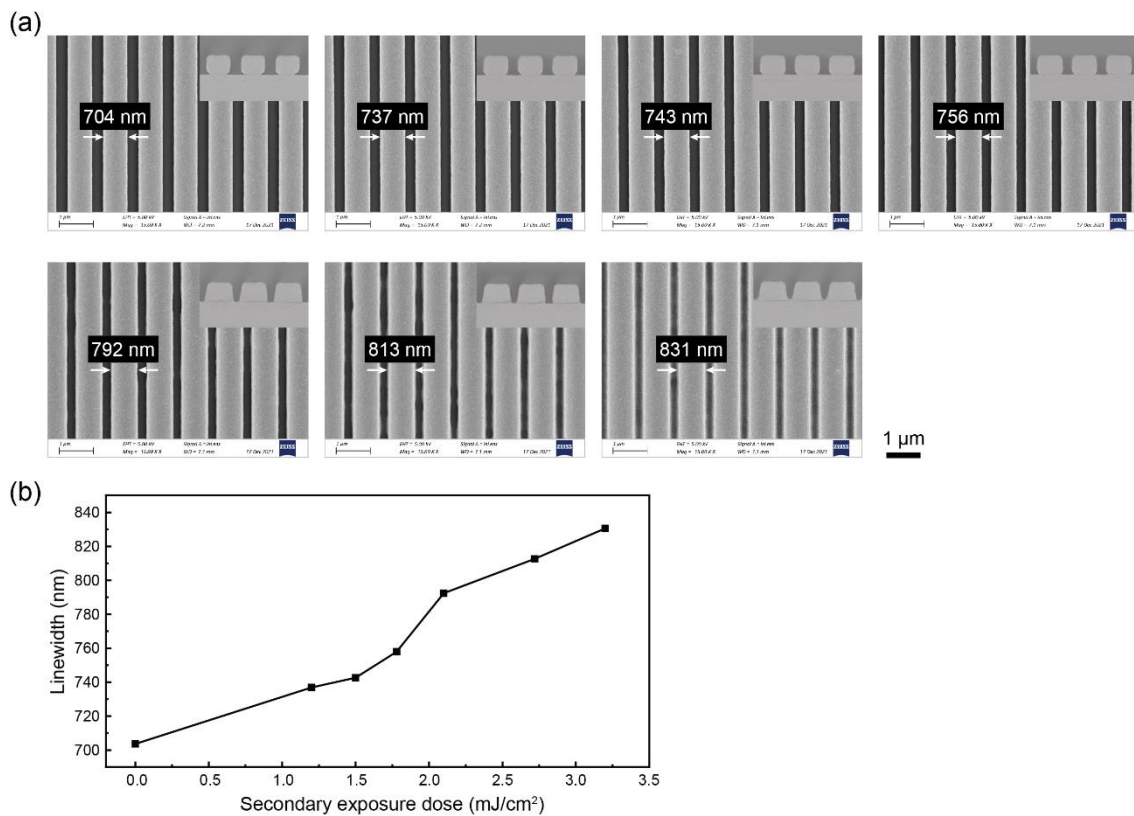


Figure D-1 Negative-tone photoresist test using IL-GPSE. (a) SEM images of 1000-nm-period gratings in negative-tone photoresist patterned by IL-GPSE process. (b) The measured linewidths showing a positive correlation to secondary exposure dose.

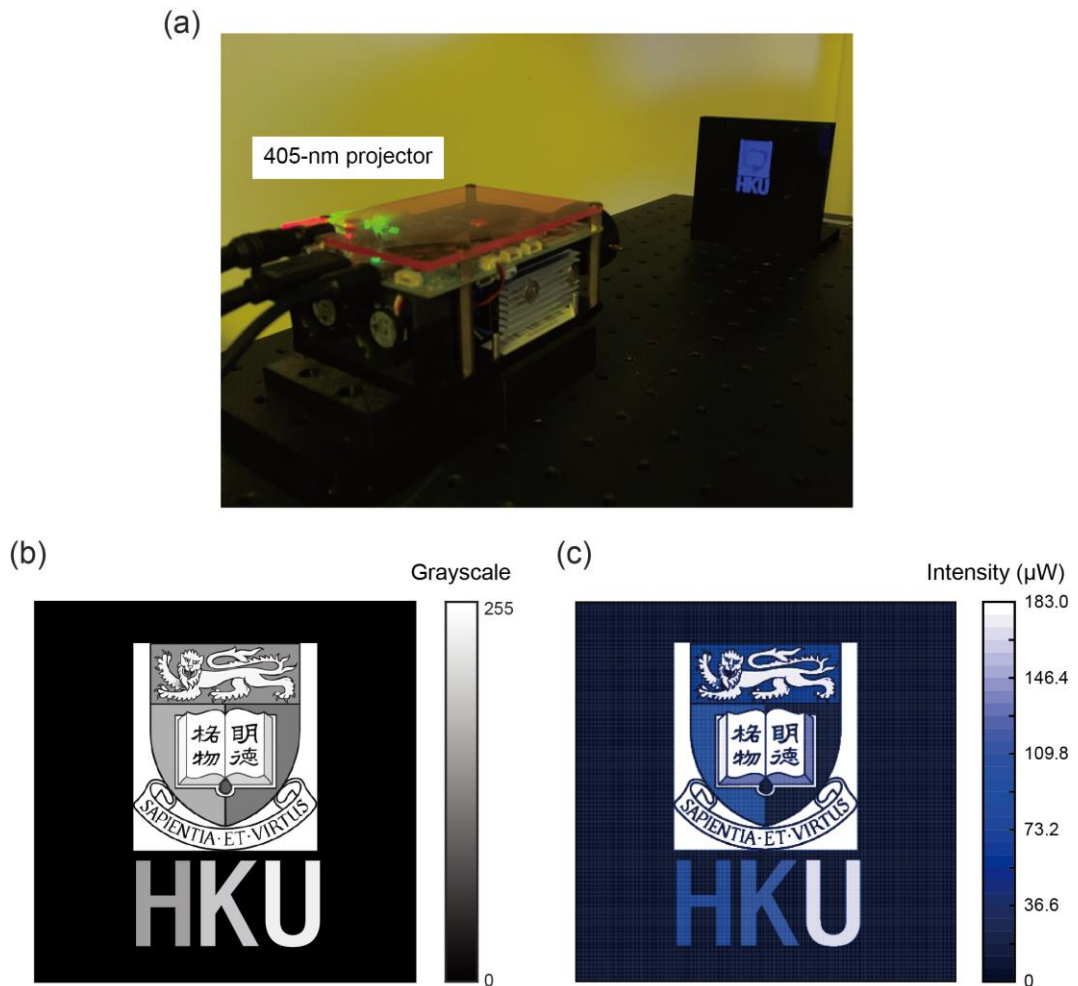


Figure D-2 IL-GPSE method using UV projection lithography. (a) Setup of the UV projection for secondary exposure with a digital grayscale image. (b) Digital grayscale image for the UV projection to generate a patterned UV intensity distribution. (c) The intensity distribution converted from (b) for secondary exposure.

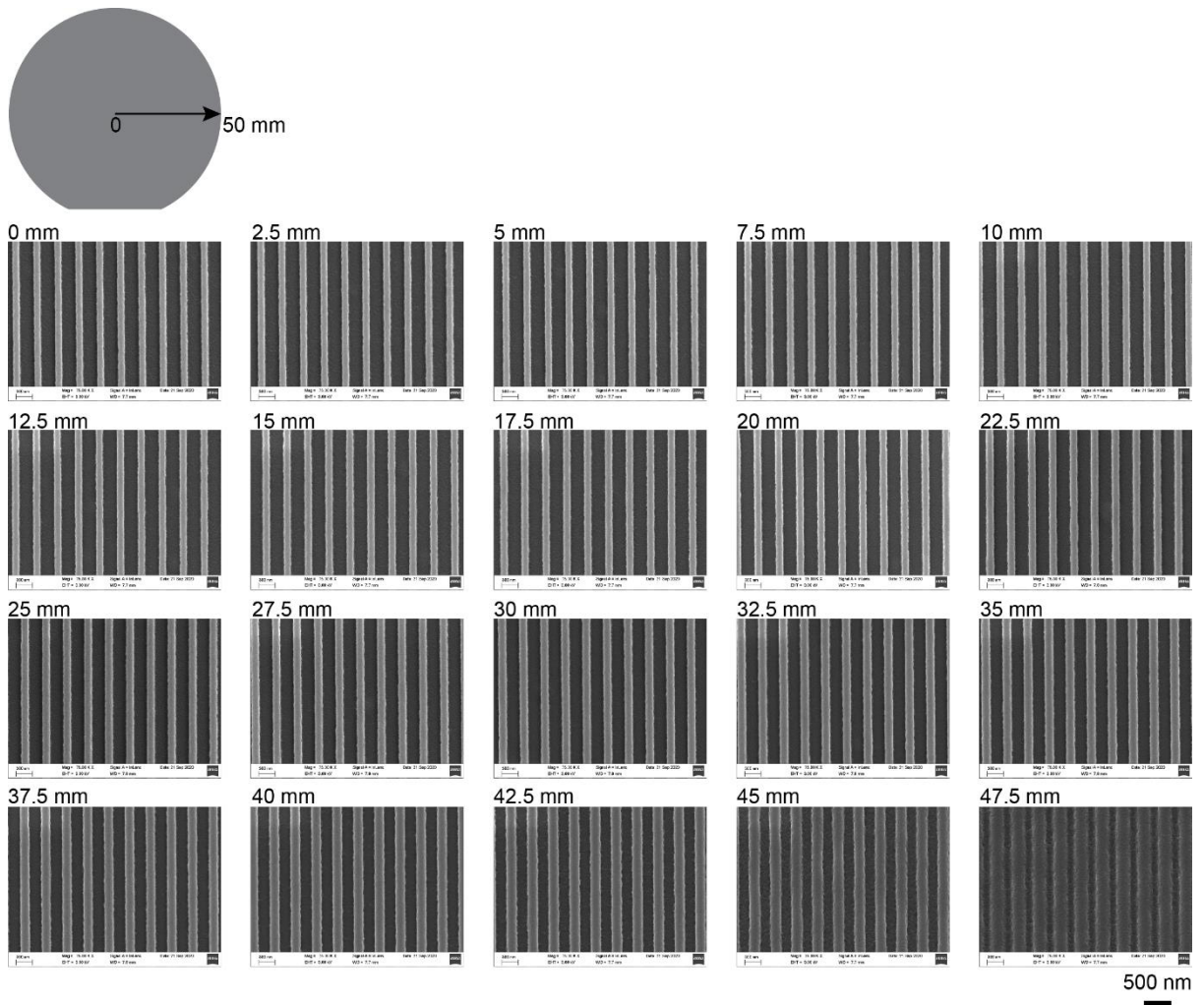


Figure D-3 SEM images recorded every 2.5 mm along the radius of the 4-inch wafer patterned only by interference lithography.

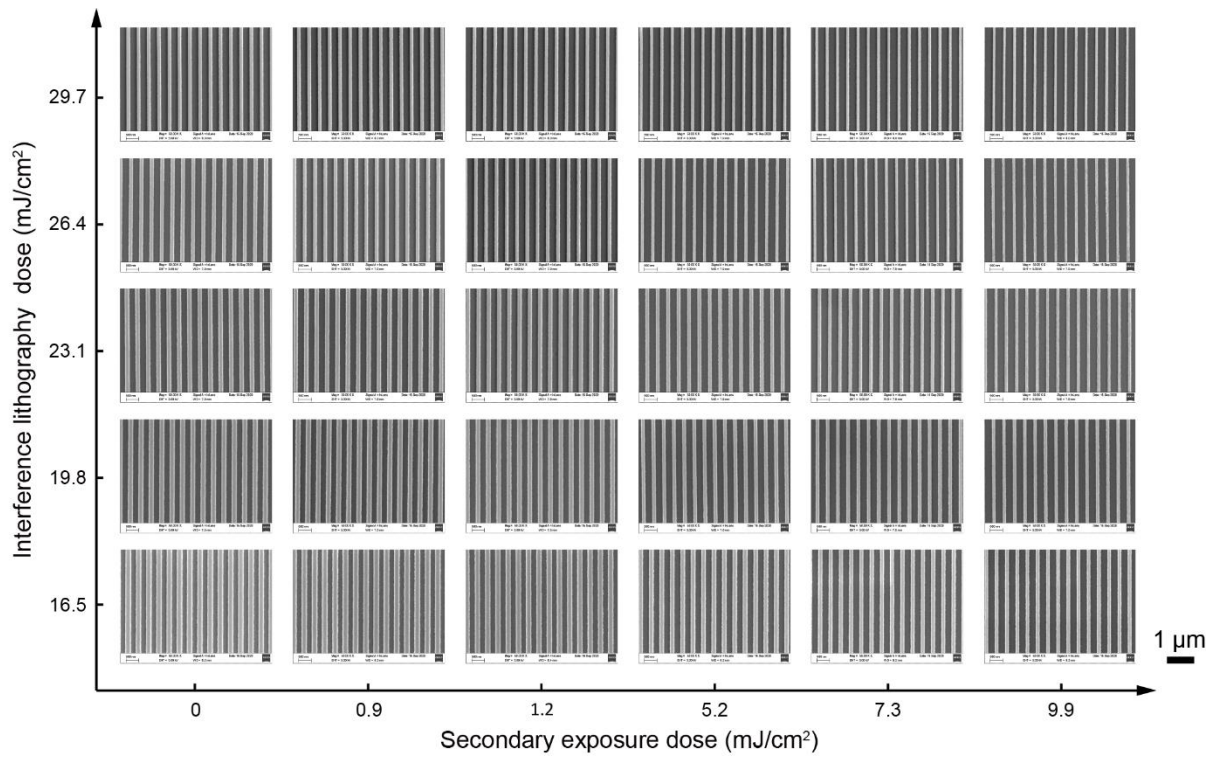


Figure D-4 SEM image matrix of 400-nm-period gratings exposed by different combinations of interference lithography and secondary exposure doses.

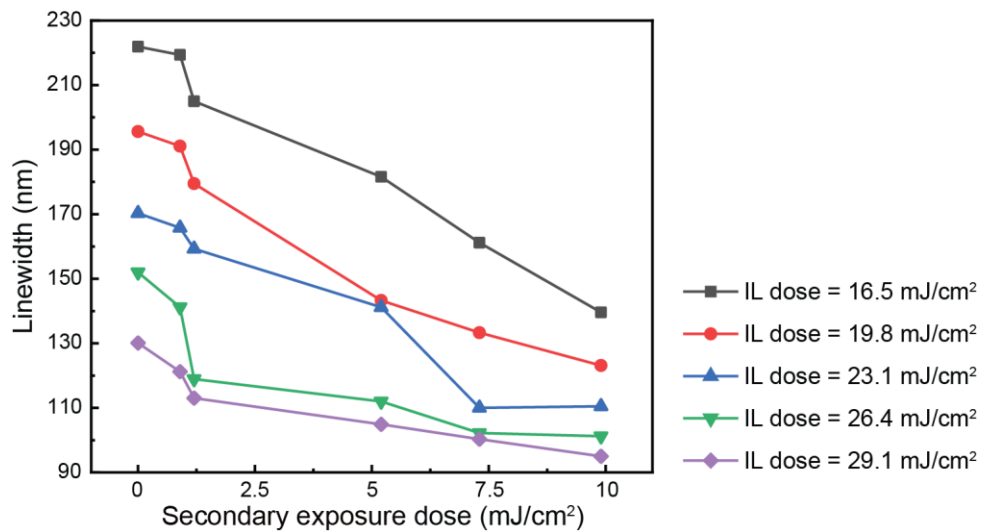


Figure D-5 The linewidths measured in the SEM images of Figure D-4.

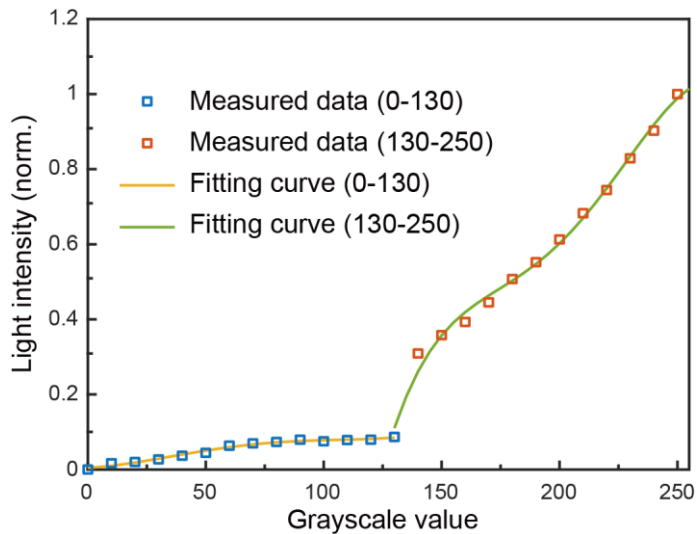


Figure D-6 The relationship between digital grayscale value and normalized projected light intensity using the UV projector.

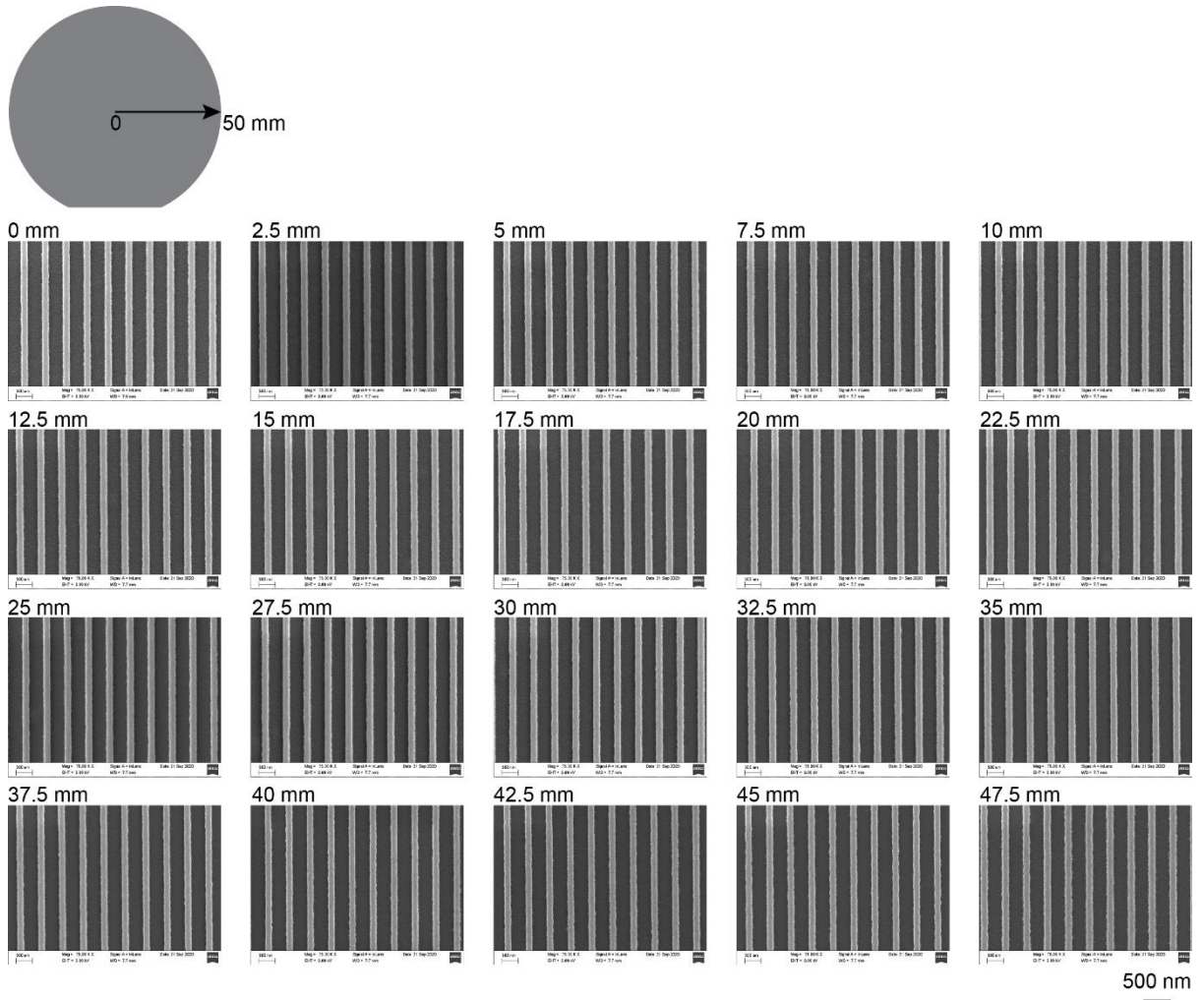


Figure D-7 SEM images recorded every 2.5 mm along the radius of the 4-inch wafer patterned by IL and grayscale-patterned secondary exposure.

Appendix E

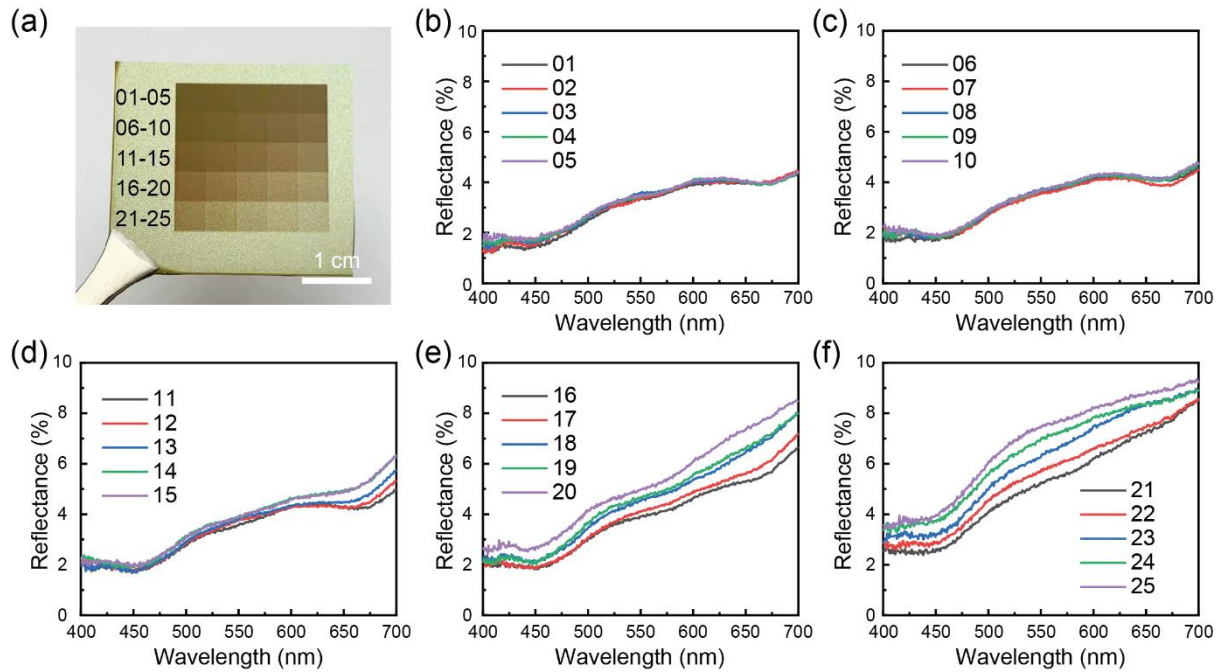


Figure E-1 (a) The photograph of 25 squares of 700-nm-period 2D patterns on photoresist modulated by secondary exposure projection, showing a clear grayscale change from dark brown to light gold. (b-f) Measured reflection spectra on each square.

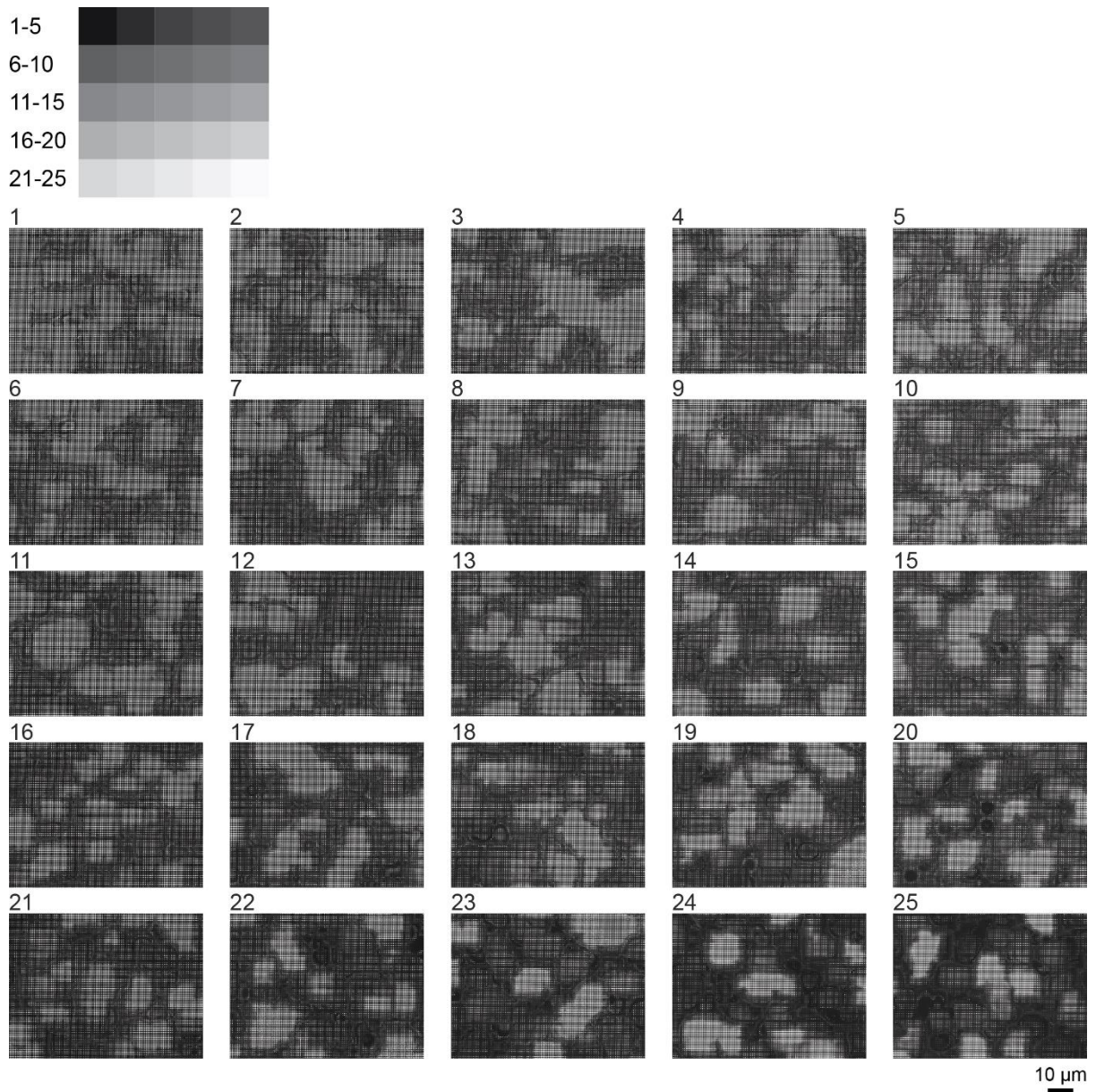


Figure E-2 SEM images of all 25 areas in Figure 6-3a patterned by different secondary exposure doses.

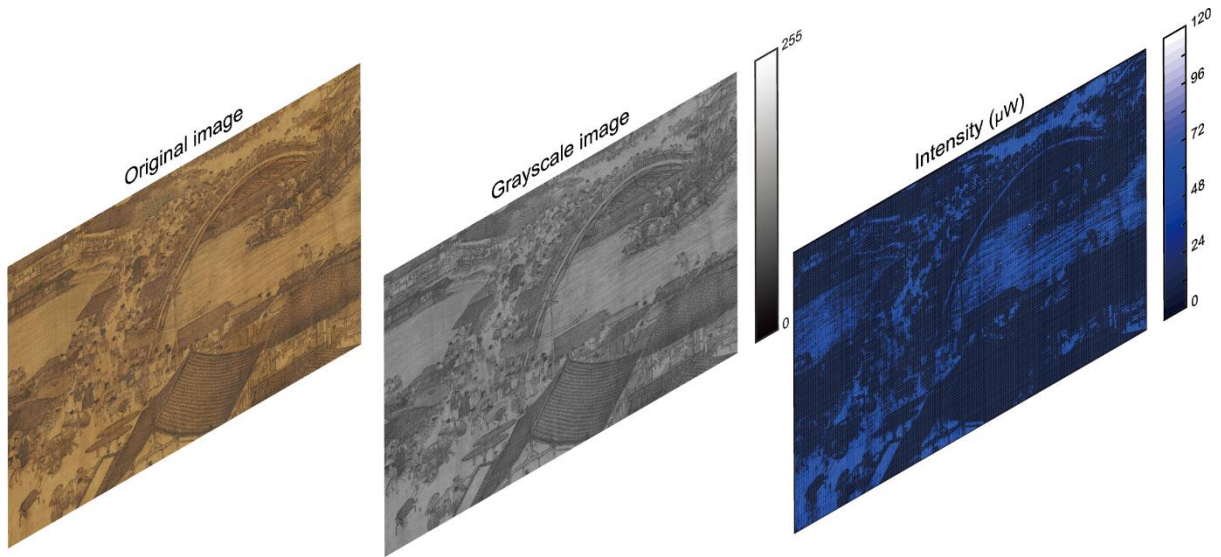


Figure E-3 Pixel-by-pixel mapping of an image into grayscale and intensity channels.

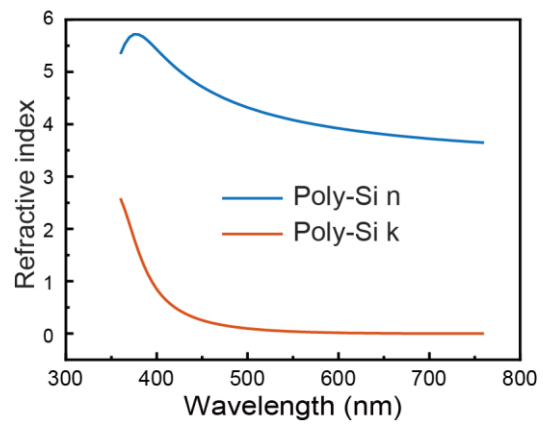


Figure E-4 Results of measured refractive index n and extinction coefficient k versus wavelength for polysilicon deposited by LPCVD.

References

- 1 Feynman, R. P. There's plenty of room at the bottom [data storage]. *Journal of microelectromechanical systems* **1**, 60-66 (1992).
- 2 Broers, A., Molzen, W., Cuomo, J. & Wittels, N. Electron-beam fabrication of 80-Å metal structures. *Applied Physics Letters* **29**, 596-598 (1976).
- 3 Pease, R. Electron beam lithography. *Contemporary Physics* **22**, 265-290 (1981).
- 4 Grigorescu, A. & Hagen, C. Resists for sub-20-nm electron beam lithography with a focus on HSQ: state of the art. *Nanotechnology* **20**, 292001 (2009).
- 5 Kurihara, K. A focused ion beam system for submicron lithography. *Journal of Vacuum Science & Technology B* **3**, 41-44 (1985).
- 6 Tseng, A. A. Recent developments in nanofabrication using focused ion beams. *Small* **1**, 924-939 (2005).
- 7 Li, W.-D., Wu, W. & Stanley Williams, R. Combined helium ion beam and nanoimprint lithography attains 4 nm half-pitch dense patterns. *Journal of Vacuum Science & Technology B* **30**, 06F304 (2012).
- 8 Von Gutfeld, R. & Chaudhari, P. Laser writing and erasing on chalcogenide films. *Journal of Applied Physics* **43**, 4688-4693 (1972).
- 9 Selimis, A., Mironov, V. & Farsari, M. Direct laser writing: Principles and materials for scaffold 3D printing. *Microelectronic Engineering* **132**, 83-89 (2015).
- 10 Finders, J. *et al.* in *Optical Microlithography XIII*. 192-205 (SPIE).
- 11 Nakao, S. *et al.* in *Optical Microlithography XIII*. 358-365 (SPIE).
- 12 Vandenberghe, G. *et al.* in *Optical Microlithography XIV*. 179-190 (SPIE).
- 13 Pirati, A. *et al.* EUV lithography performance for manufacturing: status and outlook. *Extreme Ultraviolet Lithography VII* **9776**, 78-92 (2016).

- 14 Kim, S.-S. *et al.* in *Extreme Ultraviolet (EUV) Lithography VIII*. 1014306 (SPIE).
- 15 Levinson, H. J. & Brunner, T. A. in *International Conference on Extreme Ultraviolet Lithography 2018*. 5-11 (SPIE).
- 16 Chou, S. Y., Krauss, P. R. & Renstrom, P. J. Imprint of sub-25 nm vias and trenches in polymers. *Applied Physics Letters* **67**, 3114-3116 (1995).
- 17 Chou, S. Y., Krauss, P. R. & Renstrom, P. J. J. S. Imprint lithography with 25-nanometer resolution. *Science* **272**, 85-87 (1996).
- 18 Austin, M. D. *et al.* Fabrication of 5 nm linewidth and 14 nm pitch features by nanoimprint lithography. *Applied Physics Letters* **84**, 5299-5301 (2004).
- 19 Ahn, S. H. & Guo, L. J. High-speed roll-to-roll nanoimprint lithography on flexible plastic substrates. *Advanced Materials* **20**, 2044-2049 (2008).
- 20 Ahn, S. H. & Guo, L. J. Large-area roll-to-roll and roll-to-plate nanoimprint lithography: a step toward high-throughput application of continuous nanoimprinting. *ACS Nano* **3**, 2304-2310 (2009).
- 21 Cho, Y. *et al.* Development of large area nano imprint technology by step and repeat process and pattern stitching technique. *Microelectronic Engineering* **86**, 2417-2422 (2009).
- 22 Peroz, C. *et al.* Single digit nanofabrication by step-and-repeat nanoimprint lithography. *Nanotechnology* **23**, 015305 (2011).
- 23 Black, C. T. Polymer self-assembly as a novel extension to optical lithography. *Acs Nano* **1**, 147-150 (2007).
- 24 Cheng, J. Y. *et al.* Simple and versatile methods to integrate directed self-assembly with optical lithography using a polarity-switched photoresist. *ACS Nano* **4**, 4815-4823 (2010).

- 25 Hulteen, J. C. & Van Duyne, R. P. Nanosphere lithography: A materials general fabrication process for periodic particle array surfaces. *Journal of Vacuum Science & Technology A* **13**, 1553-1558 (1995).
- 26 Cheung, C. L., Nikolić, R., Reinhardt, C. & Wang, T. Fabrication of nanopillars by nanosphere lithography. *Nanotechnology* **17**, 1339 (2006).
- 27 Byun, I. & Kim, J. Cost-effective laser interference lithography using a 405 nm AlInGaN semiconductor laser. *Journal of Micromechanics & Microengineering* **20**, 055024 (2010).
- 28 Farhoud, M. *et al.* Fabrication of 200 nm period nanomagnet arrays using interference lithography and a negative resist. *Journal of Vacuum Science & Technology B* **17**, 3182-3185 (1999).
- 29 Liang, C. W. *et al.* Wafer-scale nanopatterning using fast-reconfigurable and actively-stabilized two-beam fiber-optic interference lithography. *Optics Express* **26**, 8194-8200 (2018).
- 30 Feng, J. *et al.* Single-crystalline layered metal-halide perovskite nanowires for ultrasensitive photodetectors. *Nature Electronics* **1**, 404-410 (2018).
- 31 Xu, T. *et al.* Structural colors: from plasmonic to carbon nanostructures. *Small* **7**, 3128-3136 (2011).
- 32 Lee, K.-T., Seo, S., Yong Lee, J. & Jay Guo, L. Ultrathin metal-semiconductor-metal resonator for angle invariant visible band transmission filters. *Applied Physics Letters* **104**, 231112 (2014).
- 33 Adato, R. *et al.* Ultra-sensitive vibrational spectroscopy of protein monolayers with plasmonic nanoantenna arrays. *Proceedings of the National Academy of Sciences* **106**, 19227-19232 (2009).

- 34 Balaur, E. *et al.* Colorimetric histology using plasmonically active microscope slides. *Nature* **598**, 65-71 (2021).
- 35 Yu, Y. F. *et al.* High-transmission dielectric metasurface with 2π phase control at visible wavelengths. *Laser & Photonics Reviews* **9**, 412-418 (2015).
- 36 Arbabi, E. *et al.* MEMS-tunable dielectric metasurface lens. *Nature Communications* **9**, 1-9 (2018).
- 37 Yoon, G. *et al.* Printable nanocomposite metalens for high-contrast near-infrared imaging. *ACS Nano* **15**, 698-706 (2021).
- 38 Li, H. *et al.* Breathable and Skin-Conformal Electronics with Hybrid Integration of Microfabricated Multifunctional Sensors and Kirigami-Structured Nanofibrous Substrates. *Advanced Functional Materials*, 2202792 (2022).
- 39 Seo, M.-H. *et al.* Material-independent nanotransfer onto a flexible substrate using mechanical-interlocking structure. *ACS Nano* **12**, 4387-4397 (2018).
- 40 Rao, Z. *et al.* Curvy, shape-adaptive imagers based on printed optoelectronic pixels with a kirigami design. *Nature Electronics* **4**, 513-521 (2021).
- 41 Wu, M. *et al.* Ultrasensitive Molecular Detection at Subpicomolar Concentrations by the Diffraction Pattern Imaging with Plasmonic Metasurfaces and Convex Holographic Gratings. *Advanced Science*, 2201682 (2022).
- 42 Yang, J. *et al.* Photonic crystal fiber metalens. *Nanophotonics* **8**, 443-449 (2019).
- 43 Hadibrata, W., Wei, H., Krishnaswamy, S. & Aydin, K. Inverse design and 3D printing of a metalens on an optical fiber tip for direct laser lithography. *Nano Letters* **21**, 2422-2428 (2021).
- 44 Tseng, M. L. *et al.* Metalenses: advances and applications. *Advanced Optical Materials* **6**, 1800554 (2018).

- 45 Khorasaninejad, M. *et al.* Metalenses at visible wavelengths: Diffraction-limited focusing and subwavelength resolution imaging. *Science* **352**, 1190-1194 (2016).
- 46 Walther, B. *et al.* Spatial and spectral light shaping with metamaterials. *Advanced Materials* **24**, 6300-6304 (2012).
- 47 Zhao, R. *et al.* Controllable Polarization and Diffraction Modulated Multi-Functionality Based on Metasurface. *Advanced Optical Materials* **10**, 2102596 (2022).
- 48 Huo, P. *et al.* Photorealistic full-color nanopainting enabled by a low-loss metasurface. **7**, 1171-1172 (2020).
- 49 Kumar, K. *et al.* Printing colour at the optical diffraction limit. *Nature Nanotechnology* **7**, 557-561 (2012).
- 50 Lee, G.-Y. *et al.* Metasurface eyepiece for augmented reality. *Nature Communications* **9**, 1-10 (2018).
- 51 Lan, S. *et al.* Metasurfaces for near-eye augmented reality. *ACS Photonics* **6**, 864-870 (2019).
- 52 Xiong, J., Hsiang, E.-L., He, Z., Zhan, T. & Wu, S.-T. Augmented reality and virtual reality displays: emerging technologies and future perspectives. *Light: Science & Applications* **10**, 1-30 (2021).
- 53 Cai, J. *et al.* Highly-facile template-based selective electroless metallization of micro-and nanopatterns for plastic electronics and plasmonics. *Journal of Materials Chemistry C* **7**, 4363-4373 (2019).
- 54 Cai, J. *et al.* Solution-Processed Large-Area Gold Nanocheckerboard Metasurfaces on Flexible Plastics for Plasmonic Biomolecular Sensing. *Advanced Optical Materials*, 1900516 (2019).

- 55 Chen, L. *et al.* Nanostructured texturing of CH₃NH₃PbI₃ perovskite thin film on flexible substrate for photodetector application. *Organic Electronics* **71**, 284-289 (2019).
- 56 Savas, T., Schattenburg, M., Carter, J. & Smith, H. I. Large-area achromatic interferometric lithography for 100 nm period gratings and grids. *Journal of Vacuum Science & Technology B* **14**, 4167-4170 (1996).
- 57 Mukherjee, P. *et al.* Plasma etch fabrication of 60: 1 aspect ratio silicon nanogratings with 200 nm pitch. *Journal of Vacuum Science & Technology B* **28**, C6P70-C76P75 (2010).
- 58 Solak, H. H. *et al.* Sub-50 nm period patterns with EUV interference lithography. *Microelectronic Engineering* **67**, 56-62 (2003).
- 59 Golovkina, V. *et al.* Exploring the ultimate resolution of positive-tone chemically amplified resists: 26 nm dense lines using extreme ultraviolet interference lithography. *Journal of Vacuum Science & Technology B* **22**, 99-103 (2004).
- 60 Sun, Y.-L., Mikolas, D., Chang, E.-C., Lin, P.-T. & Fu, C.-C. Lloyd's mirror interferometer using a single-mode fiber spatial filter. *Journal of Vacuum Science & Technology B* **31**, 021604 (2013).
- 61 Hung, Y.-J., Chang, P.-C., Lin, Y.-N. & Lin, J.-J. Compact mirror-tunable laser interference system for wafer-scale patterning of grating structures with flexible periodicity. *Journal of Vacuum Science & Technology B* **34**, 040609 (2016).
- 62 Solak, H., David, C., Gobrecht, J., Wang, L. & Cerrina, F. Multiple-beam interference lithography with electron beam written gratings. *Journal of Vacuum Science & Technology B* **20**, 2844-2848 (2002).
- 63 Zaidi, S. H. & Brueck, S. R. High aspect-ratio holographic photoresist gratings. *Applied Optics* **27**, 2999-3002 (1988).

- 64 Bai, S. Nanophotonic devices, applications and fabrication by nanoimprint lithography. *PhD Thesis* (2007).
- 65 Dill, F. H., Hornberger, W. P., Hauge, P. S. & Shaw, J. M. Characterization of positive photoresist. *IEEE Transactions on electron devices* **22**, 445-452 (1975).
- 66 Babu, S. & Barouch, E. Exact solution of Dill's model equations for positive photoresist kinetics. *IEEE Electron Device Letters* **7**, 252-253 (1986).
- 67 Mello, B. d. A., da Costa, I. F., Lima, C. R. & Cescato, L. Developed profile of holographically exposed photoresist gratings. *Applied Optics* **34**, 597-603 (1995).
- 68 Chou, S. Y., Krauss, P. R. & Renstrom, P. J. Nanoimprint lithography. *Journal of Vacuum Science & Technology B* **14**, 4129-4133 (1996).
- 69 Guo, L. J. Nanoimprint lithography: methods and material requirements. *Advanced Materials* **19**, 495-513 (2007).
- 70 Lin, T.-H., Yang, Y.-K. & Fu, C.-C. Integration of multiple theories for the simulation of laser interference lithography processes. *Nanotechnology* **28**, 475301 (2017).
- 71 Fan, Y. *et al.* in *Optical Microlithography XVIII*. 1805-1816 (SPIE).
- 72 Mack, C. A. Analytical expression for the standing wave intensity in photoresist. *Applied Optics* **25**, 1958-1961 (1986).
- 73 Jeon, T. Y., Park, S. G., Kim, D. H. & Kim, S. H. Standing-wave-assisted creation of nanopillar arrays with vertically integrated nanogaps for SERS-active substrates. *Advanced Functional Materials* **25**, 4681-4688 (2015).
- 74 Schattenburg, M., Aucoin, R. & Fleming, R. Optically matched trilevel resist process for nanostructure fabrication. *Journal of Vacuum Science & Technology B* **13**, 3007-3011 (1995).

- 75 Min, S. *et al.* Ultrasensitive Molecular Detection by Imaging of Centimeter-Scale Metasurfaces with a Deterministic Gradient Geometry. *Advanced Materials* **33**, 2100270 (2021).
- 76 <https://refractiveindex.info/>.
- 77 Hosseini, A. & Massoud, Y. A low-loss metal-insulator-metal plasmonic bragg reflector. *Optics Express* **14**, 11318-11323 (2006).
- 78 Zhang, J. *et al.* Electrical tuning of metal-insulator-metal metasurface with electro-optic polymer. **113**, 231102 (2018).
- 79 Dorodnyy, A., Koepfli, S. M., Lochbaum, A. & Leuthold, J. Design of CMOS-compatible metal–insulator–metal metasurfaces via extended equivalent-circuit analysis. *Scientific Reports* **10**, 1-12 (2020).
- 80 Al Mahmud, M. J., Hyder, R. & Islam, M. Z. A highly sensitive metal–insulator–metal ring resonator-based nanophotonic structure for biosensing applications. *IEEE Sensors Journal* **18**, 6563-6568 (2018).
- 81 Baffou, G. & Quidant, R. Thermo-plasmonics: using metallic nanostructures as nano-sources of heat. *Laser & Photonics Reviews* **7**, 171-187 (2013).
- 82 Bouillard, J.-S. G., Dickson, W., O'Connor, D. P., Wurtz, G. A. & Zayats, A. V. Low-temperature plasmonics of metallic nanostructures. *Nano Letters* **12**, 1561-1565 (2012).
- 83 Khan, A. *et al.* High-performance flexible transparent electrode with an embedded metal mesh fabricated by cost-effective solution process. *Small* **12**, 3021-3030 (2016).
- 84 Didiot, C., Pons, S., Kierren, B., Fagot-Revurat, Y. & Malterre, D. Nanopatterning the electronic properties of gold surfaces with self-organized superlattices of metallic nanostructures. *Nature Nanotechnology* **2**, 617-621 (2007).

- 85 Lee, K.-L., Wu, T.-Y., Hsu, H.-Y., Yang, S.-Y. & Wei, P.-K. Low-cost and rapid fabrication of metallic nanostructures for sensitive biosensors using hot-embossing and dielectric-heating nanoimprint methods. *Sensors* **17**, 1548 (2017).
- 86 Valsecchi, C. & Brolo, A. G. Periodic metallic nanostructures as plasmonic chemical sensors. *Langmuir* **29**, 5638-5649 (2013).
- 87 Chen, Y. *et al.* Reliable Patterning, Transfer Printing and Post-Assembly of Multiscale Adhesion-Free Metallic Structures for Nanogap Device Applications. *Advanced Functional Materials* **30**, 2002549 (2020).
- 88 Meitl, M. A. *et al.* Transfer printing by kinetic control of adhesion to an elastomeric stamp. *Nature Materials* **5**, 33-38 (2006).
- 89 Schaper, C. D. Patterned transfer of metallic thin film nanostructures by water-soluble polymer templates. *Nano Letters* **3**, 1305-1309 (2003).
- 90 Chanda, D. *et al.* Large-area flexible 3D optical negative index metamaterial formed by nanotransfer printing. *Nature Nanotechnology* **6**, 402-407 (2011).
- 91 Li, Z. *et al.* Efficient strain modulation of 2D materials via polymer encapsulation. *Nature communications* **11**, 1-8 (2020).
- 92 Park, T. W. *et al.* Thermally assisted nanotransfer printing with sub-20-nm resolution and 8-inch wafer scalability. *Science Advances* **6**, eabb6462 (2020).
- 93 Tiefenauer, R. F., Tybrandt, K., Aramesh, M. & Voros, J. Fast and versatile multiscale patterning by combining template-stripping with nanotransfer printing. *ACS Nano* **12**, 2514-2520 (2018).
- 94 Hwang, S. H. *et al.* Covalent bonding-assisted nanotransfer lithography for the fabrication of plasmonic nano-optical elements. *Nanoscale* **9**, 14335-14346 (2017).
- 95 Hwang, S. H. *et al.* Repeatable and metal-independent nanotransfer printing based on metal oxidation for plasmonic color filters. *Nanoscale* **11**, 11128-11137 (2019).

- 96 Ko, J. *et al.* Nanotransfer printing on textile substrate with water-soluble polymer nanotemplate. *ACS Nano* **14**, 2191-2201 (2020).
- 97 Zhao, Z.-J. *et al.* Adhesive-layer-free and double-faced nanotransfer lithography for a flexible large-area metasurface hologram. *ACS Applied Materials & Interfaces* **12**, 1737-1745 (2019).
- 98 Liu, J. *et al.* Sacrificial layer-assisted nanoscale transfer printing. *Microsystems & nanoengineering* **6**, 1-10 (2020).
- 99 Zhang, C., Cai, J., Liang, C., Khan, A. & Li, W. D. Scalable fabrication of metallic nanofiber network via templated electrodeposition for flexible electronics. *Advanced Functional Materials* **29**, 1903123 (2019).
- 100 Khan, A. *et al.* Template-Electrodeposited and Imprint-Transferred Microscale Metal-Mesh Transparent Electrodes for Flexible and Stretchable Electronics. *Advanced Engineering Materials* **21**, 1900723 (2019).
- 101 Diaz, A. & Felix-Navarro, R. A semi-quantitative tribo-electric series for polymeric materials: the influence of chemical structure and properties. *Journal of Electrostatics* **62**, 277-290 (2004).
- 102 Zou, H. *et al.* Quantifying the triboelectric series. *Nature communications* **10**, 1-9 (2019).
- 103 Zou, H. *et al.* Quantifying and understanding the triboelectric series of inorganic non-metallic materials. *Nature communications* **11**, 1-7 (2020).
- 104 Niu, S. *et al.* Theoretical study of contact-mode triboelectric nanogenerators as an effective power source. *Energy Environmental Science* **6**, 3576-3583 (2013).
- 105 Zhou, Y. S. *et al.* In situ quantitative study of nanoscale triboelectrification and patterning. *Nano letters* **13**, 2771-2776 (2013).

- 106 Zhao, Z.-J. *et al.* 3D layer-by-layer Pd-containing nanocomposite platforms for enhancing the performance of hydrogen sensors. *ACS Sensors* **5**, 2367-2377 (2020).
- 107 Sahatiya, P., Puttapati, S. K., Srikanth, V. V. & Badhulika, S. Graphene-based wearable temperature sensor and infrared photodetector on a flexible polyimide substrate. *Flexible and Printed Electronics* **1**, 025006 (2016).
- 108 Wang, X. *et al.* A flexible triboelectric-piezoelectric hybrid nanogenerator based on P (VDF-TrFE) nanofibers and PDMS/MWCNT for wearable devices. *Scientific reports* **6**, 1-10 (2016).
- 109 Chen, X. *et al.* Highly compressible and robust polyimide/carbon nanotube composite aerogel for high-performance wearable pressure sensor. *ACS Applied Materials & Interfaces* **11**, 42594-42606 (2019).
- 110 Zhao, Z.-J. *et al.* Nanopattern-embedded micropillar structures for security identification. *ACS Applied Materials & Interfaces* **11**, 30401-30410 (2019).
- 111 Jeong, J. W. *et al.* High-resolution nanotransfer printing applicable to diverse surfaces via interface-targeted adhesion switching. *Nature communications* **5**, 1-12 (2014).
- 112 Li, S. & Li, W.-D. Refractive index sensing using disk-hole coupling plasmonic structures fabricated on fiber facet. *Optics Express* **25**, 29380-29388 (2017).
- 113 Pahlevaninezhad, H. *et al.* Nano-optic endoscope for high-resolution optical coherence tomography in vivo. *Nature photonics* **12**, 540-547 (2018).
- 114 Principe, M. *et al.* Optical fiber meta-tips. *Light: Science & Applications* **6**, e16226-e16226 (2017).
- 115 Lipomi, D. J. *et al.* Patterning the tips of optical fibers with metallic nanostructures using nanoskiving. *Nano letters* **11**, 632-636 (2011).

- 116 Zhang, C. *et al.* G-Fresnel smartphone spectrometer. *Lab on a Chip* **16**, 246-250 (2016).
- 117 Joo, W.-J. *et al.* Metasurface-driven OLED displays beyond 10,000 pixels per inch. *Science* **370**, 459-463 (2020).
- 118 Li, W.-D., Ding, F., Hu, J. & Chou, S. Y. Three-dimensional cavity nanoantenna coupled plasmonic nanodots for ultrahigh and uniform surface-enhanced Raman scattering over large area. *Optics Express* **19**, 3925-3936 (2011).
- 119 Cai, J., Zhang, C. & Li, W. D. Dual-Color Flexible Metasurfaces with Polarization-Tunable Plasmons in Gold Nanorod Arrays. *Advanced Optical Materials* **9**, 2001401 (2021).
- 120 Zheng, H. *et al.* Large-scale metasurfaces based on grayscale nanosphere lithography. *ACS Photonics* **8**, 1824-1831 (2021).
- 121 Im, H. *et al.* Label-free detection and molecular profiling of exosomes with a nanoplasmonic sensor. *Nature Biotechnology* **32**, 490-495 (2014).
- 122 Savas, T., Shah, S. N., Schattenburg, M., Carter, J. & Smith, H. I. Achromatic interferometric lithography for 100-nm-period gratings and grids. *Journal of Vacuum Science & Technology B* **13**, 2732-2735 (1995).
- 123 Hu, P.-c. *et al.* Displacement measuring grating interferometer: a review. *Frontiers of Information Technology & Electronic Engineering* **20**, 631-654 (2019).
- 124 Kang, M., Han, C. & Jeon, H. Submicrometer-scale pattern generation via maskless digital photolithography. *Optica* **7**, 1788-1795 (2020).
- 125 Dong, Z. *et al.* Printing beyond sRGB color gamut by mimicking silicon nanostructures in free-space. *Nano Letters* **17**, 7620-7628 (2017).
- 126 Wang, H. *et al.* Full color and grayscale painting with 3D printed low-index nanopillars. *Nano Letters* **21**, 4721-4729 (2021).

- 127 Khorasaninejad, M. & Capasso, F. Metalenses: Versatile multifunctional photonic components. *Science* **358**, eaam8100 (2017).
- 128 Wang, S. *et al.* A broadband achromatic metalens in the visible. *Nature Nanotechnology* **13**, 227-232 (2018).
- 129 Lin, R. J. *et al.* Achromatic metalens array for full-colour light-field imaging. *Nature Nanotechnology* **14**, 227-231 (2019).
- 130 Liu, Z., Pang, Y., Pan, C. & Huang, Z. Design of a uniform-illumination binocular waveguide display with diffraction gratings and freeform optics. *Optics Express* **25**, 30720-30731 (2017).
- 131 Gu, L. *et al.* Design of a uniform-illumination two-dimensional waveguide head-up display with thin plate compensator. *Optics Express* **27**, 12692-12709 (2019).
- 132 Zhu, X., Yan, W., Levy, U., Mortensen, N. A. & Kristensen, A. Resonant laser printing of structural colors on high-index dielectric metasurfaces. *Science Advances* **3**, e1602487 (2017).
- 133 Yang, W. *et al.* All-dielectric metasurface for high-performance structural color. *Nature Communications* **11**, 1-8 (2020).
- 134 Sun, S. *et al.* All-dielectric full-color printing with TiO₂ metasurfaces. *ACS Nano* **11**, 4445-4452 (2017).
- 135 Yu, N. *et al.* Light propagation with phase discontinuities: generalized laws of reflection and refraction. *Science* **334**, 333-337 (2011).
- 136 Yoon, G., Kim, K., Huh, D., Lee, H. & Rho, J. Single-step manufacturing of hierarchical dielectric metalens in the visible. *Nature Communications* **11**, 1-10 (2020).

- 137 McDonnell, C., Deng, J., Sideris, S., Ellenbogen, T. & Li, G. Functional THz emitters based on Pancharatnam-Berry phase nonlinear metasurfaces. *Nature Communications* **12**, 1-8 (2021).
- 138 Tang, Y. *et al.* Nano-Kirigami metasurface with giant nonlinear optical circular dichroism. *Laser & Photonics Reviews* **14**, 2000085 (2020).
- 139 Cai, J. *et al.* 3D volumetric energy deposition of focused helium ion beam lithography: visualization, modeling, and applications in nanofabrication. *Advanced Materials Interfaces* **5**, 1800203 (2018).
- 140 Xia, D., Ku, Z., Lee, S. & Brueck, S. Nanostructures and functional materials fabricated by interferometric lithography. *Advanced Materials* **23**, 147-179 (2011).
- 141 Min, S. *et al.* Gradient wettability induced by deterministically patterned nanostructures. *Microsystems & Nanoengineering* **6**, 1-9 (2020).
- 142 Gan, Z. *et al.* Patterning of high-aspect-ratio nanogratings using phase-locked two-beam fiber-optic interference lithography. *Journal of Vacuum Science & Technology B* **37**, 060601 (2019).
- 143 Levinson, H. J. *Principles of lithography*. Vol. 146 (SPIE press, 2005).
- 144 Mack, C. *Fundamental principles of optical lithography: the science of microfabrication*. (John Wiley & Sons, 2008).
- 145 O'Reilly, T. B. & Smith, H. I. Photoresist characterization using double exposures with interference lithography. *Journal of Vacuum Science & Technology B* **26**, 128-131 (2008).
- 146 Chang, E.-C. *et al.* Improving feature size uniformity from interference lithography systems with non-uniform intensity profiles. *Nanotechnology* **24**, 455301 (2013).

- 147 Hinsberg, W. *et al.* Deep-ultraviolet interferometric lithography as a tool for assessment of chemically amplified photoresist performance. *Journal of Vacuum Science & Technology B* **16**, 3689-3694 (1998).
- 148 Fallica, R., Kirchner, R., Schift, H. & Ekinci, Y. High-resolution grayscale patterning using extreme ultraviolet interference lithography. *Microelectronic Engineering* **177**, 1-5 (2017).
- 149 Haas, M. R. in *Airborne Telescope Systems II*. 85-96 (SPIE).
- 150 Barnes, S. *et al.* in *Ground-based and Airborne Instrumentation for Astronomy II*. 247-258 (SPIE).
- 151 Lu, P. P. *et al.* Precise diffraction efficiency measurements of large-area greater-than-99%-efficient dielectric gratings at the Littrow angle. *Optics Letters* **34**, 1708-1710 (2009).
- 152 Yue, G., Lei, Y., Die, J.-H., Jia, H.-Q. & Chen, H. Fabrication of 4-inch nano patterned wafer with high uniformity by laser interference lithography. *Chinese Physics Letters* **35**, 054207 (2018).
- 153 Yang, Y.-K., Wu, Y.-X., Lin, T.-H., Yu, C.-W. & Fu, C.-C. in *Laser-based Micro- and Nanoprocessing X*. 199-207 (SPIE).
- 154 Rouw, R. & Scholte, H. S. Increased structural connectivity in grapheme-color synesthesia. *Nature Neuroscience* **10**, 792-797 (2007).
- 155 Ji, C. *et al.* Engineering light at the nanoscale: structural color filters and broadband perfect absorbers. *Advanced Optical Materials* **5**, 1700368 (2017).
- 156 Zollinger, H. *Color chemistry: syntheses, properties, and applications of organic dyes and pigments*. (John Wiley & Sons, 2003).

- 157 Ge, D. *et al.* A robust smart window: reversibly switching from high transparency to angle-independent structural color display. *Advanced Materials* **27**, 2489-2495 (2015).
- 158 Walia, J., Dhindsa, N., Khorasaninejad, M. & Saini, S. S. Color generation and refractive index sensing using diffraction from 2D silicon nanowire arrays. *Small* **10**, 144-151 (2014).
- 159 Duempelmann, L., Casari, D., Luu-Dinh, A., Gallinet, B. & Novotny, L. Color rendering plasmonic aluminum substrates with angular symmetry breaking. *ACS Nano* **9**, 12383-12391 (2015).
- 160 Zhang, Y. *et al.* Ultrafast light-controlled growth of silver nanoparticles for direct plasmonic color printing. *ACS Nano* **12**, 9913-9921 (2018).
- 161 Baek, K., Kim, Y., Mohd-Noor, S. & Hyun, J. K. Mie resonant structural colors. *ACS Applied Materials & Interfaces* **12**, 5300-5318 (2020).
- 162 Lu, L. *et al.* Reversible tuning of Mie resonances in the visible spectrum. *ACS Nano* **15**, 19722-19732 (2021).
- 163 Wang, Y. *et al.* Bioinspired structural color patch with anisotropic surface adhesion. *Science Advances* **6**, eaax8258 (2020).
- 164 Cao, X. *et al.* Replicating the Cynandra opis Butterfly's Structural Color for Bioinspired Bigrating Color Filters. *Advanced Materials* **34**, 2109161 (2022).
- 165 Chen, S. *et al.* Tunable Structural Color Images by UV-Patterned Conducting Polymer Nanofilms on Metal Surfaces. *Advanced Materials* **33**, 2102451 (2021).
- 166 Zhou, L. *et al.* Dynamic structural color from wrinkled thin films. *Advanced Optical Materials* **8**, 2000234 (2020).
- 167 Ng, R. J. H., Krishnan, R. V., Wang, H. & Yang, J. K. Darkfield colors from multi-periodic arrays of gap plasmon resonators. *Nanophotonics* **9**, 533-545 (2020).

- 168 Ruan, Q. *et al.* Reconfiguring colors of single relief structures by directional stretching. *Advanced Materials* **34**, 2108128 (2022).
- 169 Chen, Y. *et al.* Dynamic color displays using stepwise cavity resonators. *Nano Letters* **17**, 5555-5560 (2017).
- 170 Daqiqeh Rezaei, S., Ho, J., Wang, T., Ramakrishna, S. & Yang, J. K. Direct color printing with an electron beam. *Nano Letters* **20**, 4422-4429 (2020).
- 171 Yan, Z. *et al.* Floating solid-state thin films with dynamic structural colour. *Nature Nanotechnology* **16**, 795-801 (2021).
- 172 Proust, J., Bedu, F., Gallas, B., Ozerov, I. & Bonod, N. All-dielectric colored metasurfaces with silicon Mie resonators. *ACS Nano* **10**, 7761-7767 (2016).
- 173 Yang, B. *et al.* Ultrahighly saturated structural colors enhanced by multipolar-modulated metasurfaces. *Nano Letters* **19**, 4221-4228 (2019).
- 174 Kong, D. *et al.* Optimization of gratings in a diffractive waveguide using relative-direction-cosine diagrams. *Optics Express* **29**, 36720-36733 (2021).

List of Publications

Journal publications

- [1]. Zhuofei Gan, Hongtao Feng, Liyang Chen, Siyi Min, Chuwei Liang, Menghong Xu, Zijie Jiang, Zhao Sun, Chuying Sun, Dehu Cui and Wen-Di Li. 2022, Spatial modulation of nanopattern dimensions by combining interference lithography and grayscale-patterned secondary exposure, *Light: Science & Applications* **11**, 89
- [2]. Zhuofei Gan, Jingxuan Cai, Chuwei Liang, Liyang Chen, Siyi Min, Xing Cheng, Dehu Cui, and Wen-Di Li. 2019, Patterning of high-aspect-ratio nanogratings using phase-locked two-beam fiber-optic interference lithography, *Journal of Vacuum Science & Technology B* **37**, 060601.
- [3]. Heekwon Lee, Zhuofei Gan, Mojun Chen, Siyi Min, Jihyuk Yang, Zhaoyi Xu, Xueying Shao, Yuan Lin, Wen-Di Li, and Ji Tae Kim. 2020, On-Demand 3D Printing of Nanowire Probes for High-Aspect-Ratio Atomic Force Microscopy Imaging, *ACS Applied Materials & Interfaces* **12**, 46571–46577.
- [4]. Liyang Chen, Wei Li, Zhuofei Gan, Yaya Zhou, Ming Chen, Dehu Cui, Haixiong Ge, Paddy KL Chan, Liqiu Wang, Wen-Di Li. 2022, Ultrathin metal-mesh Janus membranes with nanostructure-enhanced hydrophobicity for high-efficiency fog harvesting, *Journal of Cleaner Production* **363**, 132444
- [5]. Zhuofei Gan, Jingxuan Cai, Chuying Sun, Liyang Chen, Junyi Yu, Zeyu Liang, Zhao Sun, Siyi Min, Fei Han, Yu Liu, Xing Cheng, Shuhui Yu, Dehu Cui, and Wen-Di Li, High-fidelity and Clean Nanotransfer Lithography Using Structure-embedded and Electrostatic-adhesive Carrier. (Submitted)

- [6]. Liyang Chen, Zhuofei Gan, Yejin Zhang, Wanqing Cai, Guo-Dan Wei, Dehu Cui, Jingxuan Cai, and Wen-Di Li, Hybrid modeling of perovskite light-emitting diodes with nanostructured emissive layers. (Submitted)

Conference paper

- [1]. Zhuofei Gan, Dehu Cui, and Wen-Di Li, “Spatial modulation of nanopattern dimensions by combining interference lithography and grayscale-patterned secondary exposure” *the 65th International Conference on Electron, Ion and Photon Beam Technology and Nanofabrication*, May 31-June 3, 2022, New Orleans, USA.
- [2]. Liyang Chen, Zhuofei Gan, Dehu Cui, Jingxuan Cai, and Wen-Di Li, “Optical analysis of perovskite light-emitting diodes with nanostructured emissive layer via electrical simulation-assisted location of dipoles”, *the 16th IEEE International Conference on Nano/Micro Engineered & Molecular Systems*, April 25-29, 2021, Xiamen, China.
- [3]. Zhuofei Gan, Chuwei Liang, Jingxuan Cai, Dehu Cui, and Wen-Di Li, “Step-and-repeat Nanopatterning Using Compact Two-beam Fibre-optic Interference Lithography”. *the 63th International Conference on Electron, Ion and Photon Beam Technology and Nanofabrication*, May 28-31, 2019, Minneapolis, USA.
- [4]. Jingxuan Cai, Zhuofei Gan, Cuiping Zhang, and Wen-Di Li, “Metallic Nanostructures on Arbitrary Surfaces Fabricated by Solution-processed Nanopatterning and Nanotransfer Printing”. *the 63rd International Conference on Electron, Ion and Photon Beam Technology and Nanofabrication*, May 28-31, 2019, Minneapolis, USA.